

HYDROGENATION OF CARBON DIOXIDE TO FORMIC ACID BY
SINGLE-ATOM Cu CATALYST ANCHORED ON MOF-808(Zr)



A THESIS SUBMITTED IN PARTIAL FULFILLMENT OF THE REQUIREMENT FOR THE
DEGREE OF MASTER OF SCIENCE IN APPLIED CHEMISTRY
DEPARTMENT OF CHEMISTRY SCHOOL OF SCIENCE
KING MONGKUT'S INSTITUTE OF TECHNOLOGY LADKRABANG
2025

KMITL-2025-SC-M-012-004

This material is reserved for educational use only, not allowed for commercial use.

Forbidden to modify the content, and cite the document when use.



COPYRIGHT 2025

SCHOOL OF SCIENCE

KING MONGKUT'S INSTITUTE OF TECHNOLOGY LADKRABANG

This material is reserved for educational use only, not allowed for commercial use.

Forbidden to modify the content, and cite the document when use.

Thesis Title	Hydrogenation of Carbon Dioxide to Formic Acid Single-atom Cu Catalyst Anchored on MOF- 808(Zr)
Student Name	Nawarat Kusonjariyakun
Student ID	65056052
Degree	Master of Science (Applied Chemistry)
Department	Chemistry
Year	2025
Thesis Advisor	Asst. Prof. Dr. Warot Chotpatiwetchkul
Thesis Co-advisor	Dr. Sarawoot Impeng

Abstract

This study investigates the hydrogenation of carbon dioxide to formic acid on Co^{2+} - and Cu^{2+} -MOF-808 catalysts using density functional theory (DFT) and microkinetic modeling (MKM) for calculations. Two possible pathways were examined: without introducing a second H_2 molecule (pathway A), and introducing a second H_2 molecule (pathway B). Pathway B demonstrated superior performance, characterized by energy barriers that were three times lower than pathway A and a thermodynamic shift from an endergonic to an exergonic process, thereby enhancing both kinetic and thermodynamic favorability. Formate intermediates were observed in bidentate-chelating and quasi-bidentate geometries. Cu^{2+} -MOF-808 exhibited higher catalytic activity than Co^{2+} -MOF-808, primarily due to Cu's ability to stabilize the transition state via the Jahn-Teller effect, favoring a square planar geometry, which is less pronounced in Co. Microkinetic modeling confirmed these findings, revealing a higher turnover frequency (TOF) for Cu at lower temperatures, primarily governed by H_2 concentration. Formic acid desorption was identified as the rate-determining step, exerting a significant influence on reaction efficiency and catalyst performance.

Keywords: CO_2 hydrogenation, MOFs, Single-atom catalysts and DFT calculations

Acknowledgement

Firstly, I would like to thank to Asst. Prof. Dr. Warot Chotpatiwetchkul, my thesis advisor, throughout my M.Sc. at King Mongkut's Institute of Technology Ladkrabang. This includes his kind supervision, his knowledge and way of thinking, helpful suggestion and constructive comments. I have appealed fruitful discussion and inspiration throughout the course of this work. His kindness will always remember and never be forgotten.

I am also deeply thankful to Dr. Sarawoot Impeng, my co-advisor, and Miss Jirapat Santatiwongchai for their shared expertise, thoughtful advice, and assistance in proofreading my thesis.

My appreciation extends to Assoc. Prof. Dr. Sutinee Girdthep and Assoc. Prof. Dr. Rathawat Daengngern for their valuable knowledge and suggestions during my thesis examination and for their efforts in proofreading my work.

I would also like to thank members of the Applied Computational Chemistry Research Unit (ACCRU). The time spent with all of you was filled with joy and meaningful collaboration. Thank you for sharing your knowledge, ideas, and friendship.

I am sincerely grateful to the School of Science, King Mongkut's Institute of Technology Ladkrabang (Grant No. RA/TA-2565-M-009), the Nanoscale Simulation Laboratory at the National Nanotechnology Center (NANOTEC), and the NSTDA Supercomputer Center (ThaiSC) for providing financial support and computational resources.

Finally, I would like to thank my family, my friends and seventeen who always care, love and support throughout my life.

Miss Nawarat Kusonjariyakun

Table of contents

	Page
Abstract	ii
Acknowledgement	iii
Table of contents	iv
List of tables	vi
List of schemes	vii
List of figures	viii
Abbreviations/Symbols	xi
Chapter 1 Introduction	1
1.1 Research motivation	1
1.2 Objectives of the study	5
1.3 Scope of the study	5
1.4 Benefits of the study	5
Chapter 2 Theory and literature reviews	6
2.1 CO ₂ conversion and Utilization	6
2.2 Metal-organic Frameworks (MOFs)	7
2.2.1 MOF-808	8
2.3 Computational Chemistry	8
2.4 Density Functional Theory (DFT)	11
2.5 Microkinetic modelling	13
2.6 Literature reviews	14

This material is reserved for educational use only, not allowed for commercial use.

Forbidden to modify the content, and cite the document when use.

Chapter 3 Research methodology	21
3.1 Model	21
3.2 Method	22
3.3 Proposed mechanism for hydrogenation of CO ₂ to formic acid	23
Chapter 4 Main results and discussion	24
4.1 Structure, electronic properties and stability of Co ²⁺ - and Cu ²⁺ -MOF-808	24
4.2 Reaction mechanisms of CO ₂ hydrogenation to formic acid	25
4.2.1 Pathway A: without introducing a second H ₂ molecule	27
4.2.2 Pathway B: with introducing a second H ₂ molecule	31
4.2.3. Microkinetic modeling	38
Chapter 5 Conclusions and suggestions	43
5.1 Conclusions	43
5.2 Suggestions	44
References	45
Appendix	53
Appendix A: Supporting information	54
Appendix B: Publication	74
Author biography	88

List of tables

Table	Page
3.1 The relative energies of Co^{2+} - and Cu^{2+} -MOF-808 in all possible spin states were computed using the uM06-L/def2-SVP level of theory	22
4.1 Gibbs free energy of INT3, TS2 and INT4 for HCOO and COOH over Co^{2+} - and Cu^{2+} -MOF-808	25
4.2 The vibrational modes of the formate intermediate in both chelating and quasi-bidentate geometries on Co- and Cu-MOF-808 catalysts	34



List of schemes

Scheme	Page
3.1 Two possible pathways for hydrogenation of CO ₂ to formic acid using H ₂ over Co- and Cu-MOF-808 catalysts	23



List of figures

Figure	Page
1.1 Zr-MOF with 1,4-benzene-dicarboxylate (BDC) as linker, UiO-66, Zirconium, oxygen, carbon, and hydrogen atoms are red, blue, gray, and white, respectively	3
1.2 Relevant structural features and representations of NU-1000.	4
1.3 Topology of MOF-808; Atom color scheme: C, black; O, red; Zr, blue polyhedral H atoms are omitted for clarity. Yellow and orange balls indicate the space in the framework.	4
2.1 The industrial carbon cycle.	6
2.2 Composition of MOFs in catalysis.	7
2.3 Structures of (a) MOF-808, (b) BTC3- linker, (c) Zr metal node and (d) MOF-808 cluster.	8
2.4 The increase in computational time in relation to the number of stochastic particles. Computers with more cores can perform calculations more quickly but the effect becomes consistent after a certain number of cores is reached.	10
2.5 Cartoon representation of the two different methods of viewing a system electronically. For Ab initio, the method views electrons in Many-Body perspective which give rise to the necessity to identify the electron-electron repulsion force. DFT views an electronic system as density and put more importance in capturing the self-interactions of electrons.	12
2.6 Potential energy surface (PES) of CO ₂ hydrogenation on Ni (111).	14
2.7 Energy profile for the CO ₂ hydrogenation for both systems: Cu-MOF-5 (solid line for stepwise and dashed line for concerted) and gas-phase uncatalyzed reaction (dotted line).	15
2.8 The optimized structure and atomic NBO charges of the Cu/dG material. (All distances are in Å)	16
2.9 The reaction mechanism of hydrogenation of CO ₂ to formic acid, including 3 routes: a) co-adsorption of CO ₂ and H ₂ , b) H ₂ dissociation, and c) H ₂ dissociation with H spillover, respectively.	17
2.10 The hydrogenation reaction of carbon dioxide to convert to formate and formic acid over bimetallic palladium copper hydride clusters.	18

This material is reserved for educational use only, not allowed for commercial use.

Forbidden to modify the content, and cite the document when use.

2.11 MOF-808-Encapsulated Single-Atom Metal Catalysts of Carbon monoxide oxidation.	19
2.12 MOF-808-Encapsulated Single-Atom Metal Catalysts of CO ₂ hydrogenation.	20
3.1 (a) Structure of MOF-808 and (b) Cluster models before metalation	
(c) Cluster models after metalation with Co and Cu single atoms.	21
4.1 (a) Optimized structures of Co ²⁺ -MOF-808 and (b) Optimized structures of Cu ²⁺ -MOF-808. (Bond lengths are in Å.)	24
4.2 Optimized structures of TS and INT for HCOO and COOH over Co ²⁺ - and Cu ²⁺ -MOF-808.	26
4.3 Gibbs free energy profile of CO ₂ hydrogenation to formic acid via the chelating formate intermediate in pathway A over Co ²⁺ and Cu ²⁺ -MOF-808.	27
4.4 The optimized structures of INT1, TS1 and INT2 of H ₂ adsorption and H ₂ dissociation step.	27
4.5 Optimized structures of INT3, TS2 and INT4 of the formation of formate intermediate.	29
4.6 Optimized structures of TS3-A and PROD-A for the formic acid formation.	30
4.7 Gibbs free energy profile over Co ²⁺ -MOF-808 of pathway B investigates two routes-bidentate chelating and quasi-bidentate by introducing a second H ₂ molecule.	31
4.8 Optimized structures of the INT4, INT4', TS3-B, TS3-B' INT5, INT5' and PROD for CO ₂ hydrogenation to formic acid using H ₂ over Co ²⁺ -MOF-808.	32
4.9 Gibbs free energy profile over Cu ²⁺ -MOF-808 of pathway B investigates two routes-bidentate chelating and quasi-bidentate by introducing a second H ₂ molecule.	32
4.10 Optimized structures of the INT4, INT4', TS3-B, TS3-B' INT5, INT5' and PROD for CO ₂ hydrogenation to formic acid using H ₂ over Cu ²⁺ -MOF-808.	33
4.11 The structure of TS3-B shows Co in a slightly distorted square planar geometry, while Cu adopts an almost perfect square planar arrangement.	34
4.12 (a) Optimized structures of Co(O ₂ CH) ₂ and Cu(O ₂ CH) ₂ with imposed symmetry constraints, highlighting their energetic stabilities relative to the most stable	

This material is reserved for educational use only, not allowed for commercial use.

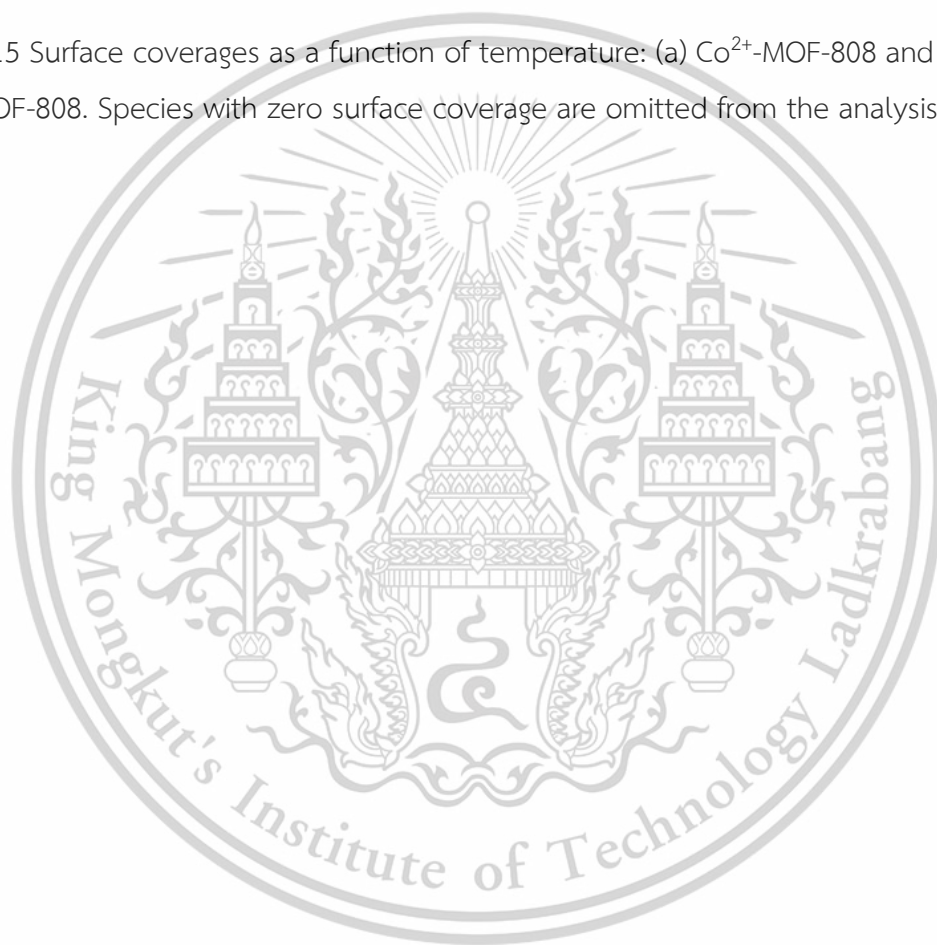
Forbidden to modify the content, and cite the document when use.

configurations in D_{2h} and D_{2d} symmetries. (b) A schematic representation of d-orbital splitting in d^7 and d^9 ML_4 complexes. 36

4.13 Turnover frequency (TOF) for HCOOH production is analyzed as a function of temperature: (a) overall reaction mechanisms, (b) TOF over Co^{2+} -MOF-808 and (c) over Cu^{2+} -MOF-808. Pathway B and B'. 49

4.14 Degree of rate control (DRC) as a function of temperature: (a) Co^{2+} -MOF-808 and (b) Cu^{2+} -MOF-808. Elementary reaction steps with a DRC coefficient of zero are excluded from the analysis. 41

4.15 Surface coverages as a function of temperature: (a) Co^{2+} -MOF-808 and (b) Cu^{2+} -MOF-808. Species with zero surface coverage are omitted from the analysis. 41



Abbreviations/Symbols

Abbreviations/Symbols	Meaning
DFT	Density Functional Theory
H ₂	Hydrogen
CO ₂	Carbon dioxide
MOFs	Metal-organic Frameworks
Co ²⁺	Cobalt ion
Cu ²⁺	Copper ion
HCOOH	Formic acid
CCUS	Carbon capture, utilization and storage
ΔG	Gibbs free energy
SACs	Single-atom catalysts
UiO-66	University of Oslo-66
NU-1000	Northwestern University-1000
MOF-808	Metal-organic Framework-808
Zn ²⁺	Zinc ion
Fe ²⁺	Iron ion
Pt ²⁺	Platinum ion
Ni ²⁺	Nickel ion
Pd ²⁺	Palladium ion
PBE	Perdew-Burke-Ernzerhof
M06-L	Minnesota 06 functional
def2-SVP	Split valence polarization
def2-TZVP	Valence triple-zeta polarization
SDD	Stuttgart-Dresden
NBO	Natural Bond Orbital
ψ _i	Wave function of single particle
Ĥ	Hamiltonian
E _i	Eigenvalue
Ψ	wavefunctions

This material is reserved for educational use only, not allowed for commercial use.

Forbidden to modify the content, and cite the document when use.

Abbreviations/Symbols

TOF	Turnover Frequency
MKM	Mean-field microkinetic modeling
DRC	Degree of Rate Control
k	Rate constant
R	Gas constant
T	Temperature
k_{ads}	Rate constant of adsorption reaction
k_{des}	Rate constant of desorption reaction
S	sticking coefficient
P	Partial pressure
A	Area of surface site
m	Mass of adsorbate
k_b	Boltzmann constant
h	Planck's constant
σ	Symmetry number of a molecule
θ_{rot}	Rotational temperature of a molecule
E_{des}	Desorption energy
ρ	Density
INT	Intermediate
TS	Transition state
PROD	Product
HCOO	Formate
COOH	Carboxyl
ΔE	Relative energy
E_a	Activation energy

This material is reserved for educational use only, not allowed for commercial use.

Forbidden to modify the content, and cite the document when use.

Chapter 1

Introduction

1.1 Research motivation

Carbon dioxide (CO₂), predominantly emitted through the extensive reliance on fossil fuels, serves as a principal contributor to global warming and climate change. Its emissions elevate greenhouse gas concentrations, effectively trapping heat within the atmosphere and causing profound environmental and economic repercussions. Addressing this challenge is imperative for fostering environmental sustainability. Carbon capture, utilization, and storage (CCUS) technologies have been widely acknowledged as essential measures for mitigating atmospheric CO₂ and combating climate change [1,2]. As a result, substantial research efforts have focused on the development of advanced adsorptive and catalytic materials capable of capturing CO₂ and converting it into valuable chemical products, thereby transforming a significant pollutant into a resource with extensive industrial applications.

The hydrogenation of carbon dioxide (CO₂) to formic acid has emerged as a promising strategy for CO₂ valorization, offering the dual benefits of mitigating CO₂ emissions while producing a valuable chemical product [3–7]. Formic acid holds significant potential as a hydrogen storage medium and as a fuel for formic acid fuel cells, presenting a liquid alternative for renewable energy storage and fuel cell technologies. Despite its advantages, the catalytic hydrogenation of CO₂ using H₂ poses considerable challenges due to the inherent stability of CO₂ ($\Delta G^{\circ}_{298} = -394.4$ kJ/mol) and the thermodynamic constraints of the reaction ($\Delta G^{\circ}_{298} = +32.9$ kJ/mol) [8]. Overcoming these challenges necessitates the development of catalysts with exceptional activity and selectivity, capable of facilitating the reaction efficiently under mild conditions. This research area is pivotal for advancing catalysis and achieving sustainable chemical transformations.

Metal-organic frameworks (MOFs) are crystalline porous materials constructed from metal ions or clusters coordinated with organic linkers [9,10]. The versatility in selecting and modifying metal ions/clusters and organic linkers enables the synthesis of a wide array of MOFs with distinctive properties, including high surface areas, tunable pore sizes, and remarkable thermal and chemical stability. These attributes make MOFs

This material is reserved for educational use only, not allowed for commercial use.

Forbidden to modify the content, and cite the document when use.

highly adaptable for various applications, such as gas storage, separation, and catalysis, by promoting efficient interactions with reactant molecules [11,12].

Zr-based metal-organic frameworks (MOFs), including UiO-66 [13], NU-1000 [14], and MOF-808 [15] have garnered significant attention for their catalytic potential due to unique structural attributes, such as missing ligands that generate structural defects. These defects serve as active catalytic sites and stable platforms for single-atom catalysts (SACs) [16–22], preventing SAC aggregation and enhancing catalytic efficiency. For instance, a recent study by Zhang et al. [23], demonstrated that MOF-808, modified with single Zn^{2+} ions integrated into Zr-oxide nodes, achieved high selectivity for CO_2 hydrogenation to methanol. Similarly, Liu et al. [24], conducted a theoretical investigation into the hydrogenation pathways of CO_2 to C1 products (CO , HCOOH , CH_3OH , CH_4) on MOF-808 loaded with various metal ions, including Cu^{2+} , Fe^{2+} , Pt^{2+} , Ni^{2+} , and Pd^{2+} . Their findings identified Cu^{2+} -MOF-808 as the most active catalyst. While these studies have provided foundational insights, further exploration of the reaction mechanisms is crucial to advancing the design and development of more efficient catalytic systems.

In this study, we employed density functional theory (DFT) calculations and microkinetic modeling to investigate the hydrogenation of CO_2 to formic acid on Co^{2+} - and Cu^{2+} -MOF-808 catalysts. While Cu^{2+} is renowned for its catalytic efficiency, Co^{2+} was analyzed as a potential alternative. A key outcome of this research is the identification of formate intermediates in both quasi-bidentate and chelating geometries, with the quasi-bidentate configuration representing a novel finding. For Co^{2+} , these geometries exhibit comparable energetic stabilities, whereas Cu^{2+} displays a slight energy disparity between the two. These distinct configurations facilitate two alternative pathways for incorporating the second H_2 molecule, a critical step in the conversion of the formate intermediate into formic acid.

Our analysis underscores the significance of electronic structures and spin states for Co^{2+} and Cu^{2+} , with particular emphasis on the Jahn-Teller effect in Cu^{2+} , which plays a pivotal role in stabilizing reaction intermediates and enhancing catalytic performance. Furthermore, this work provides a comprehensive comparison of the quasi-bidentate and bidentate chelating pathways. These findings deliver critical insights into the reaction mechanism and offer a comparative evaluation of Co^{2+} - and Cu^{2+} -MOF-808 catalysts. By elucidating the distinct catalytic pathways and the

This material is reserved for educational use only, not allowed for commercial use.

Forbidden to modify the content, and cite the document when use.

influence of electronic and structural factors, this study advances the understanding of CO₂ hydrogenation processes. It also highlights new avenues for designing alternative catalytic systems, contributing significantly to the broader disciplines of surface science and catalysis.

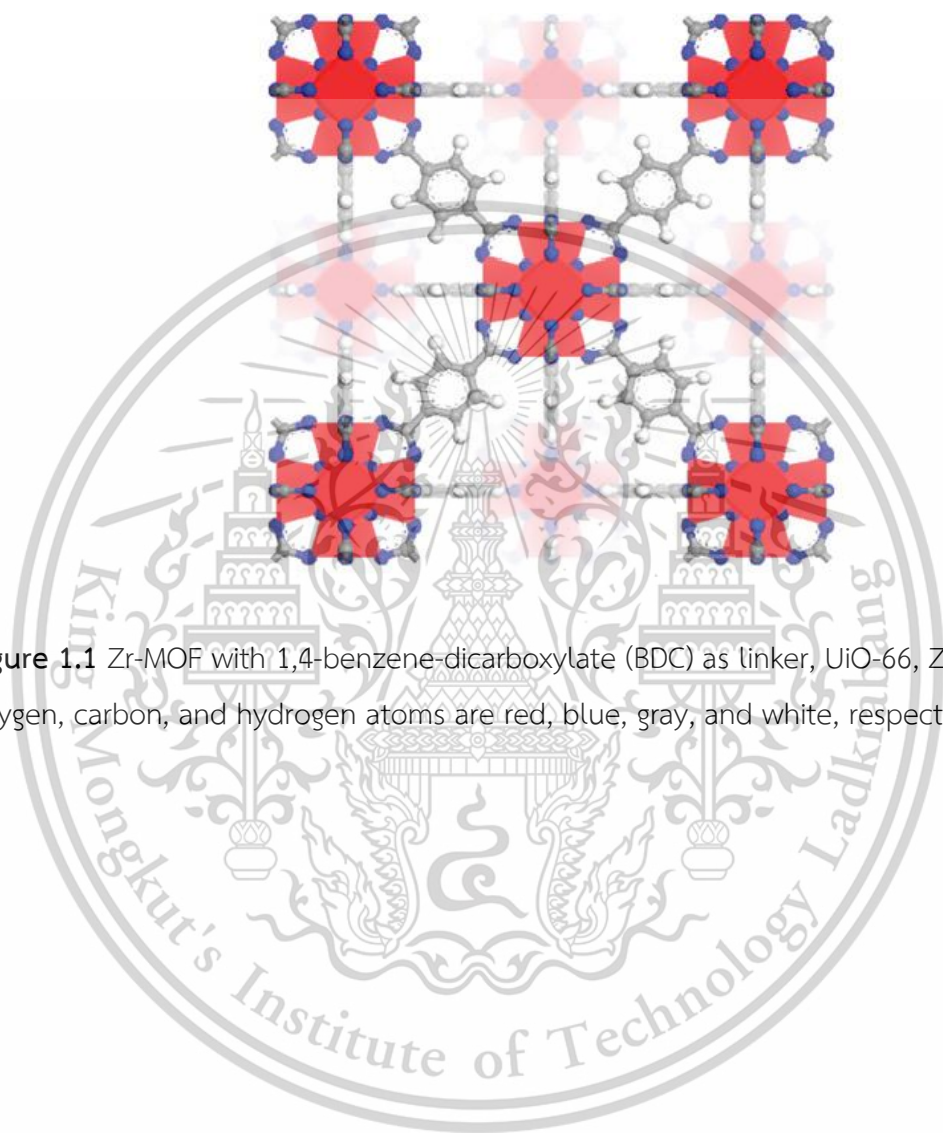


Figure 1.1 Zr-MOF with 1,4-benzene-dicarboxylate (BDC) as linker, UiO-66, Zirconium, oxygen, carbon, and hydrogen atoms are red, blue, gray, and white, respectively [13].

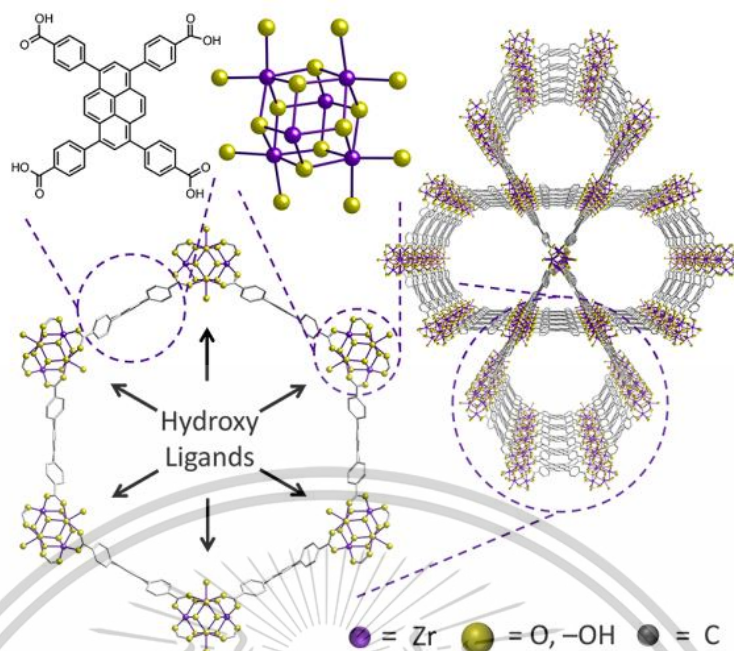


Figure 1.2 Relevant structural features and representations of NU-1000 [14].

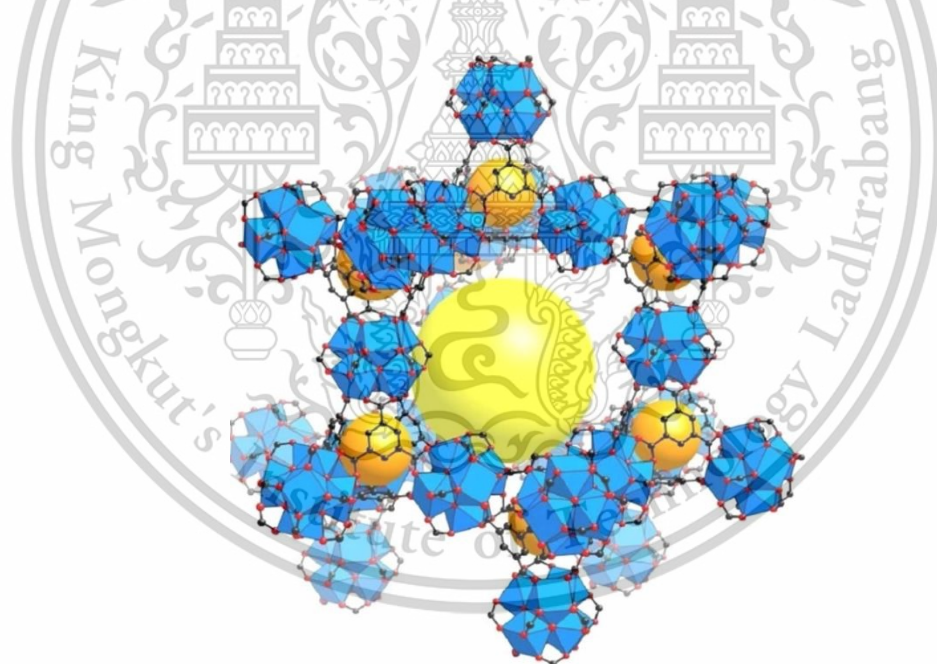


Figure 1.3 Topology of MOF-808; Atom color scheme: C, black; O, red; Zr, blue polyhedral H atoms are omitted for clarity. Yellow and orange balls indicate the space in the framework [15].

This material is reserved for educational use only, not allowed for commercial use.

Forbidden to modify the content, and cite the document when use.

1.2 Objectives of the study

1) Computational investigations of the CO₂ hydrogenation reaction mechanism were conducted using density functional theory (DFT) and microkinetic modeling (MKM) to elucidate the mechanistic pathways involved in the conversion of CO₂ to formic acid on Co²⁺- and Cu²⁺-MOF-808 catalysts.

2) The quasi-bidentate and bidentate chelating configurations of formate intermediate have been identified and characterized, representing novel structural insights that have not been previously reported.

3) The roles of the electronic structures and spin states of Co²⁺ and Cu²⁺ were analyzed, especially the Jahn-Teller effect in Cu²⁺, plays a crucial role in modulating on the catalytic activity and stability of the reaction intermediates.

1.3 Scope of the study

1) A comprehensive study of the CO₂ hydrogenation reaction mechanism to formic acid over MOF-808-supported single-atom catalysts (Co²⁺ and Cu²⁺) using density functional theory (DFT) calculations.

1.4 Benefits of the study

1) This study provides insights into the most favorable reaction pathway for converting CO₂ to formic acid, allowing for the identification of the most efficient and effective mechanism.

2) The study aims to identify and characterize a new type of catalyst that can significantly catalyze the conversion of CO₂ to formic acid, the findings could support the development of more advanced catalysts, potentially contributing to more sustainable CO₂ utilization technologies.

Chapter 2

Theory and literature reviews

2.1 CO₂ conversion and Utilization

CO₂ conversion refers to the chemical transformation of CO₂ into different forms that contain carbon from CO₂ or utilize the active oxygen atom present in CO₂. CO₂ utilization encompasses both physical processes, such as extraction, and chemical processes, such as chemical synthesis. The goals of research and development efforts in CO₂ conversion and utilization can vary depending on the applications. These goals include employing CO₂ for environmentally friendly physical or chemical processes based on its unique properties, producing useful chemicals and materials by using CO₂ as a reactant or feedstock, and replacing hazardous or less effective substances in existing processes with CO₂ as an alternative medium, solvent, or co-reactant. Additionally, CO₂ can be utilized for energy recovery or biomass growth while reducing emissions to the atmosphere through sequestration, recycling CO₂ as a carbon source for chemicals and fuels, and converting CO₂ under geologic formation conditions into new fossil energy sources [25].

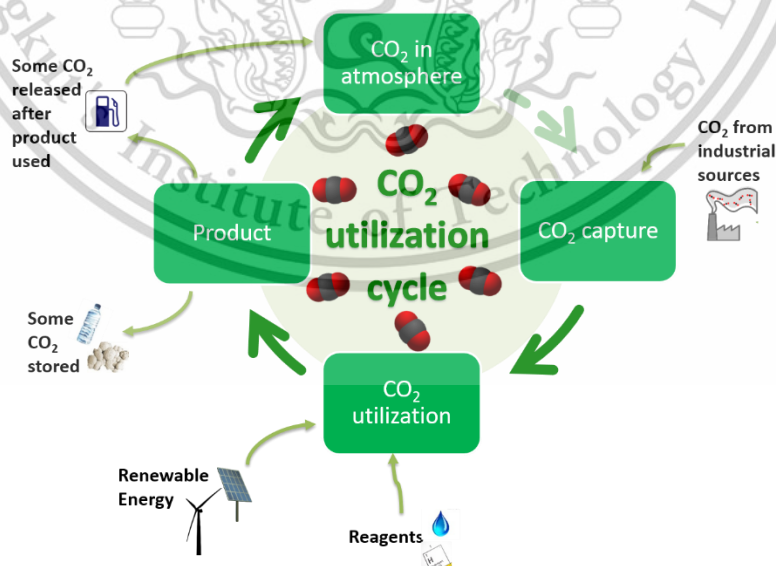


Figure 2.1 The industrial carbon cycle [26].

This material is reserved for educational use only, not allowed for commercial use.

Forbidden to modify the content, and cite the document when use.

2.2 Metal-organic Frameworks (MOFs)

Metal-Organic Frameworks (MOFs) are characterized by their network-like architectures, comprising porous structures formed through the coordination of metal nodes with organic linkers, typically carboxylates. It is considered a hybrid material with very interesting properties having a high surface area, high porosity, low density and can withstand high temperatures. It has been reported that metal-organic framework materials have been used to study gas adsorption behavior [27]. Many metal-organic framework materials are highly porous and have specialized properties (functional materials). Some can also modify the framework structure after synthesis. (post-synthesis modification) to have more chemical specificity. Meanwhile, the pore size of metal-organic framework materials can be designed before synthesis. To get the pore size at the nanometer level as desired this nanometer sized pore will help increase the gas absorption ability. These properties make MOFs of great interest for industrial research. Currently, MOFs are being applied on an industrial scale. It is used as a selector for the desired molecule and separated from other molecules in the gas separation process. It is applied to chemical catalysts that are specific to the shape and structure of the chemical. MOFs can also be used to store specific molecular substances, such as capturing and releasing hydrogen gas, etc. Therefore, metal-organic network materials, or MOFs, are considered materials that are receiving a lot of interest in industrial applications [28].

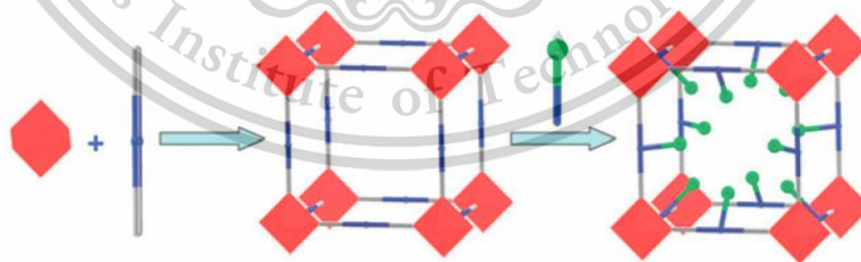


Figure 2.2 Composition of MOFs in catalysis [28].

2.2.1 MOF-808

In Figure 2.3, the components of MOF-808 are shown. MOF-808 consists of Zr metal clusters ($\text{Zr}_6\text{O}_4(\text{OH})_{10}(\text{H}_2\text{O})_6$) (Figure 2.3(b)) connected into a three-dimensional structure through benzene tricarboxylate (BTC^{3-}) (Figure 2.3(c)) with a cavity size of approximately 14 Å, having a pore volume of approximately 0.84 cm³/g and a surface area of 1600 m²/g. It is stable in air, as well as in aqueous and acidic conditions (pH 1-12), and can withstand temperatures over 400 °C. The metal ions or organic linkers can be customized as desired, and it has excellent capabilities for gas storage, capture, and separation [23]. Therefore, in this work, MOF-808 was chosen as a support for single-metal atom catalysts, specifically Co^{2+} and Cu^{2+} , for the hydrogenation of carbon dioxide to formic acid.

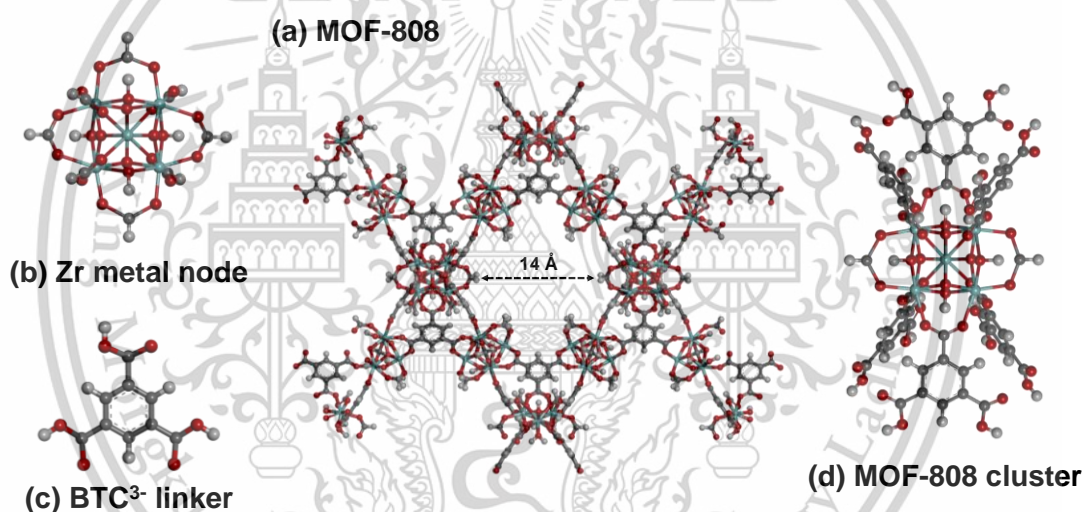


Figure 2.3 Structures of (a) MOF-808, (b) BTC^{3-} linker, (c) Zr metal node and (d) MOF-808 cluster.

2.3 Computational Chemistry

Computational chemistry is a subfield of theoretical chemistry where computer simulations assist in solving complex chemical problems [29]. Computational chemistry combines mathematical methods and fundamental laws of physics to study chemical processes [30]. In the field, a molecule or system of interest is treated as a collection of charged particles. Each molecule is different because of the unique numbers of nuclei and electrons they have. The different combinations will result in chemically

This material is reserved for educational use only, not allowed for commercial use.

Forbidden to modify the content, and cite the document when use.

different molecules as the interaction forces between the particles within the molecules are different. The said interaction forces between the particles, namely the Coulomb interaction [31], is the only important force in computational study of molecules. The interaction force dictates the most stable geometrical arrangement of a molecule, the properties, the rate which a reaction can occur, or in other words, all the characteristic of a molecule. The total interactions between particles are recorded as 'energy' in the unit kcal/mol, which indicates the stability of the molecule. The lower the energy, the more stable the structure.

The larger the size of the molecule or system, the more complex it is to compute the interaction forces. Only a system with one or two particles can be solved exactly as there is fewer interaction forces to consider. Larger systems such as enzymes or other proteins can only be solved to a certain degree of accuracy as estimation of the interaction force is necessary, though the solution can be very close to the exact value. The greater the level of detail of the estimation, the more accurate the result, but also the greater the time consumption and the more need for powerful computational devices [32].

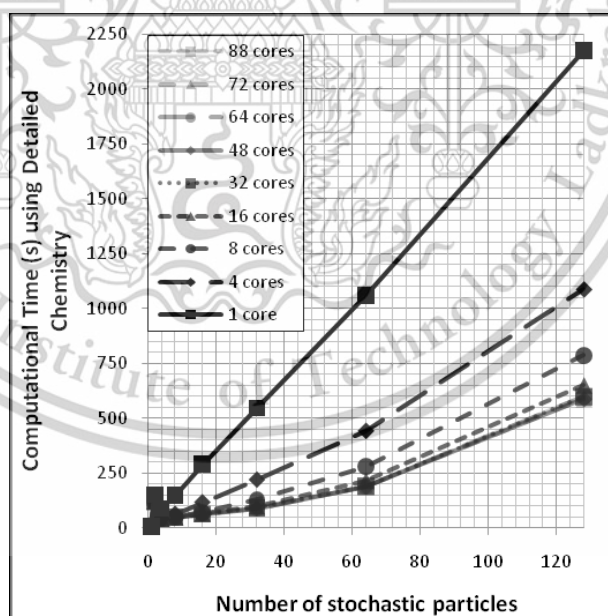


Figure 2.4 The increase in computational time in relation to the number of stochastic particles. Computers with more cores can perform calculations more

quickly but the effect becomes consistent after a certain number of cores is reached [33].

To demonstrate the quickly increasing computational power needed to calculate a large system, a simple equation related to Quantum mechanics simulation is shown below. In QM, to estimate the interaction and therefore the energy of the system, first the wavefunction of the system must be defined in terms of a wave equation. An example of wavefunction is shown in equation 1.

$$\psi = A \sin(2\pi x) \quad (\text{Equation 1})$$

To analyze the wave equation in terms of wavefunction, the Schrodinger equation is used (Equation 2.). From this equation, the nature of the wave can be described in wavefunction terms, where the total energy being summation of the kinetic energy and the potential energy function. The potential energy of a wavefunction includes the electron-electron repulsion, nuclear- electron attraction and nuclear- nuclear repulsion forces.

$$\hat{H}\psi = E\psi \quad (\text{Equation 2})$$

The Equation 3 shows a Born-Oppenheimer approximation of a system wavefunction. The equation states that the wavefunction of the system is the product of the wavefunction of nuclear and electronic wavefunction.

$$\Psi_{\text{Total}} = \Psi_{\text{electronic}} \Psi_{\text{nuclear}} \quad (\text{Equation 3})$$

From this, a system wavefunction can be defined as the product of all one-electron wavefunctions (ψ) inside an atom as shown in Equation 4. Ψ_0 is the function representing the coordinates of all the electrons in the atom, where $\Psi_0(1)$, $\Psi_0(2)$, ... , $\Psi_0(n)$ represent function of electron 1, 2, ... , n, respectively. After solving Schrödinger equation for each electron, the electron repulsion term is substituted by an average from electrostatic field calculated from $\Psi_0(2)$, $\Psi_0(3)$, ..., $\Psi_0(n)$. As the number of electrons increases, the electron repulsion term also increases, causing the rapid increase in number of mathematical equations which need to be solved.

This material is reserved for educational use only, not allowed for commercial use.

Forbidden to modify the content, and cite the document when use.

$$\psi_0 = \Psi_0(1)\Psi_0(2)\Psi_0(3) \dots \Psi_0(n) \quad (\text{Equation 4})$$

The energy of the system wavefunction ψ_0 is then calculated using the formula shown in Equation 5.

$$E = \int \psi' \hat{H} \psi d\tau \quad (\text{Equation 5})$$

After ψ_0 is computed, electron 1 from $\Psi_0(1)$ will be designated to move, resulting in ψ_1 . This repeats with $\Psi_0(2)$, $\Psi_0(3)$, ..., $\Psi_0(n)$ until all the wavefunctions are computed. This is called one cycle of calculation. The cycle and calculation will be repeated until the change in energy between the cycles are considered negligible by the criteria set.

Presently, the search for the most time efficient and accurate method for describing the interaction is still ongoing. Currently, the three main types of simulation in the field are Molecular dynamic, Quantum mechanics, and the hybrid Quantum mechanics/Molecular mechanics simulations [34–36].

2.4 Density Functional Theory (DFT)

Density functional theory (DFT) unlike the ab initio and semi empirical which are based the wavefunction, DFT uses Hohenberg-Kohn as the ground theory which refrains from the brute-force calculation of wavefunctions. The theory states that atoms and molecules at the ground-state properties are determined by its electron density functional under the condition that the energy from electron density must be greater or equal to the true energy. In electron density functional, the ρ represents the 'density' of the functional, and it can be measured by x-ray diffraction or electron diffraction unlike wavefunction. DFT function only consists of three variables for its position (x, y, z) no matter the size of the system being analyzed making it more intuitively and mathematically comprehensible and if more details are desired the number of dimensions will be increased three times incrementally. One of the lower-level theories of DFT is the local density approximation (LDA). LDA is a functional which lays groundwork for many other functionals such as PW92.

This material is reserved for educational use only, not allowed for commercial use.

Forbidden to modify the content, and cite the document when use.

Another popular type of DFT is the generalized gradient approximation (GGA). GGA functionals have information on general order gradient, which is the change in electron density of certain parts in the system. DFT can also incorporate physical values and empirical parameters. To improve the accuracy, the idea to combine two methods together was realized and named *hybrid functionals*, and example of these functionals are the combination of Hartree-Fock theory and DFT such as B3LYP or the M06 suite of functionals [37].

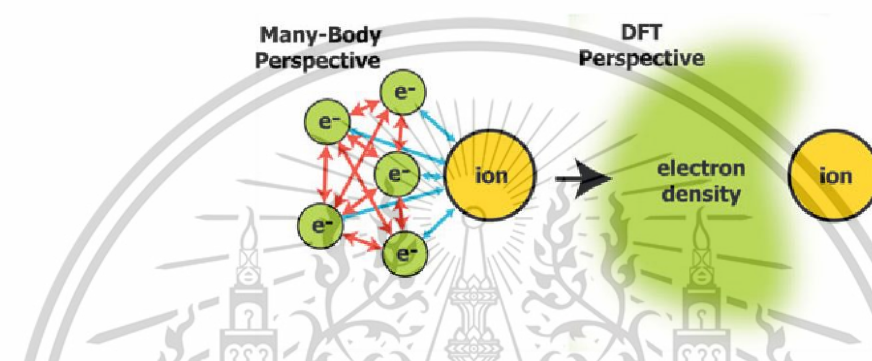


Figure 2.5 Cartoon representation of the two different methods of viewing a system electronically. For Ab initio, the method views electrons in Many-Body perspective which give rise to the necessity to identify the electron-electron repulsion force. DFT views an electronic system as density and put more importance in capturing the self-interactions of electrons [29].

Basis set is the expression of one-electron orbitals. It represents the electron configuration in the s, p, d etc. orbitals by assigning several mathematical functions to the electrons inside said orbitals to describe their energy level and position. The minimum number of functions inside a basis set must reflect all the electrons within an atom, such as for a neutral Ne atom, the minimum basis set must contain 2 s-orbital functions and 1 three component p-orbital function, equivalent to 5 functions. Minimum basis set are seldomly used since they allow for little or no electron correlation. Basis set with greater accuracy is made by doubling, tripling, and so on the number of functions, Basis set is selected according to the desired detail, the available computers, and the size of the system being studied [38].

This study examines the hydrogenation of CO_2 to formic acid using Density Functional Theory (DFT) calculations employing the M06-L functional [39]. Geometry optimizations were performed with the def2-SVP basis set [40] and the SDD

pseudopotential basis set [41]. Charge distribution analysis were conducted using the Natural Bond Orbital (NBO) method [42]. Gibbs free energy calculations were carried out at the M06-L/def2-TZVP level of theory, incorporating Grimme D3 dispersion correction [43]. All computational studies were conducted using the Gaussian 16 software package [44].

2.5 Microkinetic modelling

Mean-field microkinetic modeling (MKM) was conducted based on the DFT calculations of all elementary reaction steps. The rate constant of the surface reaction is calculated by using the Arrhenius equation (Equation 6):

$$k = \nu \cdot \exp\left(-\frac{E_a}{RT}\right) \quad (\text{Equation 6})$$

where k is the rate constant of surface reaction, E_a is the activation energy, R is the gas constant, and T is the temperature.

For the adsorption/desorption reactions, the rate constant is calculated using the Hertz-Knudsen equation [45], as shown in Equation 7 and 8:

$$k_{ads} = S \cdot \frac{PA}{\sqrt{2\pi mk_b T}} \quad (\text{Equation 7})$$

$$k_{des} = A \frac{k_b T^3}{h^3} \frac{2\pi mk_b}{\sigma \theta_{rot}} \exp\left(-\frac{E_{des}}{RT}\right) \quad (\text{Equation 8})$$

where k_{ads} and k_{des} are the rate constant for adsorption and desorption reactions, respectively. S is the sticking coefficient, P is the partial pressure of the adsorbate in gas phase, A is the area of the surface site, m is the mass of adsorbate, k_b is the Boltzmann constant, h is Planck's constant, σ is the symmetry number of a molecule, θ_{rot} is the rotational temperature of a molecule, and E_{des} is the desorption energy.

The degree of rate control (DRC) [46–49] was performed to investigate the elementary reaction steps that contribute to the rate control of the overall reaction. For the elementary reaction step i , the DRC ($X_{RC,i}$) is defined as shown in (Equation 9):

$$X_{RC,i} = \frac{k_i}{r} \left(\frac{\partial r}{\partial k_i} \right)_{k_{j \neq i}, K_i} = \left(\frac{\partial \ln r}{\partial \ln k_i} \right)_{k_{j \neq i}, K_i} \quad (\text{Equation 9})$$

where k_i , K_i , and r are the rate constants, the equilibrium constant for step i and the reaction rate, respectively. All MKM results were simulated using MKMCXX [50].

2.6 Literature reviews

Peng G. et al. [51] studied the hydrogenation of CO₂ to formic acid on the Ni(111) surface using density functional theory. Both surface-adsorbed and subsurface-adsorbed hydrogen were investigated. Two reaction mechanisms were compared: the formate intermediate and the carboxyl intermediate. The formation of formate intermediates was found to be more favorable than that of carboxyl intermediates due to a lower activation energy for the hydrogenation of the formate intermediate. Additionally, a rapid transition from unidentate to bidentate structure occurs in the formate intermediate. The hydrogenation from the carboxyl intermediate to formic acid, however, requires high energy, making it less likely to proceed. The hydrogenation of CO₂ to formic acid is an exothermic reaction, highlighting its potential for liquid fuel synthesis from carbon dioxide and for hydrogenation catalysts in general.

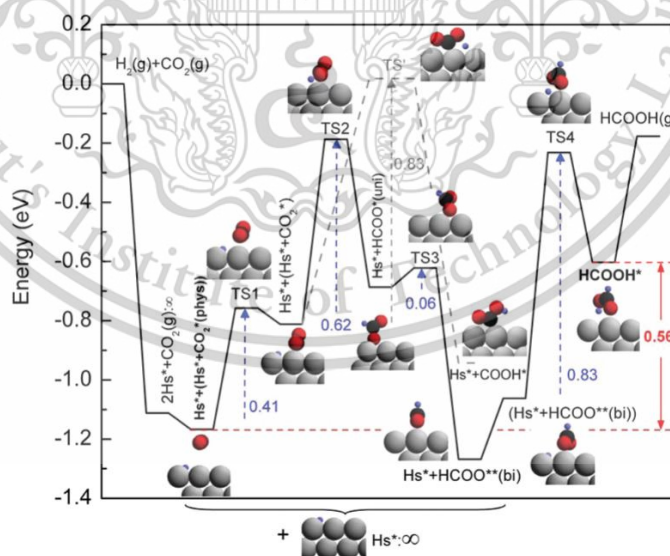


Figure 2.6 Potential energy surface (PES) of CO₂ hydrogenation on Ni (111).

Maihom T. et al. [52] investigated the production of formic acid from carbon dioxide through hydrogenation on a single Cu atom incorporated into the ligand of MOF-5, using density functional theory with the M06-L functional and basis sets 6-31G(d,p)/LANL2DZ. Two possible mechanisms of CO₂ and H₂ co-adsorption on the catalyst were studied: 1) concerted and 2) stepwise mechanisms. In the concerted mechanism, hydrogenation occurs in a single step by adding hydrogen to both the C and O atoms of CO₂ to produce formic acid. In the stepwise mechanism, the first step involves the addition of hydrogen to the C atom of CO₂ to form a formate intermediate, followed by hydrogenation at the O atom of this intermediate to yield formic acid. The activation energy for the concerted mechanism was found to be 67.2 kcal/mol, while the stepwise mechanism exhibited activation energies of 24.2 kcal/mol and 18.3 kcal/mol for the two steps, respectively. These results suggest that the stepwise mechanism is more favorable due to its lower activation energy. Additionally, the catalyst significantly reduces the activation energy of the reaction compared to the uncatalyzed reaction.

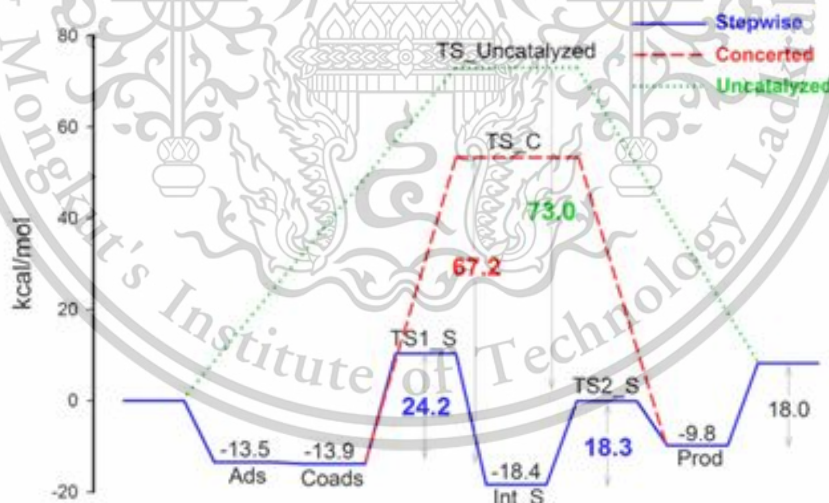


Figure 2.7 Energy profile for the CO₂ hydrogenation for both systems: Cu-MOF-5 (solid line for stepwise and dashed line for concerted) and gas-phase uncatalyzed reaction (dotted line).

Sirijaraensre J. et al. [53] conducted a computational study to investigate the properties of a Cu atom embedded on a graphene surface, denoted as Cu/dG, using density functional theory with the 6-31G(d,p)/SDD basis set. This study aimed to evaluate the catalyst's potential for converting CO₂ to formic acid. The results indicated that hydrogenation of CO₂ without prior H₂ activation requires a high activation energy, resulting in an unstable intermediate. However, H₂ dissociation into a hydride and a proton on Cu/dG facilitates easier hydrogenation. The formate structure produced via this pathway is more suitable for formic acid production than the route involving direct protonation to formate. The calculated activation energy for formic acid formation through H₂ dissociation is 11.6 kcal/mol.

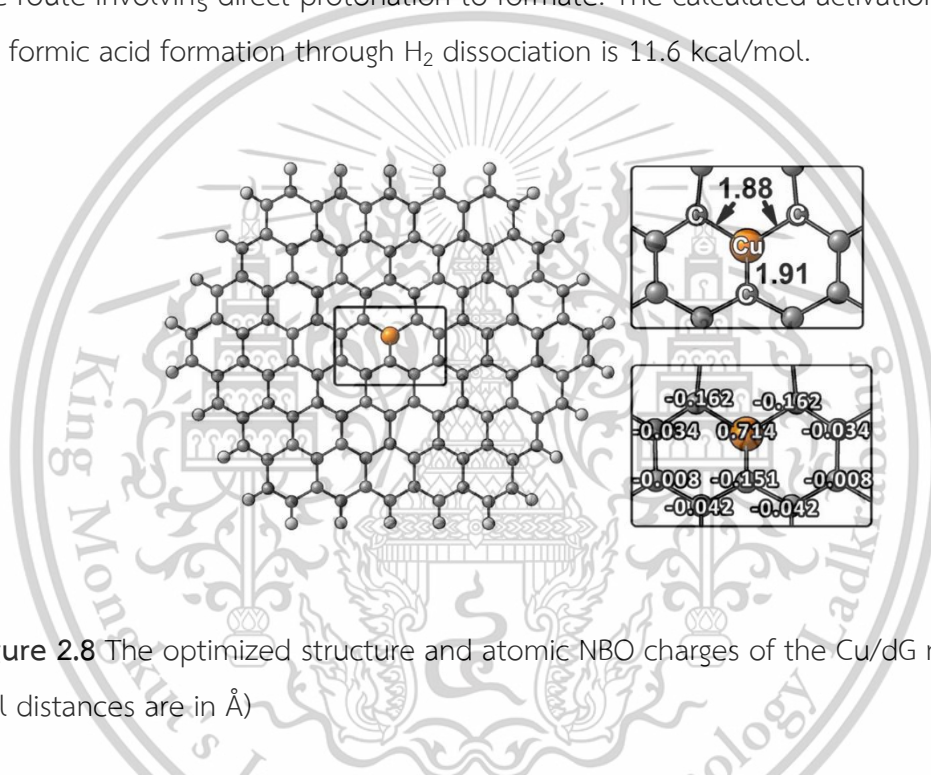


Figure 2.8 The optimized structure and atomic NBO charges of the Cu/dG material. (All distances are in Å)

Yodsin N. et al. [54] studied a catalyst for CO₂ conversion to formic acid, using a single Pt atom supported on a carbon nanocone (denoted as Pt/CNC) with DFT calculations employing the B3LYP functional and the 6-31G(d,p)/LANL2DZ basis set. The study investigated three possible routes for CO₂ hydrogenation: Route A (co-adsorption of CO₂ and H₂), Route B (H₂ dissociation), and Route BS (H₂ dissociation with H spillover) as shown in Figure 2.9. In Route A, the co-adsorption of CO₂ and H₂ follows a stepwise mechanism, proceeding through a carboxylate intermediate before forming formic acid. Calculations indicate that the first step is rate-determining, with an activation energy of 1.49 eV. Route B begins with H₂ dissociation, where an adsorbed hydrogen molecule on Pt dissociates, followed by CO₂ hydrogenation. This route can

proceed through either a carboxylate or formate intermediate. The carboxylate pathway is less favorable due to a high activation energy of 2.91 eV, while the formate pathway has a lower activation energy of 1.15 eV. Route BS involves H_2 dissociation with H spillover, similar to Route B but with an additional H spillover step following H_2 dissociation. This pathway can proceed through both formate and carboxylate intermediates. Notably, adding a second H_2 molecule after the formate intermediate was found to significantly lower the activation energy. Consequently, Route BS is the most favorable mechanism for formic acid production.

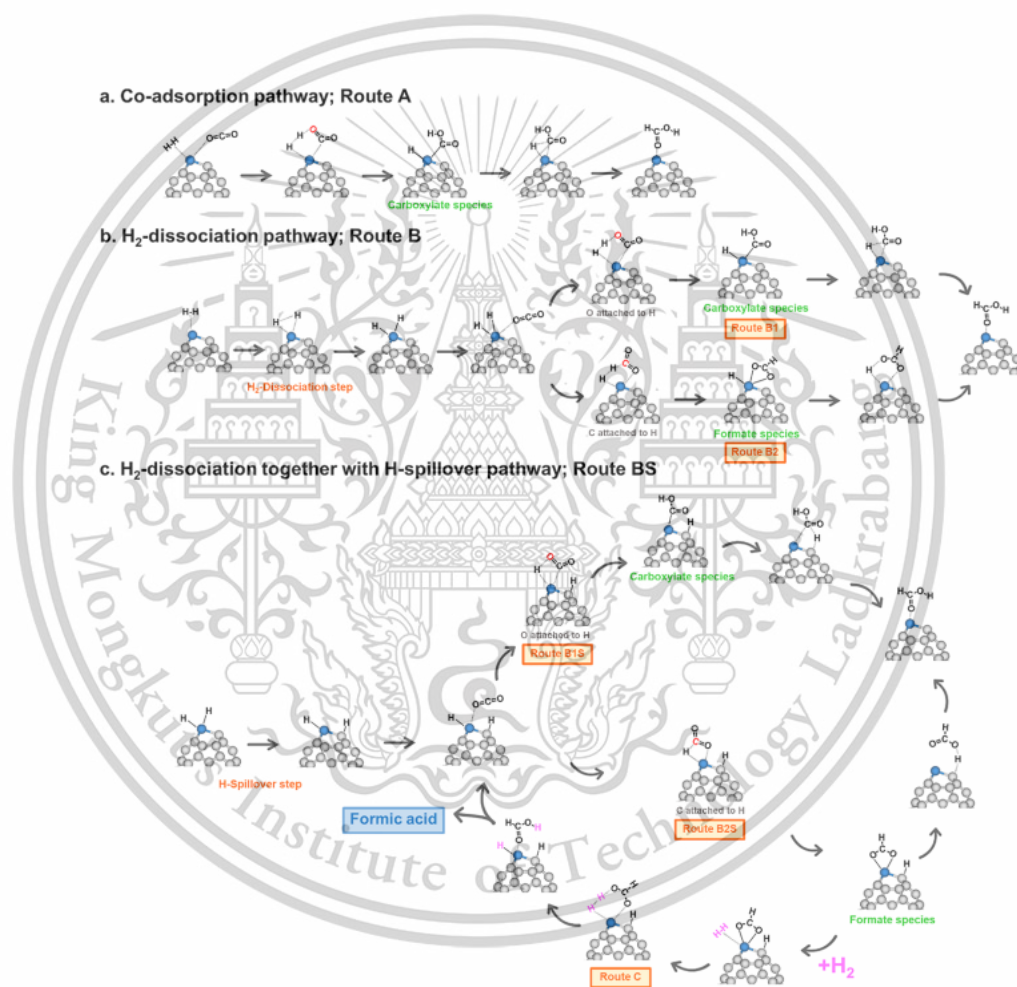


Figure 2.9 The reaction mechanism of hydrogenation of CO_2 to formic acid, including 3 routes: a) co-adsorption of CO_2 and H_2 , b) H_2 dissociation, and c) H_2 dissociation with H spillover, respectively.

Liu G. et al. [55] studied the hydrogenation of carbon dioxide to produce formate and formic acid, using bimetallic palladium-copper hydride clusters as a catalyst. Anionic mass spectrometry was employed to analyze the products of the reaction between bimetallic palladium-copper tetrahydride anions (PdCuH_4^-) and CO_2 . Density functional theory (DFT) calculations with the LANL2DZ/au₅-cc-pvtz+pp basis set demonstrated the catalyst's efficiency in forming $\text{PdCuCO}_2\text{H}_4^-$ and formate/formic acid compounds. The analysis of various structures of both PdCuH_4^- and $\text{PdCuCO}_2\text{H}_4^-$ involved photoelectron spectroscopy and quantum chemical calculations. The study observed two isomers, A and B, of PdCuH_4^- , each following distinct reaction pathways. In the first pathway, CO_2 reacts at the Cu-H bond to form a highly stable intermediate C, which requires significant energy to release formate as a product, making this pathway less favorable for formate formation. In the second pathway, CO_2 interacts with Pd and H atoms, causing rearrangement of H, Cu, and Pd atoms to produce formate, which then decomposes into PdCuH_2^- and formic acid, enabling the next catalytic cycle to proceed. This work highlights the ability of the PdCuH_4^- bimetallic cluster catalyst to convert CO_2 into formate and formic acid, as confirmed by mass spectrometry analysis.

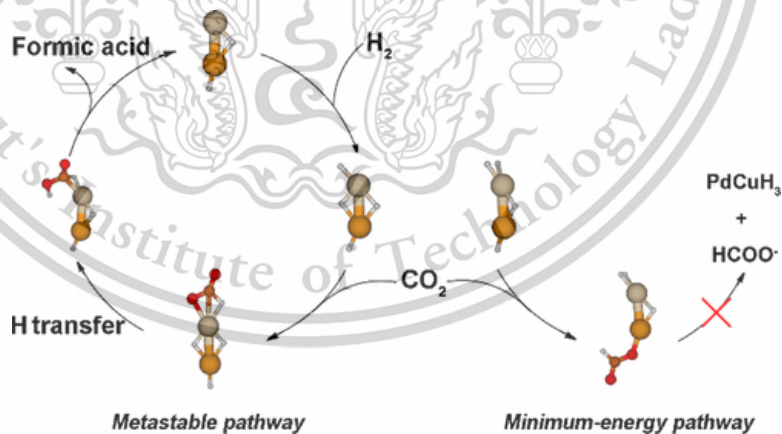


Figure 2.10 The hydrogenation reaction of carbon dioxide to convert to formate and formic acid over bimetallic palladium copper hydride clusters.

Xue W. et al. [56] investigated carbon monoxide (CO) oxidation on MOF-808 catalysts (denoted as MOF-808-M^{II}, with M = Zn, Cu, Fe, Pd, Ni, and Pt) using metal atoms in a 2+ oxidation state. The study employed density functional theory, a kinetic microstructure model, and the 6-311G**/SDD basis set. Stability analysis of various metals encapsulated in MOF-808 revealed that MOF-808-Pt^{II} was the most stable. Calculations for four oxidation pathways of CO showed that the Langmuir-Hinshelwood (LH) mechanism was the most effective. Using ESM to compute relative TOF values, MOF-808-Pt^{II} achieved the highest relative TOF value of 1.00, identifying it as the most effective catalyst for CO oxidation.

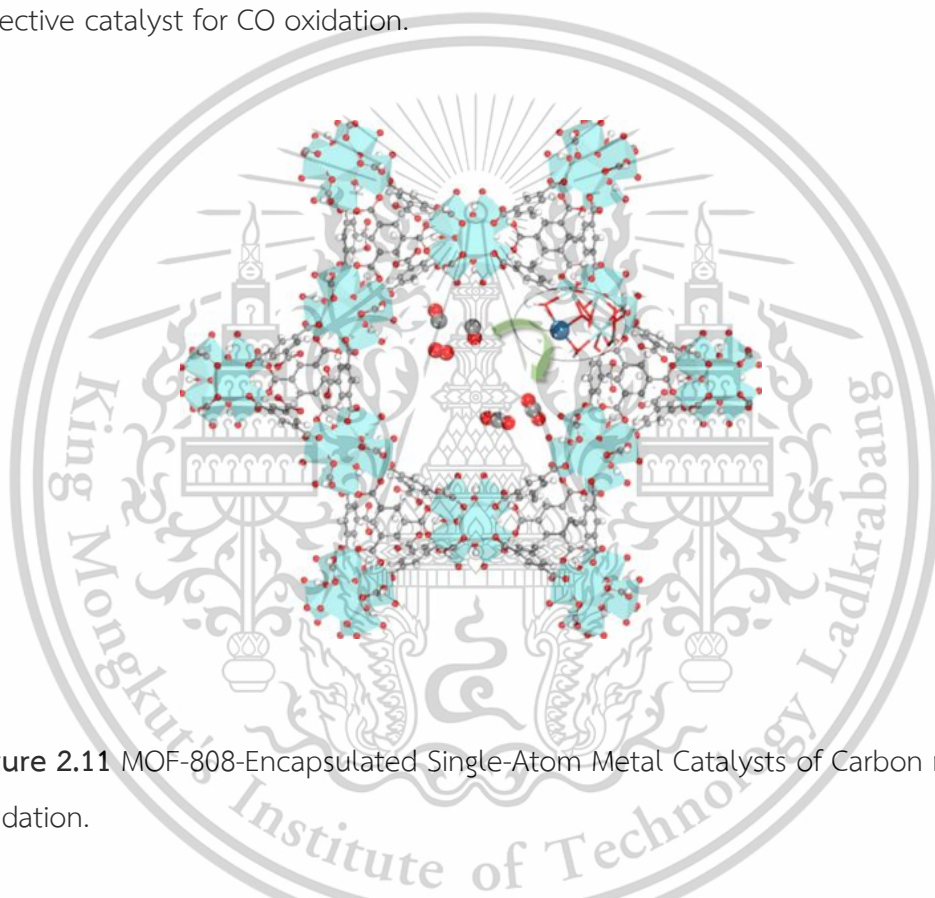


Figure 2.11 MOF-808-Encapsulated Single-Atom Metal Catalysts of Carbon monoxide oxidation.

Liu J. et al. [24] studied CO₂ hydrogenation to C1 product (HCOOH, H₂CO, H₃COH, CO and CH₄) via formate pathway and carboxyl pathway. They evaluated the stability of five metal atoms in 2+ oxidation state (M^{II} = Cu^{II}, Fe^{II}, Pt^{II}, Ni^{II}, and Pd^{II}) encapsulated in MOF-808, selecting Cu^{II}-MOF-808 as the catalyst for CO₂ hydrogenation. Using DFT calculations with the B3LYP functional and the 6-31G(d,p)/LANL2DZ basis set, they explored HCOOH, H₂CO, and H₃COH formation via the formate pathway and CO and CH₄ formation via the carboxyl pathway. The formate pathway was energetically more favorable, with hydroxyl groups promoting C1 product desorption. TOF values for CO₂ conversion to methanol were calculated for five M^{II}-

This material is reserved for educational use only, not allowed for commercial use.

Forbidden to modify the content, and cite the document when use.

MOF-808 catalysts using the ESM model, with Cu^{II}-MOF-808 achieving the highest relative TOF of 1.00 and Pd^{II}-MOF-808 at 0.062 at 523.15 K. These results indicate that Cu^{II}-MOF-808 has the highest catalytic activity for CO₂ conversion to methanol, followed by Pd^{II}-MOF-808.

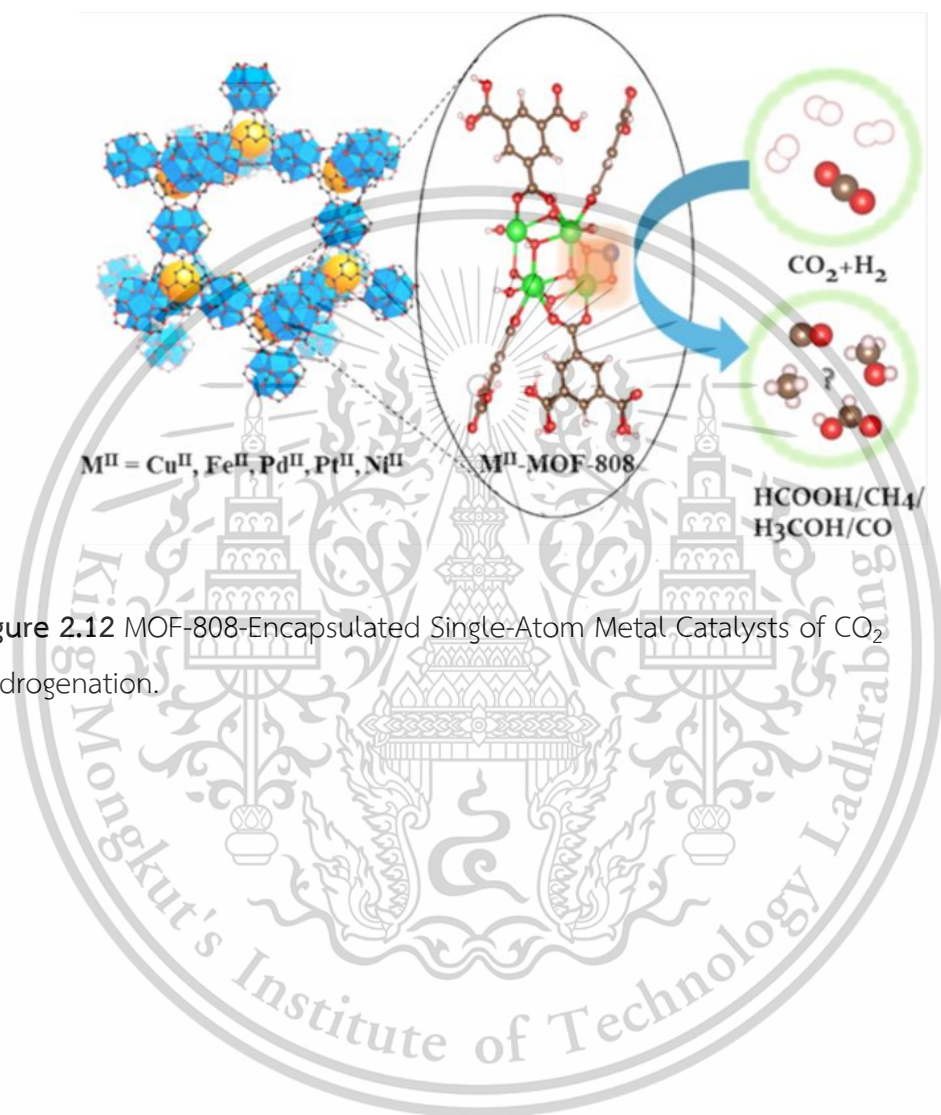


Figure 2.12 MOF-808-Encapsulated Single-Atom Metal Catalysts of CO₂ hydrogenation.

Chapter 3

Research methodology

3.1 Model

A finite-cluster model was employed to investigate the hydrogenation of CO₂ to formic acid on Co and Cu single-atom catalysts supported on MOF-808. The Zr-oxide cluster utilized in this model was derived from the crystal structure of MOF-808 [15], with the carboxylate groups of the 1,3,5-benzenetricarboxylate (BTC³⁻) linkers truncated and capped by hydrogen atoms. Consistent with prior research [23] demonstrating the successful post-synthetic metalation of Zn²⁺-supported MOF-808, Co and Cu single-atom catalysts were incorporated into the Zr-oxide cluster. This was achieved by replacing the capping formate groups at the Zr-node with hydroxide (OH⁻) and water (H₂O) molecules. To generate vacant coordination sites, one H₂O molecule and two protons, one from a terminal hydroxyl group and another from the μ₃-OH position were removed from the Zr-node. These coordination sites were subsequently occupied by Co and Cu atoms. The structural models of the catalyst cluster, both pre- and post-metalation, are depicted in Figure 3.1.

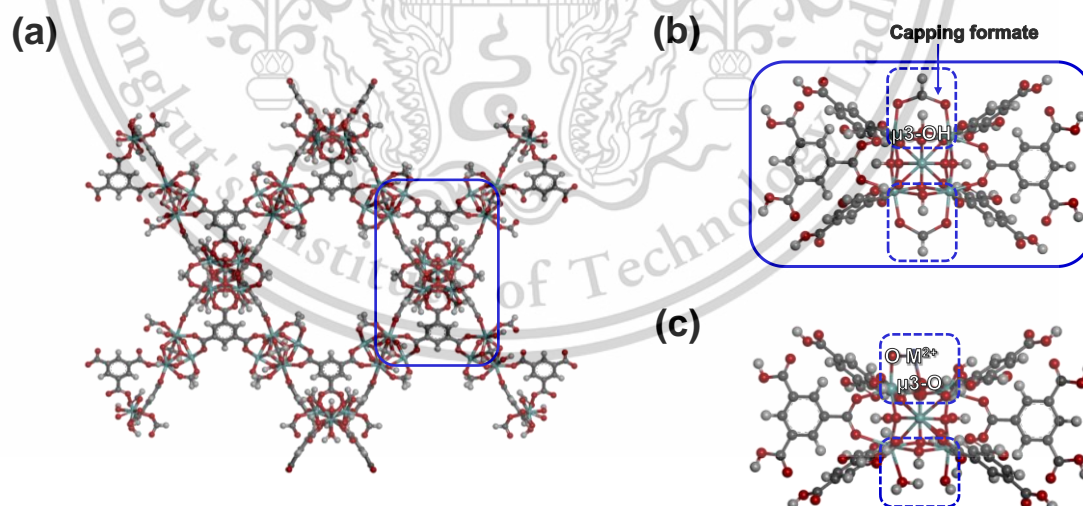


Figure 3.1 (a) Structure of MOF-808 and (b) Cluster models pre-metalation (c) Cluster models post-metalation with Co and Cu single atoms.

3.2 Method

In this study, density functional theory (DFT) calculations were performed using the uM06-L density functional [39]. The def2-SVP basis set [40] was employed for C, H, and O atoms, while the SDD pseudopotential basis set [41] was utilized for Cu, Co and Zr transition metal atoms. During geometry optimization, only terminal carbon atoms were constrained. Natural Bond Orbital (NBO) analysis [42] was conducted to examine the charge distribution within the system. Gibbs free energies were calculated at 298.15 K and 1 atm, with frequency calculations performed at the M06-L/def2-TZVP level, including the Grimme D3 dispersion correction [43]. All calculations were carried out using Gaussian 16 [44]. To investigate the spin states of the catalyst models, all possible spin states were considered. The calculations indicated that the doublet and quartet spin states correspond to the ground states for Cu²⁺- and Co²⁺-MOF-808, with the relative energies presented in Table 3.1.

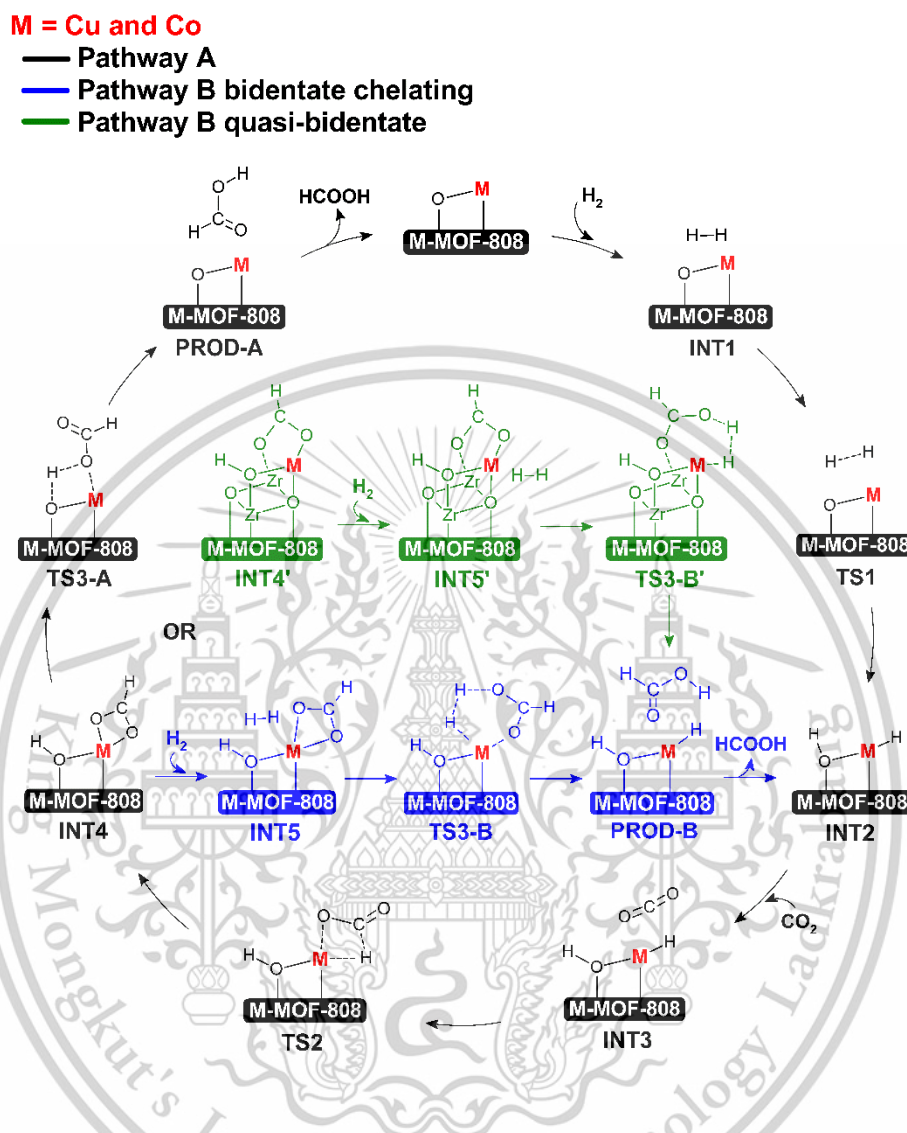
Table 3.1 The relative energies of Co²⁺- and Cu²⁺-MOF-808 in all possible spin states were computed using the uM06-L/def2-SVP level of theory

Spin states	Relative Energy (kcal/mol)	
	Co ²⁺ -MOF-808	Cu ²⁺ -MOF-808
Doublet	8.2	0.0
Quartet	0.0	54.4
Sextet	45.6	131.7
Octet	208.4	208.4

Gibbs free energy profiles were calculated as:

$$\Delta G = G_{\text{gas}/M^{2+}\text{-MOF-808}} - (G_{\text{(gas)}} + G_{M^{2+}\text{-MOF-808}}) \quad (1)$$

where $G_{\text{gas}/M^{2+}\text{-MOF-808}}$ represents the Gibbs free energy of the complex, while $G_{\text{(gas)}}$ and $G_{M^{2+}\text{-MOF-808}}$ denote the Gibbs free energies of the respective gas molecule and the M^{2+} -MOF-808 catalyst, respectively.

3.3 Proposed mechanism for hydrogenation of CO₂ to formic acid

Scheme 3.1 Two possible pathways for hydrogenation of CO₂ to formic acid using H₂ over Co- and Cu-MOF-808 catalysts.

Scheme 3.1, illustrates the proposed reaction mechanism for the hydrogenation of CO₂ over Co- and Cu-MOF-808 catalysts. The mechanism is divided into 2 pathways: Pathway A: without introducing a second H₂ molecule and Pathway B: with introducing a second H₂ molecule, which in the mechanism of Pathway B, two intermediates were identified: a bidentate chelating intermediate (INT4) and a quasi-bidentate intermediate (INT4').

Chapter 4

Main results and discussion

4.1 Structure, electronic properties and stability of Co^{2+} - and Cu^{2+} -MOF-808

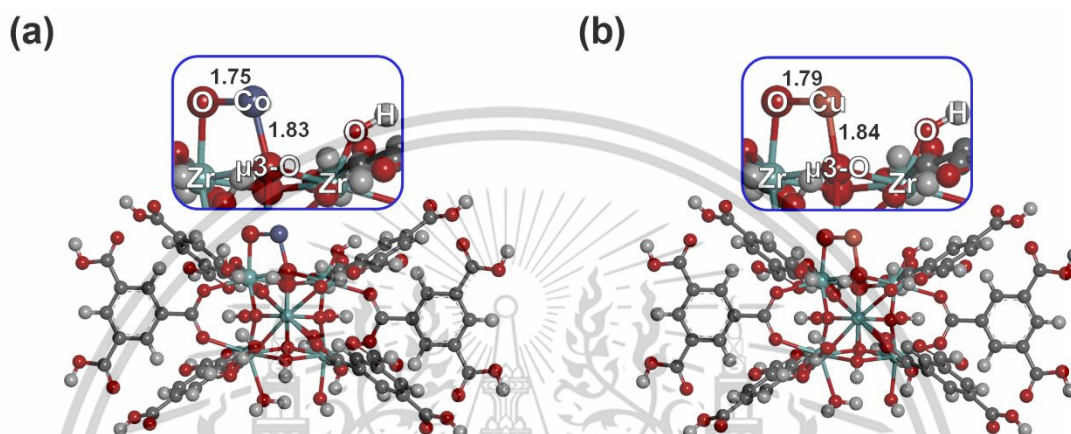


Figure 4.1 (a) Optimized structures of Co^{2+} -MOF-808 and (b) Optimized structures of Cu^{2+} -MOF-808. (Bond lengths are in Å.)

Figure 4.1 depicts the optimized structures of the catalysts in their most stable spin configurations, with Co^{2+} -MOF-808 adopting a quartet spin state and Cu^{2+} -MOF-808 exhibiting a doublet spin state. Table 3.1 summarizes the relative energies corresponding to all possible spin states for Co^{2+} - and Cu^{2+} -MOF-808. The optimized geometries indicate that both Co and Cu ions are coordinated with two oxygen atoms: one from the μ_3 -O atom and the other from the terminal oxygen atom of a neighboring Zr atom within the Zr-oxide cluster. The average C–O bond lengths are approximately 1.8 Å. Moreover, the calculated charges of Co and Cu are 1.16 |e| and 1.11 |e|, respectively, while the coordinated oxygen atoms exhibit negative charges close to -1 |e|. These results confirm that the Co and Cu species exist as Co^{2+} and Cu^{2+} ions, although their effective charges are slightly lower than the ideal +2 due to the influence of metal–oxygen coordination bonding. Consistent with prior research [24], the stability of Co^{2+} and Cu^{2+} ions supported on the MOF-808 framework was evaluated through replacement energy calculations. The calculated replacement Gibbs free

This material is reserved for educational use only, not allowed for commercial use.

energies are -200.7 kcal/mol for Co-MOF-808 and -245.2 kcal/mol for Cu-MOF-808, indicating strong stability of the metal ions within the MOF structure. The replacement Gibbs free energies for Co-MOF-808 and Cu-MOF-808 are significantly more negative than the bulk cohesive energies of their respective metallic phases, which are -101.2 kcal/mol per atom for Co and -80.5 kcal/mol per atom for Cu [57]. This comparison strongly suggests that Co^{2+} and Cu^{2+} ions are exceptionally stabilized on the MOF-808 framework, effectively preventing aggregation into clusters. The strong coordination of these metal ions with the MOF structure not only reinforces their stability but also highlights their potential as highly efficient single-atom catalysts for the hydrogenation of carbon dioxide to formic acid.

4.2 Reaction mechanisms of CO_2 hydrogenation to formic acid

Numerous studies have explored the hydrogenation of CO_2 with H_2 utilizing single-atom catalysts supported on materials such as metal-organic frameworks (MOFs), zeolites, and carbon-based substrates [23,24,53,58–66]. This reaction typically commences with the adsorption and dissociation of H_2 , followed by the hydrogenation of CO_2 via intermediates, including formate (HCOO) and carboxyl (COOH). Among these, the formate pathway is the most frequently observed mechanism as shown in Table 4.1. However, the formate intermediate exhibits a strong affinity for catalytic sites, binding in a bidentate configuration. This results in a significant energy barrier for its subsequent transformation into formic acid (HCOOH). To overcome this limitation, the introduction of a second H_2 molecule has been demonstrated as an effective approach to reduce this energy barrier.

Table 4.1 Gibbs free energy of INT3, TS2 and INT4 for HCOO and COOH over Co^{2+} - and Cu^{2+} -MOF-808

Species	Co-MOF-808 (ΔG , kcal/mol)		Cu-MOF-808 (ΔG , kcal/mol)	
	HCOO	COOH	HCOO	COOH
INT3	-31.3	-31.3	-28.0	-28.0
TS2	-18.2 ($E_a=13.1$)	28.8 ($E_a = 60.1$)	-16.8 ($E_a=11.2$)	19.0 ($E_a=47.0$)
IN4	-45.4	-13.7	-40.8	-13.9

This material is reserved for educational use only, not allowed for commercial use.

Forbidden to modify the content, and cite the document when use.

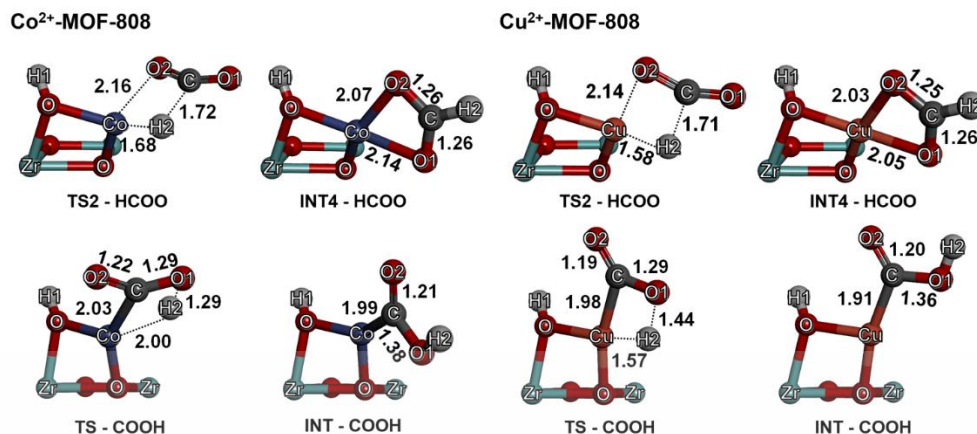


Figure 4.2 Optimized structures of TS and INT for HCOO and COOH over Co- and Cu-MOF-808

Building upon previous studies, we propose potential mechanisms for the hydrogenation of CO₂ with H₂, as outlined in Scheme 3.1. In pathway A, the reaction initiates with the adsorption and dissociation of H₂, followed by a two-step process leading to the formation of formic acid. The first step involves the formation of a formate intermediate, which, in the second step, undergoes transformation into formic acid through a chelating geometry. To reduce the energy barrier associated with formic acid formation, an alternative mechanism, designated as pathway B, introduces a second H₂ molecule in conjunction with the formate intermediate. In contrast to previous studies, our results reveal the existence of the formate intermediate in both quasi-bidentate and chelating geometries, which facilitates the incorporation of the second H₂ molecule, thereby enhancing the efficiency of the reduction to formic acid. The subsequent sections provide a detailed discussion of these proposed reaction mechanisms.

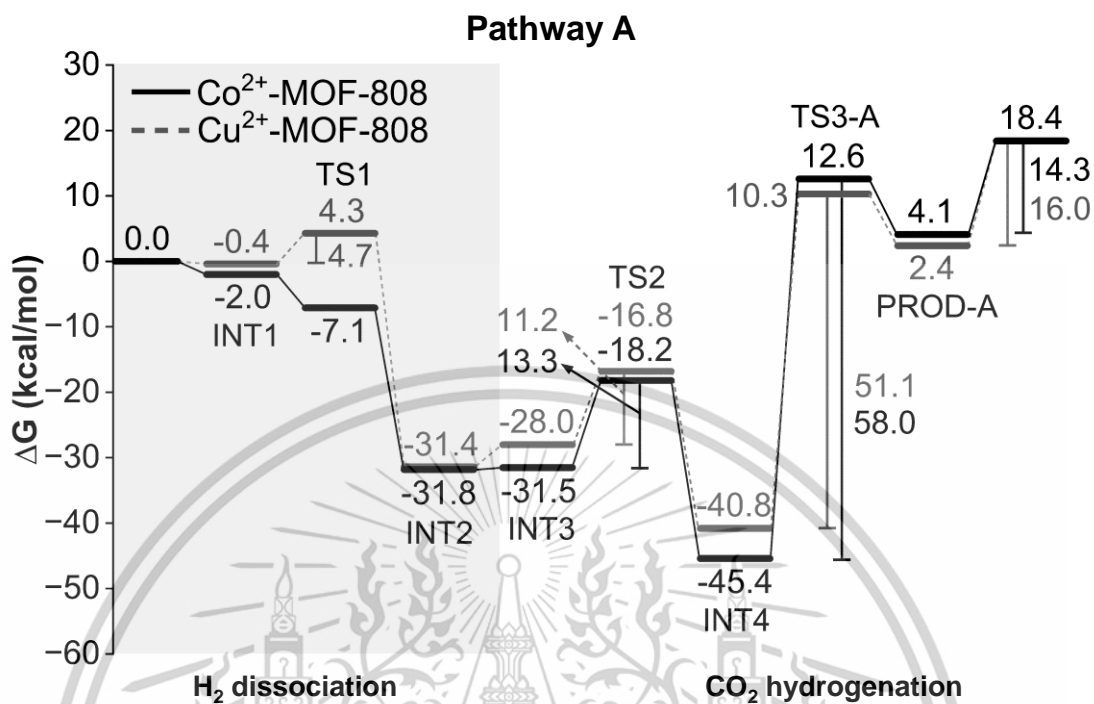
4.2.1 Pathway A: without introducing a second H₂ molecule

Figure 4.3 Gibbs free energy profile of CO₂ hydrogenation to formic acid via the chelating formate intermediate in pathway A over Co²⁺ and Cu²⁺-MOF-808.

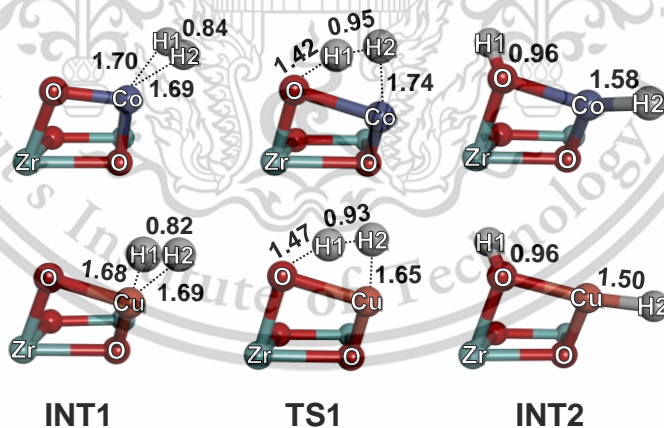


Figure 4.4 The optimized structures of INT1, TS1 and INT2 of H₂ adsorption and H₂ dissociation step.

Figure 4.3 illustrates the energy profile of CO₂ hydrogenation on Co²⁺- and Cu²⁺-MOF-808 via pathway A, while their corresponding optimized structures are displayed in Figure 4.4. The calculated adsorption energies of H₂ are -2.0 kcal/mol for Co²⁺-MOF-808 and -0.4 kcal/mol for Cu²⁺-MOF-808. In the optimized structures (INT1), the H–H bond length is notably elongated to approximately 0.8 Å, compared to the bond length of the isolated H₂ molecule, which measures approximately 0.7 Å. This elongation indicates the activation of H₂ upon adsorption. Moreover, the intermolecular distances between the activated H₂ and Co²⁺ and Cu²⁺ sites are approximately 1.7 Å.

After activation, H₂ undertakes dissociation via the transition state (TS1) with an energy barrier of 4.7 kcal/mol for and Cu²⁺-MOF-808, which aligns closely with the 7.7 kcal/mol barrier reported in previous studies [24]. Notably, for Co²⁺-MOF-808 this process is barrierless in terms of Gibbs free energy (ΔG); however, it presents an activation energy barrier (ΔE) of 7.5 kcal/mol, as detailed in the Supporting Information. These energy barriers fall within the range of 7.7–26.7 kcal/mol previously observed for H₂ dissociation over M²⁺-MOF-808 catalysts [24]. At this stage, the bond distance of activated H₂ is further extended by approximately 0.1 Å, compared to the preceding step. Additionally, one hydrogen atom (H1) approaches the terminal oxygen atom, while the other hydrogen atom (H2) remains coordinated to the Co²⁺ and Cu²⁺ sites. Charge analysis of TS1 reveals that H1 carries a positive charge of approximately +0.2 |e|, while H₂ exhibits a negative charge of -0.2 |e|, indicating that the dissociation of H₂ proceeds via heterolytic cleavage. The transition states are characterized by imaginary vibrational frequencies of 488.3i cm⁻¹ and 593.1i cm⁻¹ for Co²⁺- and Cu²⁺-MOF-808, respectively.

The collapse of TS1 results in the formation of Co- and Cu-hydride species (Co- and Cu-H₂) accompanied by a hydroxyl group (OH1) on the Zr-oxide cluster of MOF-808, corresponding to intermediate structure INT2. This transformation is exergonic, with energy changes of -31.8 kcal/mol for Co²⁺-MOF-808 and -31.4 kcal/mol for Cu²⁺-MOF-808. As summarized in Table S1, the calculated charges on Co and the hydride species are 1.19 |e| and -0.47 |e|, respectively, while for Cu and the hydride species, they are 1.00 |e| and -0.36 |e|, respectively. Furthermore, the bond lengths, as depicted in Figure 4.4, are determined to be 1.58 Å for Co-H and 1.50 Å for Cu-H. The longer

bond length and higher charges observed for Co-H indicate a greater ionic character compared to Cu-H.

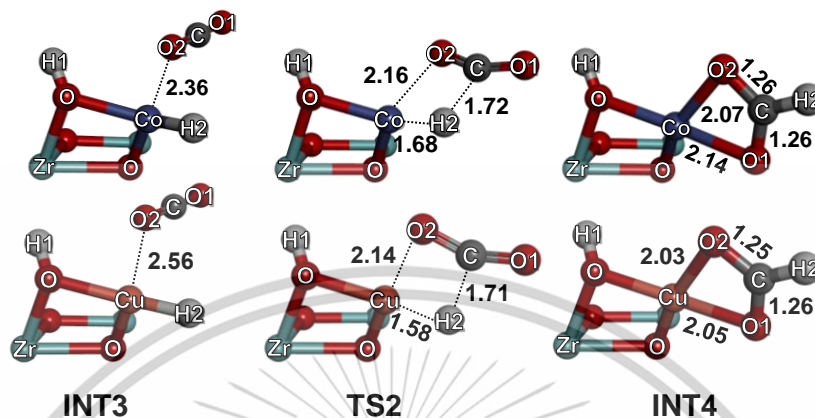


Figure 4.5 Optimized structures of INT3, TS2 and INT4 of the formation of formate intermediate.

The reaction progresses with the adsorption of CO_2 (INT3), as depicted in Figure 4.5. In this step, CO_2 binds weakly to the Co or Cu active site, with intermolecular distances exceeding 2.3 Å. Subsequently, the hydride (H_2) is transferred to the adsorbed CO_2 via the transition state (TS2). Structural analysis of this TS reveals an almost co-planar geometry, as evidenced by the M-O2-C-H2 dihedral angles of -6.0° and -5.9° for Co- and Cu-MOF-808, respectively. The adsorbed CO_2 undergoes significant bending, with bond angles measured at 152.3° for Co-MOF-808 and 154.4° for Cu-MOF-808. The distances between C---H2 and Co---O2/ Cu---O2 distances are approximately 1.7 Å and 2.1 Å, respectively, indicating bond formation. The imaginary vibrational frequencies of the transition states are calculated to be $585.3i \text{ cm}^{-1}$ and $533.6i \text{ cm}^{-1}$ for Co^{2+} - and Cu^{2+} -MOF-808, corresponding to the formation of the C-H2 bond and the cleavage of Co-H2 and Cu-H2 bonds. The energy barriers for this step are 13.3 kcal/mol for Co-MOF-808 and 11.2 kcal/mol for Cu-MOF-808, aligning with previously reported energy barriers for CO_2 hydrogenation on metal hydrides, which range between 8.5 and 16.8 kcal/mol. [24,59].

The collapse of TS2 results in the formation of a formate intermediate adopting a bidentate-chelating structure, designated as INT4. This intermediate is significantly

This material is reserved for educational use only, not allowed for commercial use.

Forbidden to modify the content, and cite the document when use.

more stable than TS2, with energy differences of 27.5 kcal/mol for Co-MOF-808 and 24.0 kcal/mol for Cu-MOF-808. In INT4, the C–O1 and C–O2 bond lengths are approximately measured at 1.25 Å. Additionally, the metal–O bond lengths between the formate intermediate and the Co and Cu active sites are 2.05 Å, confirming the bidentate-chelating configuration.

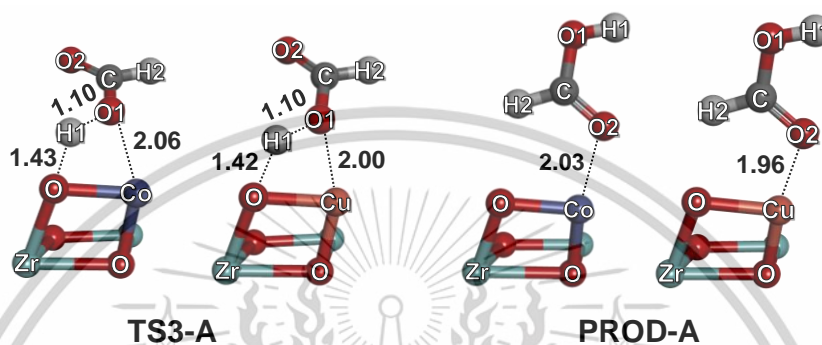


Figure 4.6 Optimized structures of TS3-A and PROD-A for the formic acid formation.

The formation of formic acid occurs through the transition state (TS3), which involves the transfer of a proton (H1) from hydroxyl group (OH1) to an oxygen atom (O2) of the formate intermediate. Natural Bond Orbital (NBO) charge analysis reveals that H1 carries a charge of 0.55 |e| for Co-MOF-808 and 0.56 |e| for Cu-MOF-808. The imaginary vibrational frequencies of TS3 are calculated to be 820.7i cm^{-1} and 794.0i cm^{-1} for Co^{2+} - and Cu^{2+} -MOF-808, respectively, corresponding to the proton transfer from OH1 to the formate intermediate, the formation of the C–H2 bond, and the cleavage of the Co–H and Cu–H bonds. As illustrated in Figure 4.6, the O---H1 and H1--O2 distances in TS3 are approximately 1.4 Å and 1.1 Å for both catalysts. Compared to INT4, the Co–O2 and Cu–O2 bond lengths remain unchanged, while the Co–O1 and Cu–O1 bonds break entirely, causing the O1 atom to orient upward. These structural changes contribute to a substantial energy barrier, calculated as 58.3 kcal/mol for Co-MOF-808 and 51.1 kcal/mol for Cu-MOF-808. This high energy barrier imposes the second hydrogenation step as the most energy demanding, confirming it as the rate-determining step, consistent with previous studies [53,61,65]. However, microkinetic modeling reveals that the actual rate-determining step in the reaction is the desorption of formic acid (HCOOH), which will be discussed in greater detail subsequently. This material is reserved for educational use only, not allowed for commercial use.

Forbidden to modify the content, and cite the document when use.

desorption process requires energy barriers of 14.3 kcal/mol for Co-MOF-808 and 16.0 kcal/mol for Cu-MOF-808, consistent with reported values for formic acid desorption from Cu-embedded graphene [53]. Overall, the hydrogenation of CO₂ to formic acid is endergonic, with an energy change of 18.4 kcal/mol, indicating that the process is thermodynamically unfavorable. This finding is in agreement with the standard Gibbs free energy change (ΔG°_{298}) of 32.9 kJ/mol reported for the reaction [8].

4.2.2 Pathway B: with introducing a second H₂ molecule

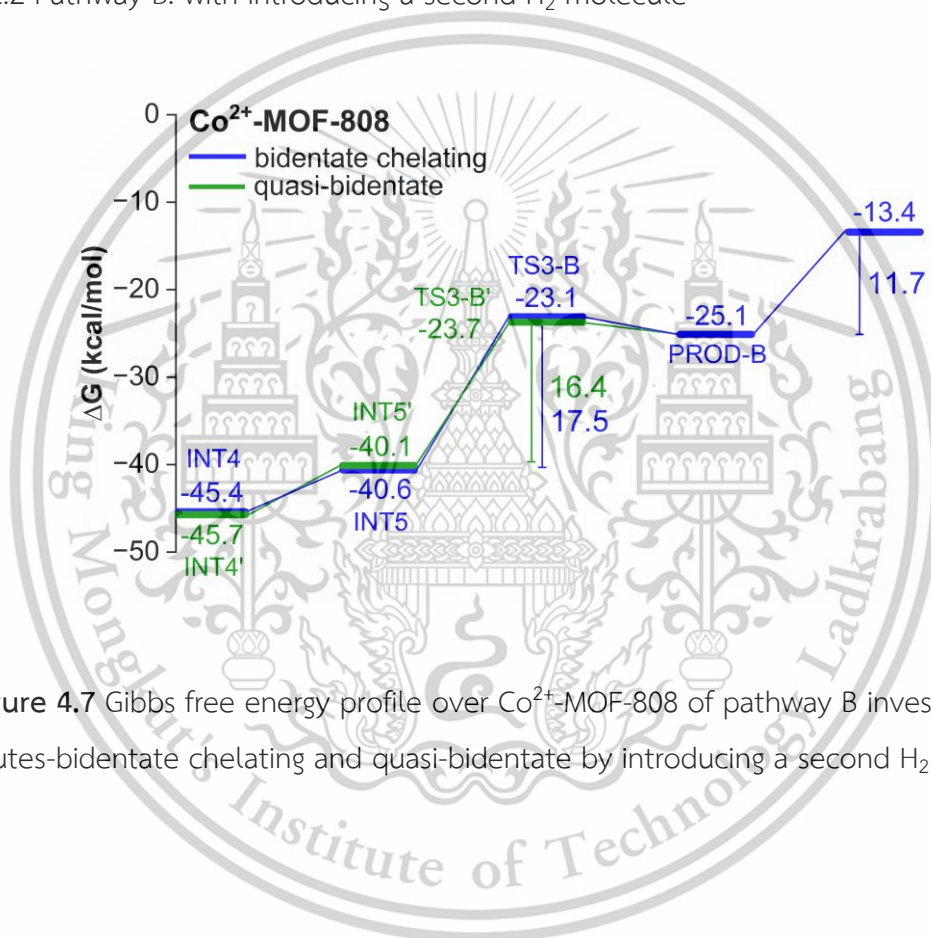
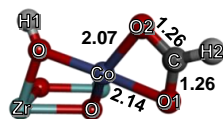


Figure 4.7 Gibbs free energy profile over Co²⁺-MOF-808 of pathway B investigates two routes-bidentate chelating and quasi-bidentate by introducing a second H₂ molecule.

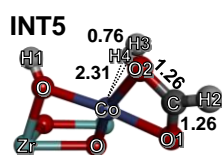
Bidentate chelating

INT4



$$\angle O_{H1}-Co-O1 = 142.2^\circ$$

$$\angle \mu_3O-Co-O2 = 117.3^\circ$$



TS3-B



$$\angle O_{H1}-Co-O1 = 165.2^\circ$$

$$\angle \mu_3O-Co-H4 = 157.6^\circ$$

Quasi-bidentate

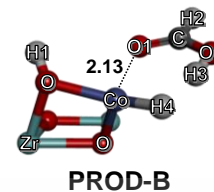
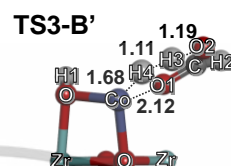
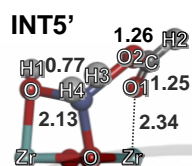
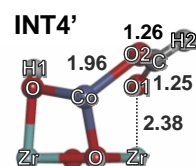


Figure 4.8 Optimized structures of the INT4, INT4', TS3-B, TS3-B', INT5, INT5' and PROD for CO₂ hydrogenation to formic acid using H₂ over Co²⁺-MOF-808.

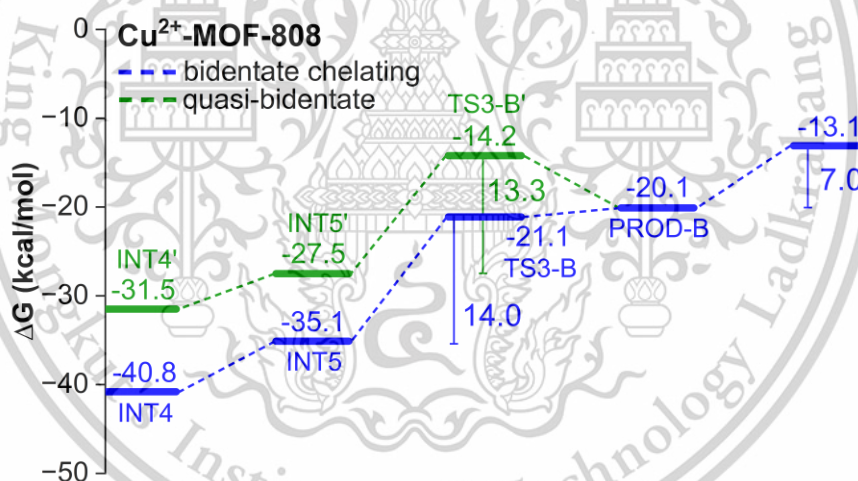
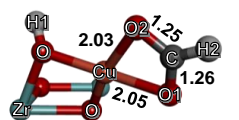


Figure 4.9 Gibbs free energy profile over Cu²⁺-MOF-808 of pathway B investigates two routes-bidentate chelating and quasi-bidentate by introducing a second H₂ molecule.

Bidentate chelating

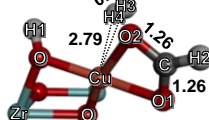
INT4



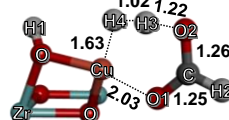
$$\angle \text{O}_{\text{H1}}-\text{Cu}-\text{O1} = 167.0^\circ$$

$$\angle \mu_3\text{O}-\text{Cu}-\text{O2} = 167.7^\circ$$

INT5



TS3-B

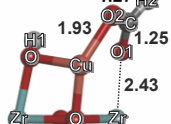


$$\angle \text{O}_{\text{H1}}-\text{Cu}-\text{O1} = 160.4^\circ$$

$$\angle \mu_3\text{O}-\text{Cu}-\text{H4} = 161.7^\circ$$

Quasi-bidentate

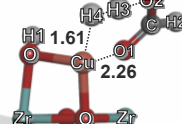
INT4'



INT5'



TS3-B'



PROD-B

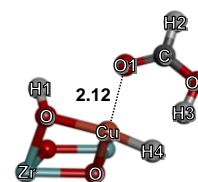


Figure 4.10 Optimized structures of the INT4, INT4', TS3-B, TS3-B', INT5, INT5' and PROD for CO₂ hydrogenation to formic acid using H₂ over Cu²⁺-MOF-808.

The adsorption of the formate intermediate onto a catalyst surface typically occurs in either a bidentate or bridging geometry, depending on the properties of the catalytic surface. In the bidentate configuration, the formate binds to a single catalytic site through both of its oxygen atoms, whereas in the bridging geometry, it interacts with two metal centers. As depicted in Figures 4.8 and 4.10, the formate intermediate (INT4') exhibits C–O bond lengths (~1.25 Å) similar to those observed in the bidentate-chelating structure (INT4). However, in INT4', one oxygen atom (O2) coordinates with a single catalytic site (Co or Cu), while the other oxygen atom (O1) is positioned farther from the adjacent Zr atom of the Zr-oxide node. The Co- and Cu-O2 bond lengths are approximately 1.9 Å and Zr---O1 distances are around 2.4 Å for both Co²⁺- and Cu²⁺-MOF-808 catalysts. This configuration suggests a quasi-bidentate geometry in INT4' [67].

Upon introducing a second H₂ molecule alongside the quasi-bidentate and bidentate-chelating geometries, the distances between the formate intermediate and the Co or Cu site increase slightly, resulting in the configurations INT5 and INT5' (Figure 4.8 and 4.10). This elongation arises from the adsorption of the second H₂ molecule at the Co or Cu site adjacent to the formate intermediate, creating H₂-formate co-adsorption geometries. In these configurations, the intermolecular distance between the adsorbed H₂ molecule and the Co or Cu site is approximately 2.0 Å, while the bond

length within the adsorbed H₂ molecule is around 0.8 Å. This adsorption process is mildly endergonic, with an energy increase of approximately 5 kcal/mol for both the quasi-bidentate and bidentate-chelating pathways in the Co- and Cu-MOF-808 catalysts.

Table 4.2 The vibrational modes of the formate intermediate in both chelating and quasi-bidentate geometries on Co- and Cu-MOF-808 catalysts.

vibrational mode	Co-MOF-808		Cu-MOF-808	
	wavenumber (cm ⁻¹)	Δ (cm ⁻¹)	wavenumber (cm ⁻¹)	Δ (cm ⁻¹)
chelating $\nu_s(\text{OCO})$	1402	201	1405	181
chelating $\nu_{as}(\text{OCO})$	1603		1586	
quasi-bidentate $\nu_s(\text{OCO})$	1389	213	1389	203
quasi-bidentate $\nu_{as}(\text{OCO})$	1602		1592	

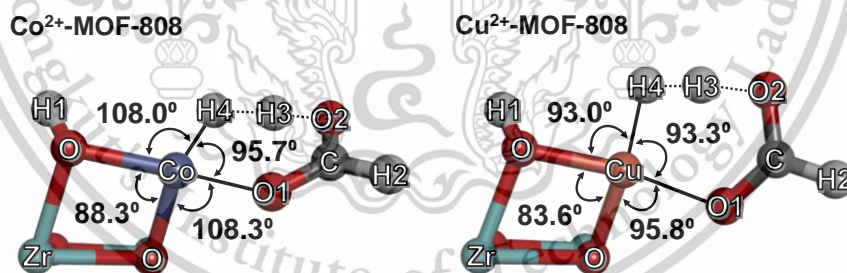


Figure 4.11 The structure of TS3-B shows Co in a slightly distorted square planar geometry, while Cu adopts an almost perfect square planar arrangement.

The formation of formic acid progresses through the transition state (TS3-B and TS3-B'), where the H3-H4 bond of the second H₂ molecule undergoes cleavage, and the resulting hydrogen atoms are transferred to the Co/Cu site and the formate intermediate. During this transition, the H3-H4 bond length extends from 0.8 Å to 1.0 Å. This material is reserved for educational use only, not allowed for commercial use.

Forbidden to modify the content, and cite the document when use.

Å, while the Co---H4 and Cu---H4 distances decrease to 1.7 Å. For Co²⁺-MOF-808, the transition states exhibit imaginary frequency values of 540.9i cm⁻¹ and 784.3i cm⁻¹ for the bidentate-chelating and quasi-bidentate pathways, respectively. Similarly, for Cu²⁺-MOF-808, the frequencies are 949.1i cm⁻¹ and 889.9i cm⁻¹, corresponding to the simultaneous cleavage of the H3-H4 bond and formation of O2-H3 and Co/Cu-H4 bonds. The energy barriers for this step are 16.4 kcal/mol and 17.5 kcal/mol for the quasi-bidentate and bidentate-chelating pathways in Co²⁺-MOF-808. In contrast, Cu²⁺-MOF-808 demonstrates lower barriers of 13.3 kcal/mol and 14.0 kcal/mol for the same pathways, indicating that Cu more effectively facilitates this step. This enhanced facilitation is attributed to the stronger Jahn-Teller stabilization observed in the Cu²⁺ (d⁹) doublet state compared to Co²⁺ (d⁷) high-spin quartet state [43]. The Jahn-Teller effect is evident in the TS3-B structure, where Cu adopts a near-square planar geometry. This configuration is stabilized by bond angles of approximately 90° and 160°, closely approximating the ideal angles of a square planar geometry (90° and 180°), as depicted in Figure 4.11. Conversely, Co, with a weaker Jahn-Teller effect, exhibits a reduced tendency for square planar geometry, leading to higher energy barriers for Co²⁺-MOF-808. Furthermore, introducing a second H₂ molecule in pathway B significantly lowers the energy barrier for converting the formate intermediate to formic acid, reducing it by approximately threefold compared to pathway A.

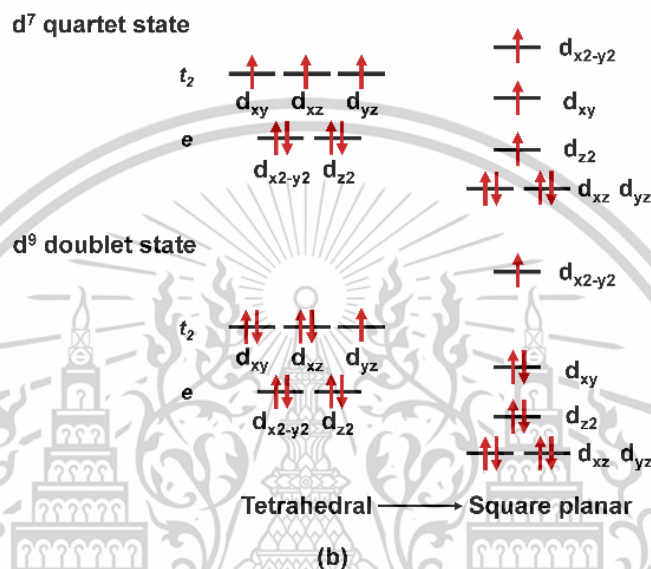
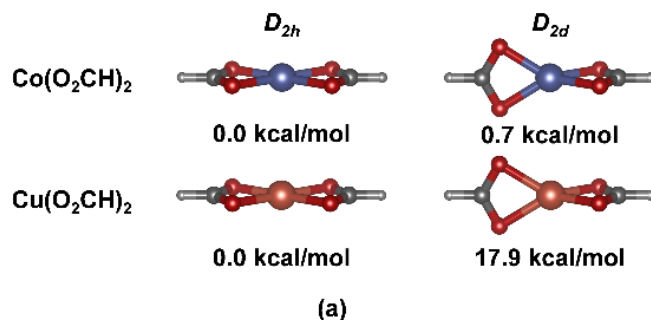


Figure 4.12 (a) Optimized structures of $\text{Co}(\text{O}_2\text{CH})_2$ and $\text{Cu}(\text{O}_2\text{CH})_2$ with imposed symmetry constraints, highlighting their energetic stabilities relative to the most stable configurations in D_{2h} and D_{2d} symmetries. (b) A schematic representation of d-orbital splitting in d^7 and d^9 ML_4 complexes.

To elucidate the stability differences between the bidentate-chelating and quasi-bidentate pathways, the electronic properties of the Co^{2+} and Cu^{2+} metal sites were investigated using simplified models: $\text{Co}(\text{O}_2\text{CH})_2$ and $\text{Cu}(\text{O}_2\text{CH})_2$. These models represent Co^{2+} and Cu^{2+} coordinated to four oxygen atoms of formate ligands, mimicking their coordination environment in MOFs. Formate ligands were chosen due to their structural similarity to the system and their weak coordination, which stabilizes Co^{2+} in a high-spin quartet state. Typically, metal complexes with a coordination number of four (ML_4) adopt either square planar or tetrahedral geometries. Figure 4.12(a) illustrates the structures of $\text{Co}(\text{O}_2\text{CH})_2$ and $\text{Cu}(\text{O}_2\text{CH})_2$ under symmetry constraints, along with their relative energetic stabilities. The $\text{Cu}(\text{O}_2\text{CH})_2$ complex favors

This material is reserved for educational use only, not allowed for commercial use.

a square planar configuration with D_{2h} symmetry over a quasi-tetrahedral, non-planar configuration with D_{2d} symmetry, exhibiting a greater stability by 17.9 kcal/mol. In contrast, both geometries of $\text{Co}(\text{O}_2\text{CH})_2$ display nearly equivalent stabilities, with the square planar geometry being slightly more stable at 0.7 kcal/mol. This finding highlights the flexibility of Co^{2+} structure, which can be easily adapted to different geometries, such as octahedral or tetrahedral, depending on the coordination number. However, it is important to note that an ideal tetrahedral geometry is unattainable due to the chelating nature of the formate ligands.

To illustrate the electronic and Jahn-Teller effects, a schematic diagram of the d-orbital splitting diagram for ML_4 complexes in both tetrahedral and square planar geometries are shown Figure 4.12(b). For the Cu^{2+} (d^9) configuration, tetrahedral geometry reduces to square planar geometry, lifting the degeneracy of the t_2 orbital set and stabilizing the system. This reduction results in an elevation of the energy of the singly occupied $d_{x^2-y^2}$ orbital, highlighting the influence of the Jahn-Teller effect, which strongly favors the square planar geometry. In contrast, the Co^{2+} (d^7) in a high-spin quartet state exhibits nearly equivalent stability in both tetrahedral and square planar geometries. This is attributable to the electronic structure of Co^{2+} (d^7), characterized by three singly occupied orbitals. The degree of orbital splitting during the transition from tetrahedral to square planar symmetry is less pronounced for Co^{2+} compared to Cu^{2+} . Unlike Cu^{2+} (d^9), where significant Jahn-Teller distortion substantially destabilizes the $d_{x^2-y^2}$ orbital, the orbital splitting in Co^{2+} experiences relatively minor orbital splitting. Consequently, the $d_{x^2-y^2}$ orbital in Co^{2+} is only slightly higher in energy than the other two singly occupied orbitals, resulting in comparable stabilities for both geometries.

In summary, these calculations demonstrate how electronic and Jahn-Teller effects affect the stability of Co^{2+} and Cu^{2+} in tetrahedral and square planar geometries. This analysis provides valuable insights into the distinct stabilities of the bidentate-chelating and quasi-bidentate pathways. Specifically, the bidentate-chelating configuration is more stable than the quasi-bidentate pathway for Cu^{2+} -MOF-808, whereas both pathways exhibit comparable stabilities for Co^{2+} -MOF-808. This difference arises from the strong preference of Cu^{2+} for square planar coordination, a preference reinforced by the Jahn-Teller effect. This phenomenon is evident in the

This material is reserved for educational use only, not allowed for commercial use.

Forbidden to modify the content, and cite the document when use.

trans bond angles of the bidentate-chelating intermediate (INT4), where Cu^{2+} -MOF-808 exhibits angles of close to 167° , compared to the more distorted angles of 142° and 117° observed for Co^{2+} -MOF-808, as illustrated in Figures 4.8 and 4.10.

The desorption of formic acid occurs with activation energies for Co^{2+} -MOF-808 is 11.7 kcal/mol and for Cu^{2+} -MOF-808 is 7.0 kcal/mol. These energy barriers are significantly lower compared to those observed in pathway A, likely attributed to the adsorption of formic acid on Co- and Cu-hydride sites instead of the open Co and Cu single-atom sites. This adsorption mechanism promotes more facile interactions, thereby reducing the desorption energy requirements. In pathway B, the completion of the second CO_2 hydrogenation step regenerates the Co- and Cu-hydride sites, enabling subsequent cycles of CO_2 hydrogenation. This hydrogenation process is exergonic, releasing approximately 13 kcal/mol, which indicates favorable thermodynamics. Importantly, the introduction of a second H_2 molecule plays a crucial role in this reaction, significantly reducing the energy barrier for the transformation of the formate intermediate into formic acid. Additionally, it shifts the overall reaction thermodynamics from endergonic to exergonic, suggesting that the rate of formic acid formation could be influenced by H_2 concentration. Moreover, the lower energy barrier calculated for Cu in density functional theory (DFT) simulations highlights its superior catalytic performance in the CO_2 hydrogenation reaction.

4.2.3. Microkinetic modeling

Mean-field microkinetic modeling (MKM) was conducted employing a dual-site model representation, incorporating Cu/Co (*) and oxygen (#) atoms of Co^{2+} - and Cu^{2+} -MOF-808. The ratio of * and # sites was set at 0.5:0.5. Key parameters including reaction rate, surface coverages, reaction order, and degree of rate control (DRC) were computed under conditions of 1 bar, an H_2 : CO_2 ratio of 1:1, temperatures ranging from 473 K to 823 K. The primary focus of the analysis was on determining the turnover frequency (TOF) for formic acid (HCOOH) production. All elementary reaction steps involved in the hydrogenation of CO_2 to HCOOH over Co^{2+} - and Cu^{2+} -MOF-808, as outlined in Table S8, were systematically incorporated into the MKM simulations.

The findings indicate that Cu^{2+} -MOF-808 demonstrates a higher turnover frequency (TOF) than Co^{2+} -MOF-808 at temperatures below 673 K. However, at

temperatures exceeding 673 K, Co^{2+} -MOF-808 outperforms Cu^{2+} -MOF-808 in TOF, as depicted in Figure 4.13(a). A detailed analysis of the contributions from each reaction pathway to the TOF reveals that pathway A has an insignificant impact on the overall reaction. In contrast, pathways B (bidentate chelating) and B' (quasi-bidentate) dominate the reaction for both catalysts. At elevated temperatures, the TOF for formic acid (HCOOH) production via pathways B and B' increases more sharply for Co^{2+} -MOF-808 compared to Cu^{2+} -MOF-808, accounting for its superior performance under these conditions. Additionally, the optimal temperature for HCOOH production for both catalysts is predicted to be approximately 723 K.

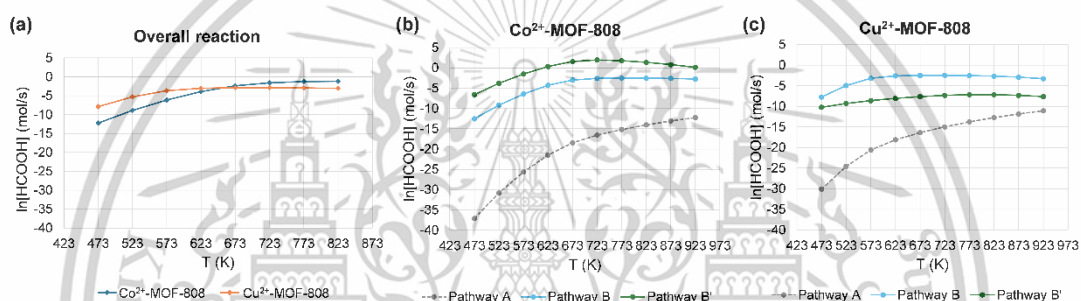


Figure 4.13 Turnover frequency (TOF) for HCOOH production is analyzed as a function of temperature: (a) overall reaction mechanisms, (b) TOF over Co^{2+} -MOF-808 and (c) over Cu^{2+} -MOF-808. Pathway B and B'.

The degree of rate control (DRC) analysis, as presented in Figure 4.14, identifies the desorption of formic acid (HCOOH) from the H^* site as the rate-determining step for both catalysts. This observation is consistent with density functional theory (DFT) calculations performed at the uM06L/def2-TZVP/SDD level of theory, which indicate that the desorption energy of HCOOH in both pathway B (bidentate chelating) and pathway B' (quasi-bidentate) exceeds the energy barrier associated with the most demanding reaction step: the second hydrogenation of CO_2 hydrogenation to formic acid (refer to the Supplementary Information). Furthermore, the hydrogenation of the formate intermediate (HCOO^*) in pathways B and B' ($\text{H}_2\text{-HCOO}^* \leftrightarrow \text{H-HCOOH}^*$ and $\text{H}_2\text{-HCOOz}^* \leftrightarrow \text{H-HCOOH}^*$) exerts minimal influence on the overall reaction rate at temperatures above 623 K. Figure 4.15 illustrates that the # sites are predominantly

occupied by hydrogen atoms (H#), which are primarily utilized in pathway A, a minor mechanism for both catalysts. At temperatures below 673 K for Co²⁺-MOF-808 and approximately 530 K for Cu²⁺-MOF-808, the formate intermediate (HCOO*) exhibits the second-highest surface coverage. However, at elevated temperatures, the concentration of HCOO* diminishes while that of H* increases, driven by the interaction with a second H₂ molecule, ultimately promoting formic acid formation. The introduction of a second H₂ molecule significantly enhances the catalytic activity of both Co²⁺- and Cu²⁺-MOF-808 for formic acid production. This enhancement is corroborated by reaction order analysis (Figure S9), which indicates that the reaction rate is predominantly governed by H₂ concentration, with CO₂ exerting a notable effect only at higher temperatures.

Microkinetic modeling (MKM) simulations indicate that Cu²⁺-MOF-808 demonstrates superior performance compared to Co²⁺-MOF-808 in the hydrogenation of CO₂ to formic acid at temperature below 673 K. However, at elevated temperatures, Co²⁺-MOF-808 exhibits higher catalytic activity. To ensure the stability of single-atom catalysts within the MOF framework and to mitigate the risk of cluster formation, maintaining the reaction temperature below 573 K is recommended. This condition underscores the suitability of Cu²⁺-MOF-808 for achieving an optimal balance between catalytic activity and structural stability. The incorporation of adding H₂ molecule in pathway B emerges as a critical factor in enhancing formic acid production. Furthermore, the desorption of formic acid, identified as the rate-determining step for both catalysts, significantly influences overall reaction efficiency. These findings highlight the necessity of strategies aimed at reducing desorption energy or facilitating product release to optimize catalytic performance.

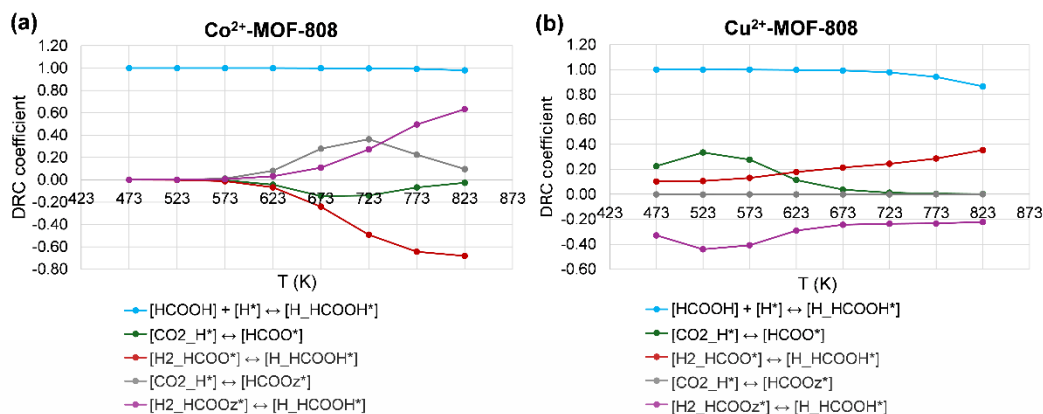


Figure 4.14 Degree of rate control (DRC) as a function of temperature: (a) Co²⁺-MOF-808 and (b) Cu²⁺-MOF-808. Elementary reaction steps with a DRC coefficient of zero are excluded from the analysis.

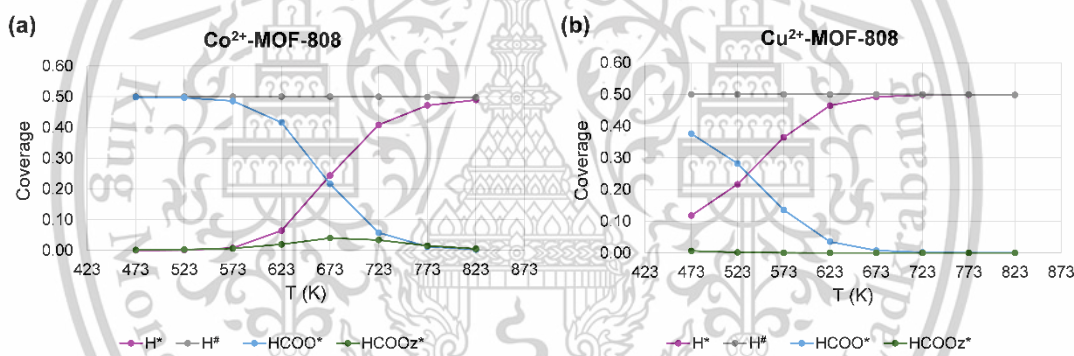


Figure 4.15 Surface coverages as a function of temperature: (a) Co²⁺-MOF-808 and (b) Cu²⁺-MOF-808. Species with zero surface coverage are omitted from the analysis.

This study provides valuable insights into CO₂ hydrogenation catalyzed by Co²⁺- and Cu²⁺-MOF-808, though several aspects merit further exploration. The finite-cluster model employed effectively captures the structural transformations and local electronic characteristics of single-atom catalysts, which are pivotal for elucidating their catalytic performance and reaction mechanisms. Nevertheless, periodic models may offer a more comprehensive depiction of the MOF framework's rigidity. While such models are computationally intensive due to the extensive unit cells of MOFs, they could impose stricter constraints on structural flexibility, potentially enhancing accuracy. However, we anticipate that the influence on reaction energetics would be

This material is reserved for educational use only, not allowed for commercial use.

minimal, with no substantive alterations to the reaction mechanisms proposed in this study. Additionally, the identification of the quasi-bidentate intermediate geometry, in conjunction with the more widely recognized bidentate chelating geometry, represents a novel contribution to the existing literature. This finding would benefit from experimental verification, such as through Fourier Transform Infrared Reflection-Absorption Spectroscopy (FT-IRRAS), which has been previously combined with DFT to characterize similar intermediates [67]. Addressing these limitations in subsequent research would strengthen the validity of our conclusions and broaden their applicability.



This material is reserved for educational use only, not allowed for commercial use.

Forbidden to modify the content, and cite the document when use.

Chapter 5

Conclusions and suggestions

5.1 Conclusions

Density Functional Theory (DFT) calculations and Mean-field microkinetic modeling (MKM) were employed to investigate the reaction mechanism of CO₂ hydrogenation to formic acid catalyzed by Co and Cu single-atom catalysts supported on MOF-808. This study emphasizes two well-defined reaction pathways, designated as pathway A and pathway B. Both pathways encompass the adsorption and dissociation of H₂, culminating in the formation of Co- and Cu-hydride active sites that drive CO₂ hydrogenation process.

The hydrogenation process proceeds through two primary stages: the formation of a formate intermediate, followed by its subsequent conversion into formic acid. The key difference between pathway A and pathway B lies in the second hydrogenation step. In pathway A, the formate intermediate undergoes direct conversion to formic acid without the involvement of an additional H₂. In contrast, pathway B entails the introduction of a second H₂ molecule following the formation of the formate intermediate, thereby facilitating the hydrogenation process. Computational analysis reveals that H₂ dissociation is energetically favorable, with low activation barriers of approximately 7 kcal/mol for both Co- and Cu-MOF-808 catalysts.

In pathway A, the second step of CO₂ hydrogenation, involving the transformation of the formate intermediate into formic acid, is identified as the rate-determining step, with substantial energy barriers of approximately 60 kcal/mol for Co-MOF-808 and 50 kcal/mol for Cu-MOF-808. Notably, in pathway B, the formate intermediate assumes quasi-bidentate and bidentate-chelating configurations. The incorporation of a second H₂ molecule in these geometries markedly reduces the energy barriers for the second hydrogenation step, lowering them to nearly one-third of the values observed in pathway A.

Overall, the findings reveal that pathway B is both kinetically and thermodynamically more favorable than pathway A. Moreover, Cu²⁺-MOF-808 exhibits superior catalytic performance compared to Co²⁺-MOF-808, primarily attributed to Cu's

This material is reserved for educational use only, not allowed for commercial use.

Forbidden to modify the content, and cite the document when use.

enhanced capability to stabilize the transition state through its square planar geometry, facilitated by the Jahn-Teller effect. This stabilization effect is notably less pronounced in Co.

5.2 Suggestions

This study explores the reaction mechanism of CO₂ hydrogenation to formic acid, providing a foundation for future investigations into extending the hydrogenation process to synthesize other valuable products, such as formaldehyde and methanol, which have broad industrial applications. It is anticipated that the Co²⁺- and Cu²⁺-MOF-808 catalysts examined in this work will exhibit high catalytic efficiency. Future research could focus on substituting the metal centers with alternative elements and optimizing reaction conditions to further enhance catalytic performance.



References

- [1] R.M. Cuéllar-Franca, A. Azapagic, Carbon capture, storage and utilisation technologies: A critical analysis and comparison of their life cycle environmental impacts, *Journal of CO₂ Utilization* 9 (2015) 82–102.
<https://doi.org/10.1016/j.jcou.2014.12.001>.
- [2] B. Dziejarski, R. Krzyżyńska, K. Andersson, Current status of carbon capture, utilization, and storage technologies in the global economy: A survey of technical assessment, *Fuel* 342 (2023) 127776.
<https://doi.org/10.1016/j.fuel.2023.127776>.
- [3] W. Wang, S. Wang, X. Ma, J. Gong, Recent advances in catalytic hydrogenation of carbon dioxide, *Chem. Soc. Rev.* 40 (2011) 3703–3727.
<https://doi.org/10.1039/C1CS15008A>.
- [4] W. Li, H. Wang, X. Jiang, J. Zhu, Z. Liu, X. Guo, C. Song, A short review of recent advances in CO₂ hydrogenation to hydrocarbons over heterogeneous catalysts, *RSC Adv.* 8 (2018) 7651–7669. <https://doi.org/10.1039/C7RA13546G>.
- [5] R.-P. Ye, J. Ding, W. Gong, M.D. Argyle, Q. Zhong, Y. Wang, C.K. Russell, Z. Xu, A.G. Russell, Q. Li, M. Fan, Y.-G. Yao, CO₂ hydrogenation to high-value products via heterogeneous catalysis, *Nature Communications* 10 (2019) 5698.
<https://doi.org/10.1038/s41467-019-13638-9>.
- [6] Z. Sun, J. Dong, C. Chen, S. Zhang, Y. Zhu, Photocatalytic and electrocatalytic CO conversion: from fundamental principles to design of catalysts, *Journal of Chemical Technology & Biotechnology* 96 (2021) 1161–1175.
<https://doi.org/10.1002/jctb.6653>.
- [7] R.R. Ikreedeegh, M. Tahir, A critical review in recent developments of metal-organic-frameworks (MOFs) with band engineering alteration for photocatalytic CO₂ reduction to solar fuels, *Journal of CO₂ Utilization* 43 (2021) 101381.
<https://doi.org/10.1016/j.jcou.2020.101381>.
- [8] Wan-Hui Wang, Yuichiro Himeda, Recent Advances in Transition Metal-Catalysed Homogeneous Hydrogenation of Carbon Dioxide in Aqueous Media, in: Iyad Karamé (Ed.), *Hydrogenation*, IntechOpen, Rijeka, 2012: p. Ch. 10.
<https://doi.org/10.5772/48658>.

This material is reserved for educational use only, not allowed for commercial use.

Forbidden to modify the content, and cite the document when use.

- [9] M. Kondo, T. Yoshitomi, H. Matsuzaka, S. Kitagawa, K. Seki, Three-Dimensional Framework with Channeling Cavities for Small Molecules: $\{[M_2(4, 4'$ -bpy) $](NO_3)_4] \cdot xH_2O\}_n$ (M = Co, Ni, Zn), *Angewandte Chemie International Edition in English* 36 (1997) 1725–1727. <https://doi.org/10.1002/anie.199717251>.
- [10] M. Eddaoudi, J. Kim, N. Rosi, D. Vodak, J. Wachter, M. O’Keeffe, O.M. Yaghi, Systematic design of pore size and functionality in isorecticular MOFs and their application in methane storage, *Science* 295 (2002) 469–472. <https://doi.org/10.1126/science.1067208>.
- [11] P.Z. Moghadam, Y.G. Chung, R.Q. Snurr, Progress toward the computational discovery of new metal–organic framework adsorbents for energy applications, *Nature Energy* 9 (2024) 121–133. <https://doi.org/10.1038/s41560-023-01417-2>.
- [12] J. Lee, O.K. Farha, J. Roberts, K.A. Scheidt, S.T. Nguyen, J.T. Hupp, Metal–organic framework materials as catalysts, *Chem. Soc. Rev.* 38 (2009) 1450–1459. <https://doi.org/10.1039/B807080F>.
- [13] J.H. Cavka, S. Jakobsen, U. Olsbye, N. Guillou, C. Lamberti, S. Bordiga, K.P. Lillerud, A New Zirconium Inorganic Building Brick Forming Metal Organic Frameworks with Exceptional Stability, *J. Am. Chem. Soc.* 130 (2008) 13850–13851. <https://doi.org/10.1021/ja8057953>.
- [14] J.E. Mondloch, W. Bury, D. Fairen-Jimenez, S. Kwon, E.J. DeMarco, M.H. Weston, A.A. Sarjeant, S.T. Nguyen, P.C. Stair, R.Q. Snurr, O.K. Farha, J.T. Hupp, Vapor-Phase Metalation by Atomic Layer Deposition in a Metal–Organic Framework, *J. Am. Chem. Soc.* 135 (2013) 10294–10297. <https://doi.org/10.1021/ja4050828>.
- [15] H. Furukawa, F. Gándara, Y.-B. Zhang, J. Jiang, W.L. Queen, M.R. Hudson, O.M. Yaghi, Water Adsorption in Porous Metal–Organic Frameworks and Related Materials, *J. Am. Chem. Soc.* 136 (2014) 4369–4381. <https://doi.org/10.1021/ja500330a>.
- [16] D. Yang, B.C. Gates, Catalysis by Metal Organic Frameworks: Perspective and Suggestions for Future Research, *ACS Catal.* 9 (2019) 1779–1798. <https://doi.org/10.1021/acscatal.8b04515>.
- [17] Y. Shan, G. Zhang, Y. Shi, H. Pang, Synthesis and catalytic application of defective MOF materials, *Cell Reports Physical Science* 4 (2023) 101301. <https://doi.org/10.1016/j.xcrp.2023.101301>.

- [18] A.M. Abdel-Mageed, B. Rungtaweevoranit, M. Parlinska-Wojtan, X. Pei, O.M. Yaghi, R.J. Behm, Highly Active and Stable Single-Atom Cu Catalysts Supported by a Metal–Organic Framework, *J Am Chem Soc* 141 (2019) 5201–5210. <https://doi.org/10.1021/jacs.8b11386>.
- [19] B. Rungtaweevoranit, A.M. Abdel-Mageed, P. Khemthong, S. Eaimsumang, K. Chakarawet, T. Butburee, B. Kunkel, S. Wohlrab, K. Chainok, J. Phanthasri, S. Wannapaiboon, S. Youngjan, T. Seehamongkol, S. Impeng, K. Faungnawakij, Structural Evolution of Iron-Loaded Metal–Organic Framework Catalysts for Continuous Gas-Phase Oxidation of Methane to Methanol, *ACS Appl. Mater. Interfaces* 15 (2023) 26700–26709. <https://doi.org/10.1021/acsami.3c03310>.
- [20] K. Otake, S. Ahn, J. Knapp, J.T. Hupp, J.M. Notestein, O.K. Farha, Vapor-Phase Cyclohexene Epoxidation by Single-Ion Fe(III) Sites in Metal–Organic Frameworks, *Inorg. Chem.* 60 (2021) 2457–2463. <https://doi.org/10.1021/acs.inorgchem.0c03364>.
- [21] S. Impeng, E. Salaya-Gerónimo, B. Kunkel, S. Bartling, K. Faungnawakij, B. Rungtaweevoranit, A.M. Abdel-Mageed, Mechanism and selectivity of MOF-supported Cu single-atom catalysts for preferential CO oxidation, *J. Mater. Chem. A* 12 (2024) 3084–3095. <https://doi.org/10.1039/D3TA05047E>.
- [22] A.M. Abdel-Mageed, B. Rungtaweevoranit, S. Impeng, J. Bansmann, J. Rabeah, S. Chen, T. Häring, S. Namuangrak, K. Faungnawakij, A. Brückner, R.J. Behm, Unveiling the CO Oxidation Mechanism over a Molecularly Defined Copper Single-Atom Catalyst Supported on a Metal–Organic Framework, *Angewandte Chemie International Edition* 62 (2023) e202301920. <https://doi.org/10.1002/anie.202301920>.
- [23] J. Zhang, B. An, Z. Li, Y. Cao, Y. Dai, W. Wang, L. Zeng, W. Lin, C. Wang, Neighboring Zn–Zr Sites in a Metal–Organic Framework for CO₂ Hydrogenation, *J. Am. Chem. Soc.* 143 (2021) 8829–8837. <https://doi.org/10.1021/jacs.1c03283>.
- [24] J. Liu, W. Xue, W. Zhang, D. Mei, Theoretical Study on the Catalytic CO₂ Hydrogenation over the MOF-808-Encapsulated Single-Atom Metal Catalysts, *J. Phys. Chem. C* 127 (2023) 4051–4062. <https://doi.org/10.1021/acs.jpcc.2c08006>.
- [25] C. Song, A.F. Gaffney, K. Fujimoto, A.C.S.D. of P. Chemistry, A.C.S. Meeting, CO₂ Conversion and Utilization, American Chemical Society, Washington, DC, 2002.

- [26] V.G. Yadav, G.D. Yadav, S.C. Patankar, The production of fuels and chemicals in the new world: critical analysis of the choice between crude oil and biomass vis-à-vis sustainability and the environment, *Clean Technologies and Environmental Policy* 22 (2020) 1757–1774. <https://doi.org/10.1007/s10098-020-01945-5>.
- [27] I. Ahmed, S.H. Jhung, Composites of metal–organic frameworks: Preparation and application in adsorption, *Materials Today* 17 (2014) 136–146. <https://doi.org/10.1016/j.mattod.2014.03.002>.
- [28] Q. Wang, D. Astruc, State of the Art and Prospects in Metal–Organic Framework (MOF)-Based and MOF-Derived Nanocatalysis, *Chem. Rev.* 120 (2020) 1438–1511. <https://doi.org/10.1021/acs.chemrev.9b00223>.
- [29] G. Groenhof, Introduction to QM/MM simulations, *Methods in Molecular Biology* (Clifton, N.J.) 924 (2013) 43–66. https://doi.org/10.1007/978-1-62703-017-5_3.
- [30] J.G. Hill, Gaussian basis sets for molecular applications, *International Journal of Quantum Chemistry* 113 (2013) 21–34. <https://doi.org/10.1002/qua.24355>.
- [31] F. Jensen, *Introduction to Computational Chemistry*, 3rd ed., Wiley, New Jersey, 2017.
- [32] M.T. Lusk, A.E. Mattsson, High-performance computing for materials design to advance energy science, *MRS Bulletin* 36 (2011) 169–174. <https://doi.org/10.1557/mrs.2011.30>.
- [33] A. Coble, A. Smallbone, A. Bhave, S. Mosbach, M. Kraft, P. Niven, S. Amphlett, Implementing Detailed Chemistry and In-Cylinder Stratification into 0/1-D IC Engine Cycle Simulation Tools, *SAE Technical Papers* (2011). <https://doi.org/10.4271/2011-01-0849>.
- [34] M. Wolfsberg, W.A. Van Hook, P. Paneth, The Born–Oppenheimer Approximation: Potential Energy Surfaces, in: M. Wolfsberg, W.A. Hook, P. Paneth, L.P.N. Rebelo (Eds.), *Isotope Effects: In the Chemical, Geological, and Bio Sciences*, Springer Netherlands, Dordrecht, 2009: pp. 37–54. https://doi.org/10.1007/978-90-481-2265-3_2.
- [35] J.-L. Basdevant, Wave Function, Schrödinger Equation, in: J.-L. Basdevant (Ed.), *Lectures on Quantum Mechanics: With Problems, Exercises and Solutions*, Springer International Publishing, Cham, 2023: pp. 33–61. https://doi.org/10.1007/978-3-031-17635-7_3.

This material is reserved for educational use only, not allowed for commercial use.

Forbidden to modify the content, and cite the document when use.

- [36] S. Hotta, Schrödinger Equation and Its Application, in: S. Hotta (Ed.), *Mathematical Physical Chemistry: Practical and Intuitive Methodology*, Springer Nature Singapore, Singapore, 2023: pp. 3–30. https://doi.org/10.1007/978-981-99-2512-4_1.
- [37] M. Elstner, Q. Cui, M. Gruden, Density Functional Theory (DFT), in: M. Elstner, Q. Cui, M. Gruden (Eds.), *Introduction to Statistical Thermodynamics: A Molecular Perspective*, Springer International Publishing, Cham, 2024: pp. 515–533. https://doi.org/10.1007/978-3-031-54994-6_21.
- [38] J. Olsen, An Introduction and Overview of Basis Sets for Molecular and Solid-State Calculations, in: E. Perlt (Ed.), *Basis Sets in Computational Chemistry*, Springer International Publishing, Cham, 2021: pp. 1–16. https://doi.org/10.1007/978-3-030-67262-1_1.
- [39] Y. Zhao, D.G. Truhlar, The M06 suite of density functionals for main group thermochemistry, thermochemical kinetics, noncovalent interactions, excited states, and transition elements: two new functionals and systematic testing of four M06-class functionals and 12 other functionals, *Theoretical Chemistry Accounts* 120 (2008) 215–241. <https://doi.org/10.1007/s00214-007-0310-x>.
- [40] F. Weigend, R. Ahlrichs, Balanced basis sets of split valence, triple zeta valence and quadruple zeta valence quality for H to Rn: Design and assessment of accuracy, *Phys. Chem. Chem. Phys.* 7 (2005) 3297–3305. <https://doi.org/10.1039/B508541A>.
- [41] M. Dolg, U. Wedig, H. Stoll, H. Preuss, Energy-adjusted ab initio pseudopotentials for the first-row transition elements, *The Journal of Chemical Physics* 86 (1987) 866–872. <https://doi.org/10.1063/1.452288>.
- [42] A.E. Reed, L.A. Curtiss, F. Weinhold, Intermolecular interactions from a natural bond orbital, donor-acceptor viewpoint, *Chem. Rev.* 88 (1988) 899–926. <https://doi.org/10.1021/cr00088a005>.
- [43] S. Grimme, J. Antony, S. Ehrlich, H. Krieg, A consistent and accurate ab initio parametrization of density functional dispersion correction (DFT-D) for the 94 elements H-Pu, *The Journal of Chemical Physics* 132 (2010) 154104. <https://doi.org/10.1063/1.3382344>.
- [44] M.J. Frisch, G.W. Trucks, H.B. Schlegel, G.E. Scuseria, M.A. Robb, J.R. Cheeseman, G. Scalmani, V. Barone, G.A. Petersson, H. Nakatsuji, X. Li, M. Caricato, A.V.

This material is reserved for educational use only, not allowed for commercial use.

Forbidden to modify the content, and cite the document when use.

- Marenich, J. Bloino, B.G. Janesko, R. Gomperts, B. Mennucci, H.P. Hratchian, J.V. Ortiz, A.F. Izmaylov, J.L. Sonnenberg, D. Williams-Young, F. Ding, F. Lipparini, F. Egidi, J. Goings, B. Peng, A. Petrone, T. Henderson, D. Ranasinghe, V.G. Zakrzewski, J. Gao, N. Rega, G. Zheng, W. Liang, M. Hada, M. Ehara, K. Toyota, R. Fukuda, J. Hasegawa, M. Ishida, T. Nakajima, Y. Honda, O. Kitao, H. Nakai, T. Vreven, K. Throssell, J.A. Montgomery Jr., J.E. Peralta, F. Ogliaro, M.J. Bearpark, J.J. Heyd, E.N. Brothers, K.N. Kudin, V.N. Staroverov, T.A. Keith, R. Kobayashi, J. Normand, K. Raghavachari, A.P. Rendell, J.C. Burant, S.S. Iyengar, J. Tomasi, M. Cossi, J.M. Millam, M. Klene, C. Adamo, R. Cammi, J.W. Ochterski, R.L. Martin, K. Morokuma, O. Farkas, J.B. Foresman, D.J. Fox, Gaussian 16, Rev. C.02, Gaussian, Inc, Wallingford CT, (2019).
- [45] R. Holyst, M. Litniewski, D. Jakubczyk, A molecular dynamics test of the Hertz–Knudsen equation for evaporating liquids, *Soft Matter* 11 (2015) 7201–7206. <https://doi.org/10.1039/C5SM01508A>.
- [46] C.T. Campbell, Future Directions and Industrial Perspectives Micro- and macro-kinetics: Their relationship in heterogeneous catalysis, *Topics in Catalysis* 1 (1994) 353–366. <https://doi.org/10.1007/BF01492288>.
- [47] C.T. Campbell, Finding the Rate-Determining Step in a Mechanism: Comparing DeDonder Relations with the “Degree of Rate Control,” *Journal of Catalysis* 204 (2001) 520–524. <https://doi.org/10.1006/jcat.2001.3396>.
- [48] C. Stegelmann, A. Andreasen, C.T. Campbell, Degree of Rate Control: How Much the Energies of Intermediates and Transition States Control Rates, *J. Am. Chem. Soc.* 131 (2009) 8077–8082. <https://doi.org/10.1021/ja9000097>.
- [49] C.T. Campbell, Z. Mao, Analysis and prediction of reaction kinetics using the degree of rate control, *Journal of Catalysis* 404 (2021) 647–660. <https://doi.org/10.1016/j.jcat.2021.10.002>.
- [50] I.A.W. Filot, R.A. van Santen, E.J.M. Hensen, The Optimally Performing Fischer–Tropsch Catalyst, *Angewandte Chemie International Edition* 53 (2014) 12746–12750. <https://doi.org/10.1002/anie.201406521>.
- [51] G. Peng, S.J. Sibener, G.C. Schatz, S.T. Ceyer, M. Mavrikakis, CO₂ Hydrogenation to Formic Acid on Ni(111), *J. Phys. Chem. C* 116 (2012) 3001–3006. <https://doi.org/10.1021/jp210408x>.

- [52] T. Maihom, S. Wannakao, B. Boekfa, J. Limtrakul, Production of Formic Acid via Hydrogenation of CO₂ over a Copper-Alkoxide-Functionalized MOF: A Mechanistic Study, *J. Phys. Chem. C* 117 (2013) 17650–17658. <https://doi.org/10.1021/jp405178p>.
- [53] J. Sirijaraensre, J. Limtrakul, Hydrogenation of CO₂ to formic acid over a Cu-embedded graphene: A DFT study, *Applied Surface Science* 364 (2016) 241–248. <https://doi.org/10.1016/j.apsusc.2015.12.117>.
- [54] N. Yodsin, C. Rungrim, S. Tungkamani, V. Promarak, S. Namuangruk, S. Jungstittiwong, DFT Study of Catalytic CO₂ Hydrogenation over Pt-Decorated Carbon Nanocones: H₂ Dissociation Combined with the Spillover Mechanism, *J. Phys. Chem. C* 124 (2020) 1941–1949. <https://doi.org/10.1021/acs.jpcc.9b08776>.
- [55] G. Liu, P. Poths, X. Zhang, Z. Zhu, M. Marshall, M. Blankenhorn, A.N. Alexandrova, K.H. Bowen, CO₂ Hydrogenation to Formate and Formic Acid by Bimetallic Palladium–Copper Hydride Clusters, *J. Am. Chem. Soc.* 142 (2020) 7930–7936. <https://doi.org/10.1021/jacs.0c01855>.
- [56] W. Xue, X. Song, D. Mei, Theoretical Insights into CO Oxidation over MOF-808-Encapsulated Single-Atom Metal Catalysts, *J. Phys. Chem. C* 125 (2021) 17097–17108. <https://doi.org/10.1021/acs.jpcc.1c04906>.
- [57] Kittel, *Introduction to Solid State Physics*, 7th Ed, 2007.
- [58] T. Maihom, S. Wannakao, B. Boekfa, J. Limtrakul, Production of Formic Acid via Hydrogenation of CO₂ over a Copper-Alkoxide-Functionalized MOF: A Mechanistic Study, *J. Phys. Chem. C* 117 (2013) 17650–17658. <https://doi.org/10.1021/jp405178p>.
- [59] K. Nilwanna, J. Sittiwong, B. Boekfa, P. Treesukol, S. Boonya-udtayan, M. Probst, T. Maihom, J. Limtrakul, Aluminum-based metal-organic framework support metal(II)-hydride as catalyst for the hydrogenation of carbon dioxide to formic acid: A computational study, *Molecular Catalysis* 541 (2023) 113116. <https://doi.org/10.1016/j.mcat.2023.113116>.
- [60] Y. Chai, B. Qin, B. Li, W. Dai, G. Wu, N. Guan, L. Li, Zeolite-encaged mononuclear copper centers catalyze CO₂ selective hydrogenation to methanol, *National Science Review* 10 (2023) nwad043. <https://doi.org/10.1093/nsr/nwad043>.
- [61] N. Yodsin, C. Rungrim, S. Tungkamani, V. Promarak, S. Namuangruk, S. Jungstittiwong, DFT Study of Catalytic CO₂ Hydrogenation over Pt-Decorated

This material is reserved for educational use only, not allowed for commercial use.

Forbidden to modify the content, and cite the document when use.

- Carbon Nanocones: H₂ Dissociation Combined with the Spillover Mechanism, *J. Phys. Chem. C* 124 (2020) 1941–1949. <https://doi.org/10.1021/acs.jpcc.9b08776>.
- [62] Y. Injongkol, R. Intayot, N. Yodsin, A. Montoya, S. Jungsuttiwong, Mechanistic insight into catalytic carbon dioxide hydrogenation to formic acid over Pt-doped boron nitride nanosheets, *Molecular Catalysis* 510 (2021) 111675. <https://doi.org/10.1016/j.mcat.2021.111675>.
- [63] P. Poldorn, Y. Wongnongwa, T. Mudchimo, S. Jungsuttiwong, Theoretical insights into catalytic CO₂ hydrogenation over single-atom (Fe or Ni) incorporated nitrogen-doped graphene, *Journal of CO₂ Utilization* 48 (2021) 101532. <https://doi.org/10.1016/j.jcou.2021.101532>.
- [64] S. Ali, R. Iqbal, A. Khan, S.U. Rehman, M. Haneef, L. Yin, Stability and Catalytic Performance of Single-Atom Catalysts Supported on Doped and Defective Graphene for CO₂ Hydrogenation to Formic Acid: A First-Principles Study, *ACS Appl. Nano Mater.* 4 (2021) 6893–6902. <https://doi.org/10.1021/acsanm.1c00959>.
- [65] Y. Zhang, Y. Mo, Z. Cao, Rational Design of Main Group Metal-Embedded Nitrogen-Doped Carbon Materials as Frustrated Lewis Pair Catalysts for CO₂ Hydrogenation to Formic Acid, *ACS Appl. Mater. Interfaces* 14 (2022) 1002–1014. <https://doi.org/10.1021/acsami.1c20230>.
- [66] X. Liang, Q. Ke, X. Zhao, X. Chen, Graphene-Supported Tin Single-Atom Catalysts for CO₂ Hydrogenation to HCOOH: A Theoretical Investigation of Performance under Different N Coordination Numbers, *ACS Appl. Nano Mater.* 6 (2023) 4489–4498. <https://doi.org/10.1021/acsanm.2c05581>.
- [67] M. Creutzburg, K. Sellschopp, S. Tober, E. Grånäs, V. Vonk, W. Mayr-Schmölzer, S. Müller, H. Noei, G.B. Vonbun-Feldbauer, A. Stierle, Heterogeneous Adsorption and Local Ordering of Formate on a Magnetite Surface, *J. Phys. Chem. Lett.* 12 (2021) 3847–3852. <https://doi.org/10.1021/acs.jpcllett.1c00209>.



This material is reserved for educational use only, not allowed for commercial use.

Forbidden to modify the content, and cite the document when use.

Appendix A: Supporting information

Table S1. Electron configuration, charge, and spin density of selected atoms along the pathway A for CO₂ hydrogenation over Co²⁺-MOF-808.

System	Electron Configuration	Charge e	Spin density ($\rho\alpha - \rho\beta$)
Co ²⁺ - MOF- 808	Co = [core] 4s (0.42) 3d (7.37) 4p (0.03) 4d (0.01) = 7.83	1.16	2.49
	O = [core] 2s (1.85) 2p (5.11) = 6.96	-0.97	0.35
	μ 3-O = [core] 2s (1.77) 2p (5.30) = 7.07	-1.07	0.15
INT1	Co = [core] 4s (0.34) 3d (7.53) 4p (0.03) 4d (0.02) = 7.92	1.07	2.30
	O = [core] 2s (1.84) 2p (5.07) = 6.91	-0.92	0.50
	μ 3-O = [core] 2s (1.76) 2p (5.30) = 7.06	-1.06	0.19
	H1 = 1s (0.96) 2s (0.01) = 0.97	0.03	-0.01
	H2 = 1s (1.00) = 1.00	0.00	0.00
TS1	Co = [core] 4s (0.31) 3d (7.34) 4p (0.03) 4d (0.01) = 7.69	1.30	2.65
	O = [core] 2s (1.83) 2p (5.22) = 7.05	-1.06	0.19
	μ 3-O = [core] 2s (1.76) 2p (5.36) = 7.12	-1.13	0.06
	H1 = 1s (0.75) = 0.75	0.25	0.00
	H2 = 1s (1.22) = 1.22	-0.23	0.04
INT2	Co = [core] 4s (0.50) 3d (7.27) 4p (0.02) 4d (0.01) = 7.80	1.19	2.79
	O = [core] 2s (1.75) 2p (5.32) 3p (0.01) = 7.08	-1.08	0.05
	μ 3-O = [core] 2s (1.76) 2p (5.38) = 7.14	-1.14	0.06
	H1 = 1s (0.49) = 0.49	0.51	0.00
	H2 = 1s (1.47) = 1.47	-0.47	0.05
INT3	Co = [core] 4s (0.46) 3d (7.30) 4p (0.02) 4d (0.01) = 7.79	1.21	2.75
	O = [core] 2s (1.75) 2p (5.32) 3p (0.01) = 7.08	-1.08	0.06
	μ 3-O = [core] 2s (1.75) 2p (5.39) = 7.14	-1.15	0.07
	H1 = 1s (0.49) = 0.49	0.51	0.00
	H2 = 1s (1.48) = 1.48	-0.49	0.08
	C = [core] 2s (0.64) 2p (2.20) 3p (0.02) 3d (0.02) = 2.88	1.12	0.01
	O1 = [core] 2s (1.73) 2p (4.74) 3d (0.01) = 6.48	-0.49	0.00
	O2 = [core] 2s (1.72) 2p (4.86) 3p (0.01) 3d (0.01) = 6.60	-0.60	0.01

This material is reserved for educational use only, not allowed for commercial use.

Forbidden to modify the content, and cite the document when use.

Table S1. (Continued)

System	Electron Configuration	Charge e	Spin density ($\rho\alpha - \rho\beta$)
TS2	Co = [core] 4s (0.35) 3d (7.29) 4p (0.02) 4d (0.01) = 7.67	1.32	2.69
	O = [core] 2s (1.75) 2p (5.31) 3p (0.01) = 7.07	-1.08	0.06
	μ 3-O = [core] 2s (1.75) 2p (5.38) = 7.13	-1.14	0.07
	H1 = 1s (0.49) = 0.49	0.51	0.00
	H2 = 1s (1.36) = 1.36	-0.36	0.06
	C = [core] 2s (0.70) 2p (2.30) 3s (0.01) 3p (0.04) 3d (0.02) = 3.07	0.95	0.01
	O1 = [core] 2s (1.71) 2p (4.80) 3d (0.01) = 6.52	-0.53	0.01
	O2 = [core] 2s (1.73) 2p (4.93) 3d (0.01) = 6.67	-0.67	0.07
INT4	Co = [core] 4s (0.30) 3d (7.21) 4p (0.02) 4d (0.01) = 7.54	1.46	2.77
	O = [core] 2s (1.75) 2p (5.32) = 7.07	-1.08	0.06
	μ 3-O = [core] 2s (1.76) 2p (5.38) = 7.14	-1.15	0.05
	H1 = 1s (0.48) = 0.48	0.51	0.00
	H2 = 1s (0.88) = 0.88	0.12	0.00
	C = [core] 2s (0.86) 2p (2.39) 3s (0.01) 3p (0.03) 3d (0.01) = 3.3	0.70	0.00
	O1 = [core] 2s (1.74) 2p (5.03) 3d (0.01) = 6.78	-0.79	0.05
	O2 = [core] 2s (1.74) 2p (5.02) 3d (0.01) = 6.77	-0.77	0.04
TS3-A	Co = [core] 4s (0.31) 3d (7.29) 4p (0.02) 4d (0.01) = 7.63	1.36	2.64
	O = [core] 2s (1.83) 2p (5.27) = 7.10	-1.11	0.19
	μ 3-O = [core] 2s (1.75) 2p (5.36) = 7.11	-1.12	0.10
	H1 = 1s (0.44) = 0.44	0.55	0.00
	H2 = 1s (0.89) = 0.89	0.11	0.00
	C = [core] 2s (0.86) 2p (2.37) 3s (0.01) 3p (0.02) 3d (0.01) = 3.27	0.74	0.00
	O1 = [core] 2s (1.70) 2p (5.14) = 6.84	-0.86	0.03
	O2 = [core] 2s (1.72) 2p (4.84) 3d (0.01) = 6.57	-0.58	0.01

This material is reserved for educational use only, not allowed for commercial use.

Forbidden to modify the content, and cite the document when use.

Table S1. (Continued)

System	Electron Configuration	Charge $ e $	Spin density ($\rho\alpha - \rho\beta$)
PROD-A	Co = [core] 4s (0.33) 3d (7.34) 4p (0.02) 4d (0.01) = 7.7	1.29	2.56
	O = [core] 2s (1.85) 2p (5.21) = 7.06	-1.07	0.29
	μ 3-O = [core] 2s (1.76) 2p (5.33) = 7.09	-1.10	0.10
	H1 = 1s (0.49) = 0.49	0.50	0.00
	H2 = 1s (0.80) = 0.80	0.19	0.00
	C = [core] 2s (0.88) 2p (2.32) 3s (0.01) 3p (0.02) 3d (0.01) = 3.24	0.76	0.00
	O1 = [core]2s (1.69) 2p (4.95) 3d (0.01) = 6.65	-0.65	0.00
	O2 = [core]2s (1.72) 2p (4.98) 3p (0.01) 3d (0.01) = 6.72	-0.71	0.03

This material is reserved for educational use only, not allowed for commercial use.

Forbidden to modify the content, and cite the document when use.

Table S2. Electron configuration, charge, and spin density of selected atoms along the pathway B bidentate chelating for CO₂ hydrogenation over Co²⁺-MOF-808.

System	Electron Configuration	Charge e	Spin density ($\rho\alpha - \rho\beta$)
INT5	Co = [core] 4s (0.29) 3d (7.22) 4p (0.02) 4d (0.01) 5p (0.01) = 7.55	1.45	2.74
	O = [core]2s (1.75) 2p (5.32) = 7.07	-1.08	0.06
	μ 3-O = [core] 2s (1.75) 2p (5.39) = 7.14	-1.15	0.05
	H1 = 1s (0.48) = 0.48	0.51	0.00
	H2 = 1s (0.88) = 0.88	0.12	0.00
	C = [core]2s (0.86) 2p (2.39) 3s (0.01) 3p (0.03) 3d (0.01) = 3.30	0.70	0.00
	O1 = [core]2s (1.74) 2p (5.04) 3d (0.01) = 6.79	-0.79	0.05
	O2 = [core]2s (1.74) 2p (5.01) 3d (0.01) = 6.76	-0.77	0.05
	H3 = 1s (0.97) = 0.97	0.02	0.01
	H4 = 1s (0.99) = 0.99	0.00	0.01
TS3-B	Co = [core]4s (0.34) 3d (7.27) 4p (0.02) 4d (0.01) = 7.64	1.34	2.69
	O = [core]2s (1.76) 2p (5.31) 3p (0.01) = 7.08	-1.07	0.06
	μ 3-O = [core]2s (1.75) 2p (5.39) = 7.14	-1.14	0.07
	H1 = 1s (0.49) = 0.49	0.51	0.00
	H2 = 1s (0.86) = 0.86	0.14	0.01
	C = [core] 2s (0.85) 2p (2.36) 3p (0.02) 3d (0.01) = 3.24	0.75	0.00
	O1 = [core] 2s (1.72) 2p (5.02) 3p (0.01) 3d (0.01) = 6.76	-0.76	0.04
	O2 = [core] 2s (1.70) 2p (4.99) 3d (0.01) = 6.70	-0.70	0.02
	H3 = 1s (0.60) = 0.60	0.39	0.02
	H4 = 1s (1.42) = 1.42	-0.43	0.06

Table S2. (Continued)

System	Electron Configuration	Charge e	Spin density ($\rho\alpha - \rho\beta$)
PROD-B	Co = [core] 4s (0.38) 3d (7.28) 4p (0.02) 4d (0.01) = 7.69	1.29	2.72
	O = [core] 2s (1.75) 2p (5.31) 3p (0.01) = 7.07	-1.07	0.06
	μ^3 -O = [core] 2s (1.75) 2p (5.39) = 7.14	-1.15	0.07
	H1 = 1s (0.49) = 0.49	0.51	0.00
	H2 = 1s (0.85) = 0.85	0.14	0.01
	C = [core] 2s (0.86) 2p (2.34) 3p (0.02) 3d (0.01) = 3.23	0.76	0.00
	O1 = [core] 2s (1.71) 2p (4.97) 3p (0.01) 3d (0.01) = 6.70	-0.70	0.04
	O2 = [core] 2s (1.69) 2p (5.01) 3d (0.01) = 6.71	-0.70	0.01
	H3 = 1s (0.51) = 0.51	0.49	0.01
	H4 = 1s (1.52) = 1.52	-0.52	0.07

This material is reserved for educational use only, not allowed for commercial use.

Forbidden to modify the content, and cite the document when use.

Table S3. Electron configuration, charge, and spin density of selected atoms along the pathway B quasi-bidentate for CO₂ hydrogenation over Co²⁺-MOF-808.

System	Electron Configuration	Charge e	Spin density ($\rho\alpha - \rho\beta$)
INT4'	Co = [core] 4s (0.27) 3d (7.24) 4p (0.02) 4d (0.01) = 7.54	1.45	2.74
	O = [core] 2s (1.76) 2p (5.31) 3p (0.01) = 7.08	-1.08	0.07
	μ 3-O = [core] 2s (1.75) 2p (5.38) = 7.13	-1.14	0.10
	H1 = 1s (0.49) = 0.49	0.13	0.00
	H2 = 1s (0.87) = 0.87	0.51	0.00
	C = [core] 2s (0.85) 2p (2.34) 3s (0.01) 3p (0.02) 3d (0.01) = 3.23	0.76	0.00
	O1 = [core] 2s (1.68) 2p (5.05) = 6.73	-0.74	0.01
	O2 = [core] 2s (1.73) 2p (5.04) 3p (0.01) 3d (0.01) = 6.76	-0.79	0.04
INT5'	Co = [core] 4s (0.27) 3d (7.25) 4p (0.02) 4d (0.01) 5p (0.01) = 7.56	1.44	2.71
	O = [core] 2s (1.76) 2p (5.31) 3p (0.01) = 7.08	-1.08	0.07
	μ 3-O = [core] 2s (1.75) 2p (5.38) = 7.13	-1.14	0.10
	H1 = 1s (0.49) = 0.49	0.51	0.00
	H2 = 1s (0.87) = 0.87	0.13	0.00
	C = [core] 2s (0.85) 2p (2.34) 3s (0.01) 3p (0.02) 3d (0.01) = 3.23	0.77	0.00
	O1 = [core] 2s (1.68) 2p (5.04) = 6.72	-0.73	0.01
	O2 = [core] 2s (1.73) 2p (5.06) 3p (0.01) 3d (0.01) = 6.81	-0.80	0.05
	H3 = 1s (0.96) = 0.96	0.03	0.01
H4 = 1s (1.00) = 1.00	0.00	0.01	

Table S3. (Continued)

System	Electron Configuration	Charge e	Spin density ($\rho\alpha - \rho\beta$)
TS3-B'	Co = [core] 4s (0.32) 3d (7.29) 4p (0.02) 4d (0.01) = 7.64	1.34	2.69
	O = [core] 2s (1.76) 2p (5.30) 3p (0.01) = 7.07	-1.07	0.07
	μ 3-O = [core] 2s (1.75) 2p (5.38) = 7.13	-1.14	0.09
	H1 = 1s (0.49) = 0.49	0.50	0.00
	H2 = 1s (0.85) = 0.85	0.15	0.01
	C = [core] 2s (0.85) 2p (2.34) 3s (0.01) 3p (0.02) 3d (0.01) = 3.23	0.76	0.00
	O1 = [core] 2s (1.70) 2p (5.05) 3p (0.01) 3d (0.01) = 6.77	-0.76	0.05
	O2 = [core] 2s (1.70) 2p (4.97) 3d (0.01) = 6.68	-0.68	0.01
	H3 = 1s (0.66) = 0.66	0.33	0.02
H4 = 1s (1.36) = 1.36	-0.37	0.04	

This material is reserved for educational use only, not allowed for commercial use.

Forbidden to modify the content, and cite the document when use.

Table S4. Electron configuration, charge, and spin density of selected atoms along the pathway A for CO₂ hydrogenation over Cu²⁺-MOF-808.

System	Electron Configuration	Charge e	Spin density ($\rho\alpha - \rho\beta$)
Cu ²⁺ - MOF- 808	Cu = [core] 4s (0.38) 3d (9.47) 4p (0.03) = 9.88	1.11	0.43
	O = [core] 2s (1.86) 2p (5.06) = 6.92	-0.93	0.42
	μ 3-O = [core] 2s (1.77) 2p (5.29) = 7.06	-1.06	0.16
INT1	Cu = [core] 4s (0.36) 3d (9.53) 4p (0.03) 5s (0.01) = 9.93	1.06	0.32
	O = [core] 2s (1.86) 2p (5.00) = 6.86	-0.87	0.55
	μ 3-O = [core] 2s (1.76) 2p (5.32) = 7.08	-1.08	0.13
	H1 = 1s (0.94) = 0.94	0.05	-0.01
	H2 = 1s (1.00) = 1.00	-0.01	0.03
TS1	Cu = [core] 4s (0.38) 3d (9.51) 4p (0.03) = 9.92	1.07	0.42
	O79 = [core] 2s (1.85) 2p (5.04) = 6.89	-0.89	0.48
	μ 3-O = [core] 2s (1.76) 2p (5.35) = 7.11	-1.11	0.06
	H1 = 1s (0.77) = 0.77	0.22	-0.01
	H2 = 1s (1.16) = 1.16	-0.17	0.06
INT2	Cu = [core] 4s (0.55) 3d (9.42) 4p (0.03) = 10.0	1.00	0.60
	O = [core] 2s (1.76) 2p (5.32) 3p (0.01) = 7.09	-1.09	0.02
	μ 3-O = [core] 2s (1.76) 2p (5.31) = 7.07	-1.08	0.19
	H1 = 1s (0.49) = 0.49	0.51	0.00
	H2 = 1s (1.35) = 1.35	-0.36	0.17
INT3	Cu = [core] 4s (0.51) 3d (9.42) 4p (0.02) 4d (0.01) = 9.96	1.04	0.61
	O = [core] 2s (1.76) 2p (5.32) 3p (0.01) = 7.09	-1.09	0.03
	μ 3-O = [core] 2s (1.76) 2p (5.33) = 7.09	-1.09	0.17
	H1 = 1s (0.49) = 0.49	0.51	0.00
	H2 = 1s (1.37) = 1.37	-0.37	0.18
	C = [core] 2s (0.65) 2p (2.21) 3p (0.02) 3d (0.02) = 2.90	1.10	0.00
	O1 = [core] 2s (1.73) 2p (4.76) 3d (0.01) = 6.50	-0.51	0.00
	O2 = [core] 2s (1.72) 2p (4.84) 3d (0.01) = 6.57	-0.58	0.00

This material is reserved for educational use only, not allowed for commercial use.

Forbidden to modify the content, and cite the document when use.

Table S4. (Continued)

System	Electron Configuration	Charge e	Spin density ($\rho\alpha - \rho\beta$)
TS2	Cu = [core] 4s (0.39) 3d (9.41) 4p (0.02) 4d (0.01) = 9.83	1.17	0.54
	O = [core] 2s (1.76) 2p (5.31) = 7.07	-1.07	0.05
	μ 3-O = [core] 2s (1.76) 2p (5.34) = 7.10	-1.10	0.14
	H1 = 1s (0.49) = 0.49	0.51	0.00
	H2 = 1s (1.29) = 1.29	-0.29	0.15
	C = [core] 2s (0.69) 2p (2.29) 3s (0.01) 3p (0.04) 3d (0.02) = 3.05	0.95	0.00
	O1 = [core] 2s (1.72) 2p (4.79) 3d (0.01) = 6.52	-0.52	0.02
	O2 = [core] 2s (1.73) 2p (4.90) 3d (0.01) = 6.64	-0.64	0.10
INT4	Cu = [core] 4s (0.37) 3d (9.30) 4p (0.02) = 9.69	1.31	0.63
	O = [core] 2s (1.76) 2p (5.28) = 7.04	-1.05	0.09
	μ 3-O = [core] 2s (1.76) 2p (5.35) = 7.11	-1.11	0.11
	H1 = 1s (0.49) = 0.49	0.51	0.00
	H2 = 1s (0.87) = 0.87	0.12	0.00
	C = [core] 2s (0.87) 2p (2.38) 3s (0.01) 3p (0.03) 3d (0.01) = 3.30	0.71	-0.01
	O1 = [core] 2s (1.75) 2p (4.99) 3d (0.01) = 6.75	-0.75	0.09
	O2 = [core] 2s (1.74) 2p (4.97) 3d (0.01) = 6.27	-0.73	0.08

Table S3. (Continued)

System	Electron Configuration	Charge e	Spin density ($\rho\alpha - \rho\beta$)
TS3-A	Cu = [core] 4s (0.34) 3d (9.41) 4p (0.02) 4d (0.01) = 9.78	1.21	0.49
	O = [core] 2s (1.84) 2p (5.19) = 7.03	-1.03	0.33
	μ 3-O = [core]2s (1.75) 2p (5.33) = 7.08	-1.09	0.14
	H1 = 1s (0.44) = 0.44	0.56	0.00
	H2 = 1s (0.89) = 0.89	0.11	0.00
	C = [core] 2s (0.86) 2p (2.37) 3s (0.01) 3p (0.02) 3d (0.01) = 3.27	0.73	0.00
	O1 = [core] 2s (1.71) 2p (5.13) = 6.84	-0.85	0.02
	O2 = [core] 2s (1.72) 2p (4.83) 3d (0.01) = 6.56	-0.57	0.01
PROD-A	Cu = [core] 4s (0.38) 3d (9.42) 4p (0.02) 4d (0.01) = 9.83	1.16	0.47
	O = [core] 2s (1.86) 2p (5.13) = 6.99	-0.99	0.41
	μ 3-O = [core] 2s (1.76) 2p (5.32) = 7.08	-1.09	0.11
	H1 = 1s (0.49) = 0.49	0.50	0.00
	H2 = 1s (0.79) = 0.79	0.20	0.00
	C = [core] 2s (0.89) 2p (2.31) 3s (0.01) 3p (0.02) 3d (0.01) = 3.24	0.76	0.00
	O1 = [core] 2s (1.69) 2p (4.95) 3d (0.01) = 6.65	-0.65	0.00
	O2 = [core] 2s (1.72) 2p (4.98) 3p (0.01) 3d (0.01) = 6.72	-0.72	0.03

Table S5. Electron configuration, charge, and spin density of selected atoms along the pathway B bidentate chelating for CO₂ hydrogenation over Cu²⁺-MOF-808.

System	Electron Configuration	Charge e	Spin density ($\rho\alpha - \rho\beta$)
INT5	Cu = [core] 4s (0.35) 3d (9.30) 4p (0.02) 4d (0.01) = 9.68	1.32	0.64
	O = [core] 2s (1.76) 2p (5.29) = 7.05	-1.05	0.09
	μ 3-O = [core] 2s (1.76) 2p (5.36) = 7.12	-1.12	0.11
	H1 = 1s (0.49) = 0.49	0.51	0.00
	H2 = 1s (0.87) = 0.87	0.12	0.00
	C = [core] 2s (0.87) 2p (2.38) 3p (0.03) 3d (0.01) = 3.29	0.71	-0.01
	O1 = [core] 2s (1.74) 2p (4.98) 3d (0.01) = 6.73	-0.73	0.08
	O2 = [core] 2s (1.74) 2p (5.00) 3d (0.01) = 6.75	-0.76	0.09
	H3 = 1s (1.00) = 1.00	0.00	0.00
	H4 = 1s (0.99) = 0.99	0.00	0.00
TS3-B	Cu = [core]4s (0.37) 3d (9.37) 4p (0.02) 4d (0.01) = 9.77	1.22	0.56
	O79 = [core] 2s (1.76) 2p (5.27) = 7.03	-1.04	0.11
	μ 3-O = [core] 2s (1.76) 2p (5.36) = 7.12	-1.12	0.07
	H1 = 1s (0.49) = 0.49	0.51	0.00
	H2 = 1s (0.86) = 0.86	0.14	0.02
	C = [core] 2s (0.85) 2p (2.37) 3p (0.02) 3d (0.01) = 3.25	0.74	-0.01
	O1 = [core] 2s (1.72) 2p (5.02) 3p (0.01) 3d (0.01) = 6.76	-0.76	0.08
	O2 = [core] 2s (1.71) 2p (4.95) 3d (0.01) = 6.67	-0.67	0.05
	H3 = 1s (0.68) = 0.68	0.31	0.02
	H4 = 1s (1.29) = 1.29	-0.29	0.10

Table S5. (Continued)

System	Electron Configuration	Charge e	Spin density ($\rho\alpha - \rho\beta$)
PROD-B	Cu = [core]4s (0.41) 3d (9.40) 4p (0.02) 4d (0.01) = 9.84	1.16	0.56
	O = [core]2s (1.76) 2p (5.30) = 7.06	-1.07	0.05
	μ 3-O = [core]2s (1.76) 2p (5.35) = 7.11	-1.11	0.12
	H1 = 1s (0.49) = 0.49	0.51	0.00
	H2 = 1s (0.86) = 0.86	0.14	0.01
	C = [core] 2s (0.85) 2p (2.35) 3p (0.02) 3d (0.01) = 3.23	0.76	-0.01
	O1 = [core] 2s (1.72) 2p (4.95) 3p (0.01) 3d (0.01) = 6.69	-0.69	0.06
	O2 = [core] 2s (1.69) 2p (5.00) 3d (0.01) = 6.70	-0.69	0.01
	H3 = 1s (0.51) = 0.51	0.49	0.01
	H4 = 1s (1.44) = 1.44	-0.45	0.18

This material is reserved for educational use only, not allowed for commercial use.

Forbidden to modify the content, and cite the document when use.

Table S6. Electron configuration, charge, and spin density of selected atoms along the pathway B quasi-bidentate for CO₂ hydrogenation over Cu²⁺-MOF-808.

System	Electron Configuration	Charge e	Spin density ($\rho\alpha - \rho\beta$)
INT4'	Cu = [core] 4s (0.34) 3d (9.32) 4p (0.02) = 9.68	1.31	0.64
	O = [core] 2s (1.77) 2p (5.23) = 7.00	-1.01	0.17
	μ 3-O = [core] 2s (1.76) 2p (5.33) = 7.09	-1.09	0.14
	H1 = 1s (0.49) = 0.49	0.50	0.00
	H2 = 1s (0.87) = 0.87	0.13	0.00
	C = [core] 2s (0.85) 2p (2.35) 3s (0.01) 3p (0.02) 3d (0.01) = 3.24	0.75	0.00
	O1 = [core] 2s (1.68) 2p (5.04) = 6.72	-0.73	0.01
	O2 = [core] 2s (1.74) 2p (5.02) 3d (0.01) = 6.77	-0.77	0.04
INT5'	Cu = [core] 4s (0.31) 3d (9.33) 4p (0.02) = 9.66	1.32	0.62
	O = [core] 2s (1.77) 2p (5.24) = 7.01	-1.02	0.15
	μ 3-O = [core] 2s (1.76) 2p (5.34) = 7.10	-1.10	0.15
	H1 = 1s (0.49) = 0.49	0.50	0.00
	H2 = 1s (0.87) = 0.87	0.13	0.00
	C = [core] 2s (0.85) 2p (2.36) 3p (0.02) 3d (0.01) = 3.24	0.75	0.00
	O1 = [core] 2s (1.68) 2p (5.04) = 6.72	-0.73	0.01
	O2 = [core] 2s (1.73) 2p (5.03) 3d (0.01) = 6.77	-0.77	0.05
	H3 = 1s (0.97) = 0.97	0.03	0.01
H4 = 1s (1.00) = 1.00	-0.01	0.00	

This material is reserved for educational use only, not allowed for commercial use.

Forbidden to modify the content, and cite the document when use.

Table S6. (Continued)

System	Electron Configuration	Charge e	Spin density ($\rho\alpha - \rho\beta$)
TS3-B'	Cu = [core] 4s (0.35) 3d (9.36) 4p (0.03) 4d (0.01) = 9.75	1.25	0.62
	O = [core] 2s (1.77) 2p (5.26) = 7.03	-1.04	0.11
	μ 3-O = [core] 2s (1.75) 2p (5.34) = 7.09	-1.10	0.13
	H1 = 1s (0.50) = 0.50	0.50	0.00
	H2 = 1s (0.86) = 0.86	0.14	0.01
	C = [core] 2s (0.85) 2p (2.35) 3s (0.01) 3p (0.02) 3d (0.01) = 3.24	0.76	0.00
	O1 = [core] 2s (1.68) 2p (5.07) 3p (0.01) = 6.76	-0.76	0.03
	O2 = [core] 2s (1.71) 2p (4.94) 3d (0.01) = 6.66	-0.66	0.03
	H3 = 1s (0.73) = 0.73	0.26	0.01
H4 = 1s (1.24) = 1.24	-0.25	0.05	

This material is reserved for educational use only, not allowed for commercial use.

Forbidden to modify the content, and cite the document when use.

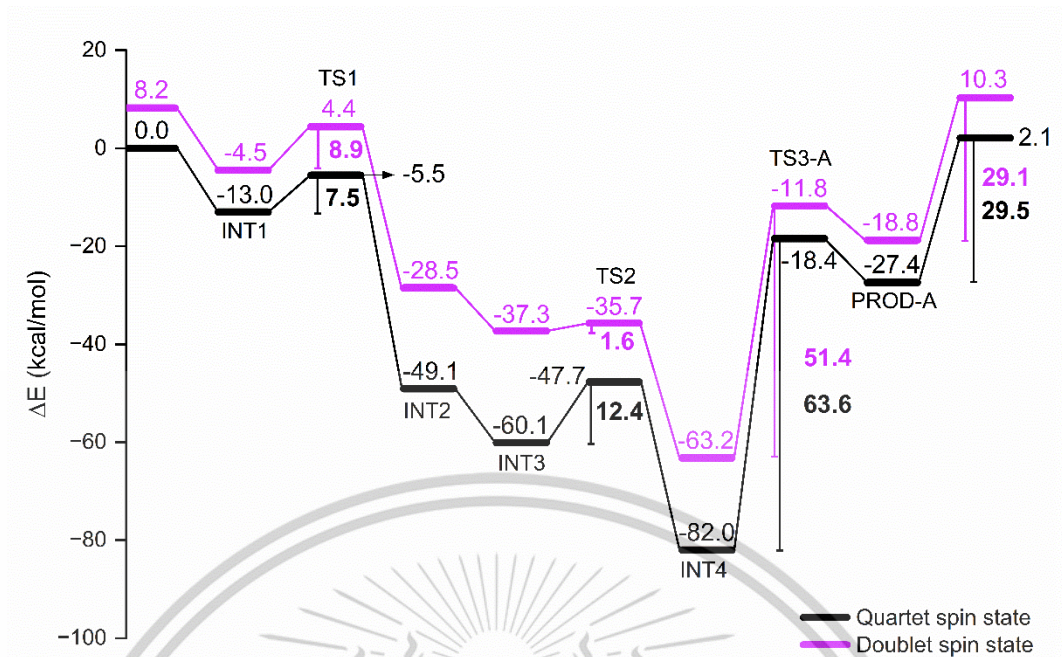


Figure S1. Energy profile for CO₂ hydrogenation over Co²⁺-MOF-808 on doublet and quartet spin states in pathway A, calculated at uM06-L/def2-SVP level of theory.

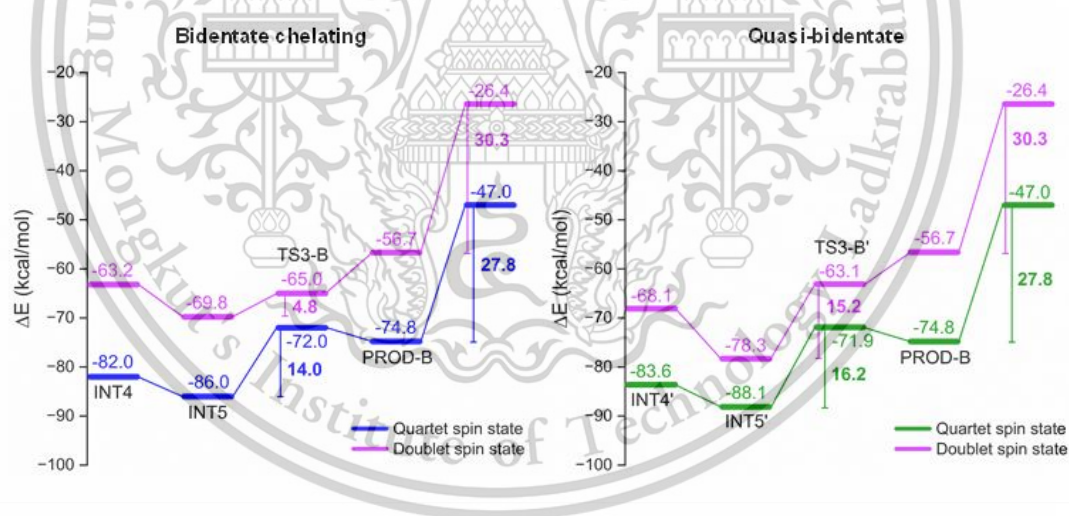


Figure S2. Energy profile for CO₂ hydrogenation over Co²⁺-MOF-808 on doublet and quartet spin states in pathway B, calculated at uM06-L/def2-SVP level of theory.

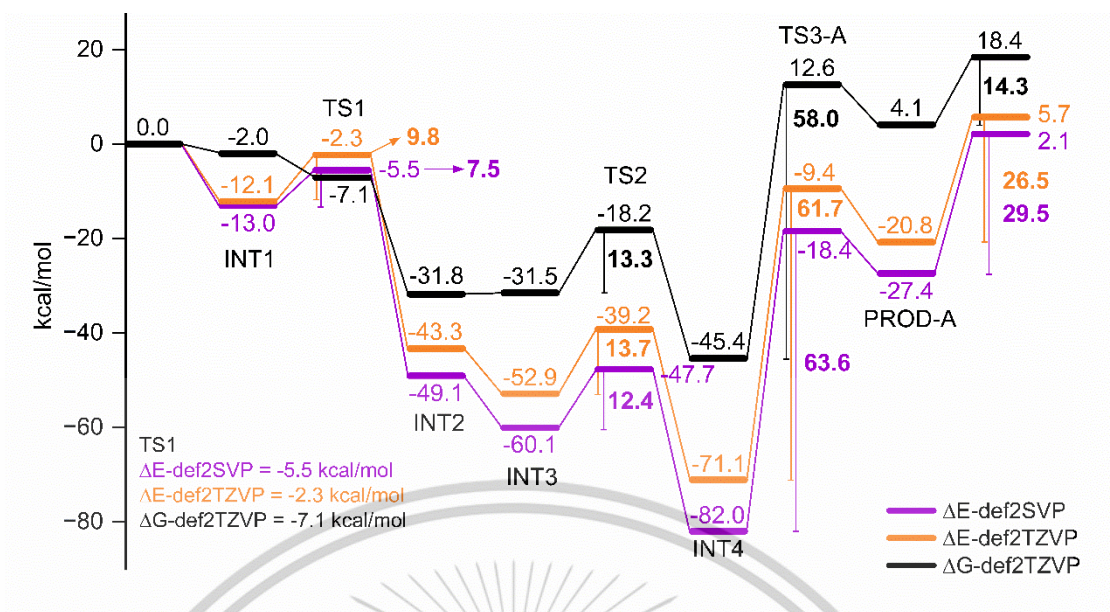


Figure S3. ΔE at def2-SVP and, ΔE and ΔG at def2-TZVP for CO₂ hydrogenation to formic acid over Co²⁺-MOF-808 (quartet spin state) in pathway A.

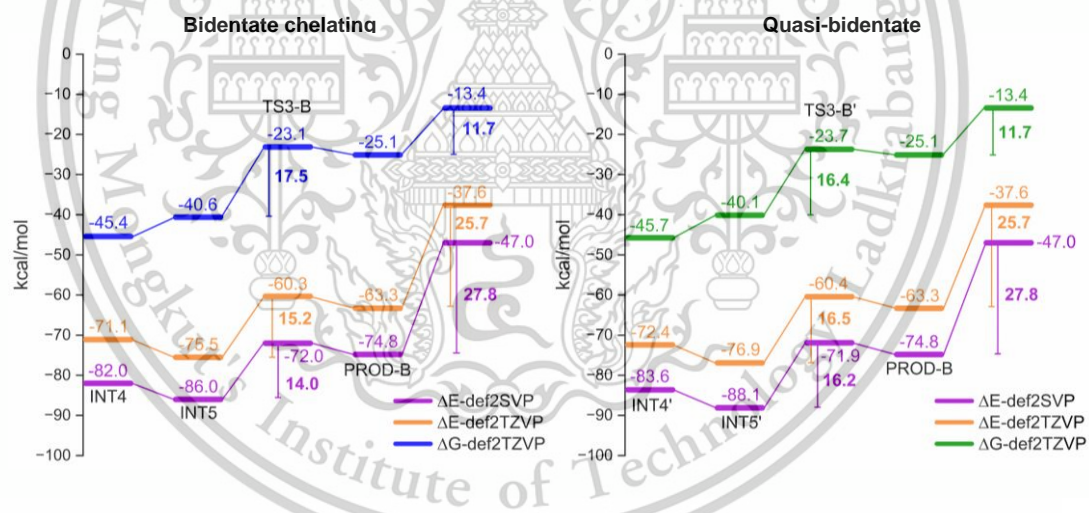


Figure S4. ΔE at def2-SVP and, ΔE and ΔG at def2-TZVP for CO₂ hydrogenation to formic acid over Co²⁺-MOF-808 (quartet spin state) in pathway B.

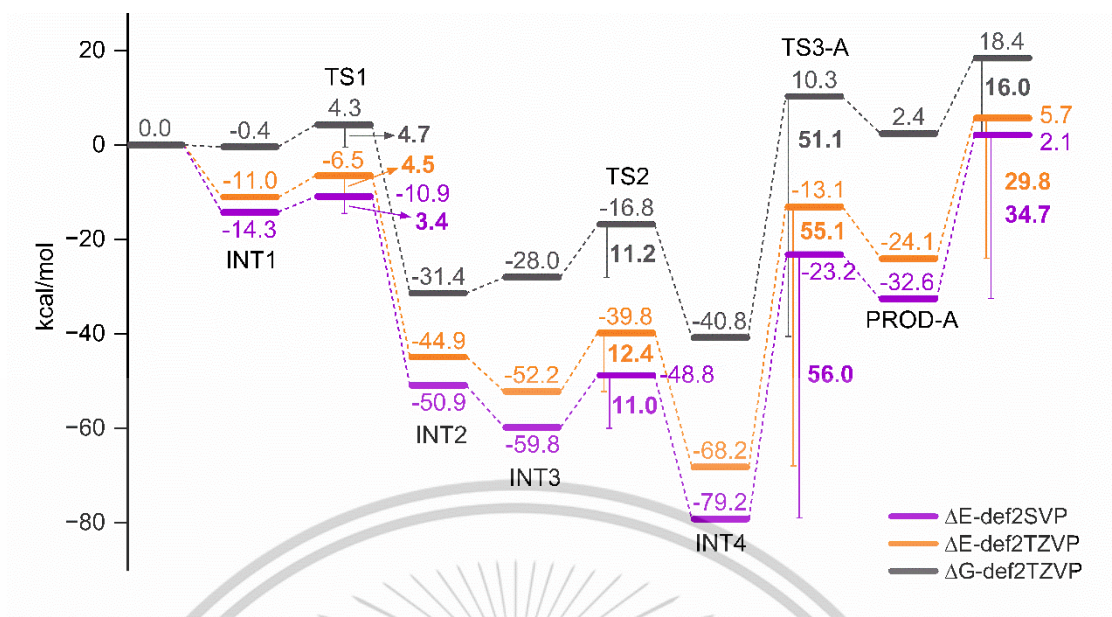


Figure S5. ΔE at def2-SVP and, ΔE and ΔG at def2-TZVP for CO₂ hydrogenation to formic acid over Cu²⁺-MOF-808 (doublet spin state) in pathway A.

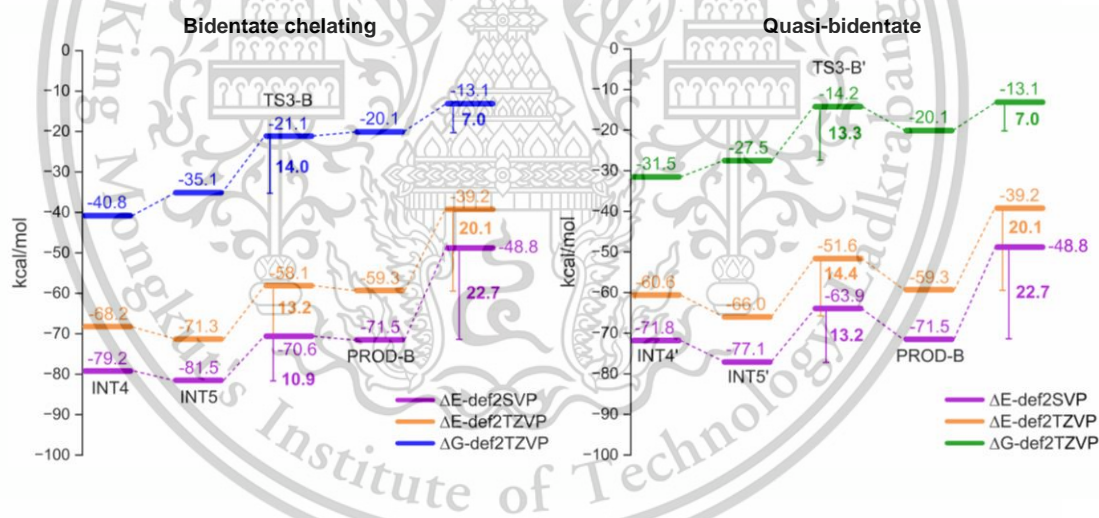


Figure S6. ΔE at def2-SVP and, ΔE and ΔG at def2-TZVP for CO₂ hydrogenation to formic acid over Cu²⁺-MOF-808 (doublet spin state) in pathway B.

Table S7. Summary of elementary reaction steps and activation energies from DFT calculations used for the MKM. E_{ads} represents the adsorption energy, while $E_{\text{a-f}}$ and $E_{\text{a-b}}$ denote the activation energies for the forward and backward reactions, respectively. The symbols * and # represent Co/Cu and O sites on Co^{2+} - and Cu^{2+} -MOF-808.

Elementary reaction step	Co^{2+} -MOF-808		Cu^{2+} -MOF-808	
	E_{ads} (J/mol)		E_{ads} (J/mol)	
<i>Adsorption/desorption reaction</i>				
R0: $[\text{H}_2] + [*] \leftrightarrow [\text{H}_2^*]$	50,626		46,024	
R1: $[\text{CO}_2] + [\text{H}_2^*] \leftrightarrow [\text{CO}_2\text{-H}^*]$	40,166		30,543	
R2: $[\text{H}_2] + [\text{HCOO}^*] \leftrightarrow [\text{H}_2\text{-HCOO}^*]$	18,410		12,970	
R3: $[\text{HCOOH}] + [\text{H}^*] \leftrightarrow [\text{H-HCOOH}^*]$	107,529		84,098	
R4: $[\text{HCOOH}] + [*] \leftrightarrow [\text{HCOOH}^*]$	110,876		124,683	
R5: $[\text{H}_2] + [\text{HCOOz}^*] \leftrightarrow [\text{H}_2\text{-HCOOz}^*]$	18,828		22,594	
Elementary reaction step	Co^{2+} -MOF-808		Cu^{2+} -MOF-808	
	$E_{\text{a-f}}$ (J/mol)	$E_{\text{a-b}}$ (J/mol)	$E_{\text{a-f}}$ (J/mol)	$E_{\text{a-b}}$ (J/mol)
<i>Surface reaction</i>				
R6: $[\text{H}_2^*] + [\text{H}^\#] \leftrightarrow [\text{H}^*] + [\text{H}^\#]$	41,300	171,544	18,828	160,665
R7: $[\text{CO}_2\text{-H}^*] \leftrightarrow [\text{HCOO}^*]$	57,321	133,469	51,882	118,825
R8: $[\text{HCOO}^*] + [\text{H}^\#] \leftrightarrow [\text{HCOOH}^*] + [\text{H}^\#]$	258,153	47,698	230,538	46,024
R9: $[\text{H}_2\text{-HCOO}^*] \leftrightarrow [\text{H-HCOOH}^*]$	63,597	12,552	55,229	5,021
R10: $[\text{CO}_2\text{-H}^*] \leftrightarrow [\text{HCOOz}^*]$	57,321	138,909	51,882	87,027
R11: $[\text{H}_2\text{-HCOOz}^*] \leftrightarrow [\text{H-HCOOH}^*]$	60,250	32,217	69,036	12,134

Please note that $[\text{HCOOz}^*]$ refers to the INT4' in the quasi-bidentate pathway of pathway B, which we referred to as pathway B'. All the reported energies in the Table S7 are ΔE at the M06L/def2-TZVP/SDD level of theory.

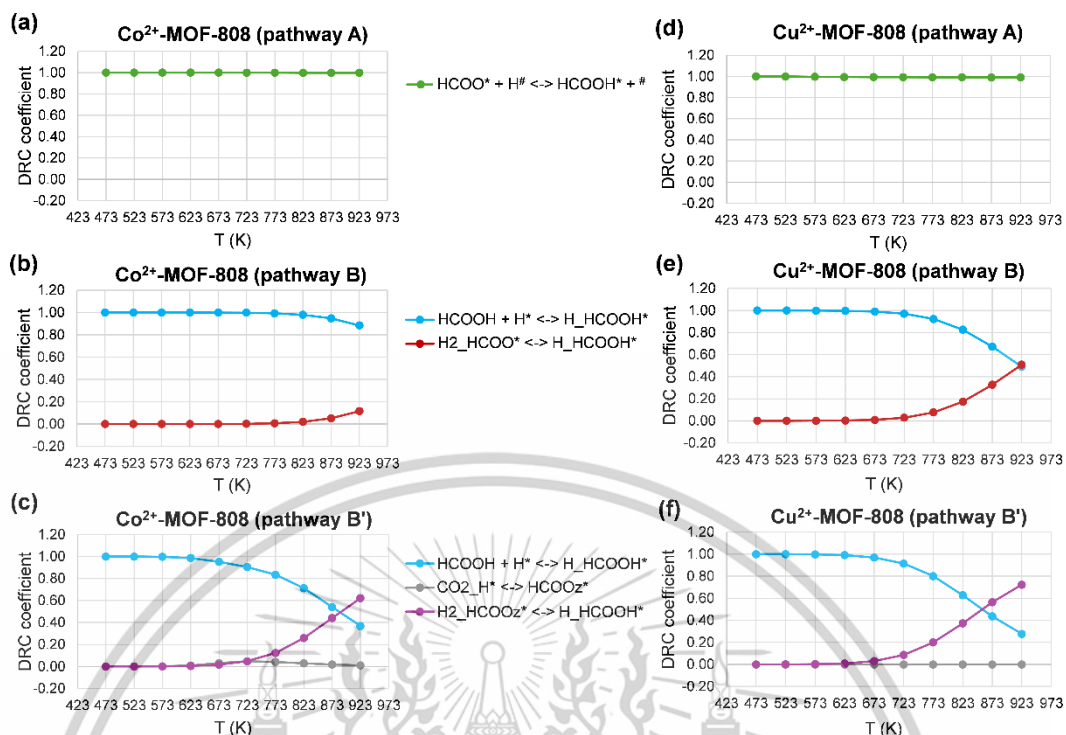


Figure S7. Degree of rate control (DRC) as a function of temperature for Co²⁺-MOF-808: (a) pathway A, (b) pathway B, (c) pathway B'; and for Cu²⁺-MOF-808: (d) pathway A, (e) pathway B, (f) pathway B'. Note that elementary reaction steps with zero DRC coefficient are not shown.

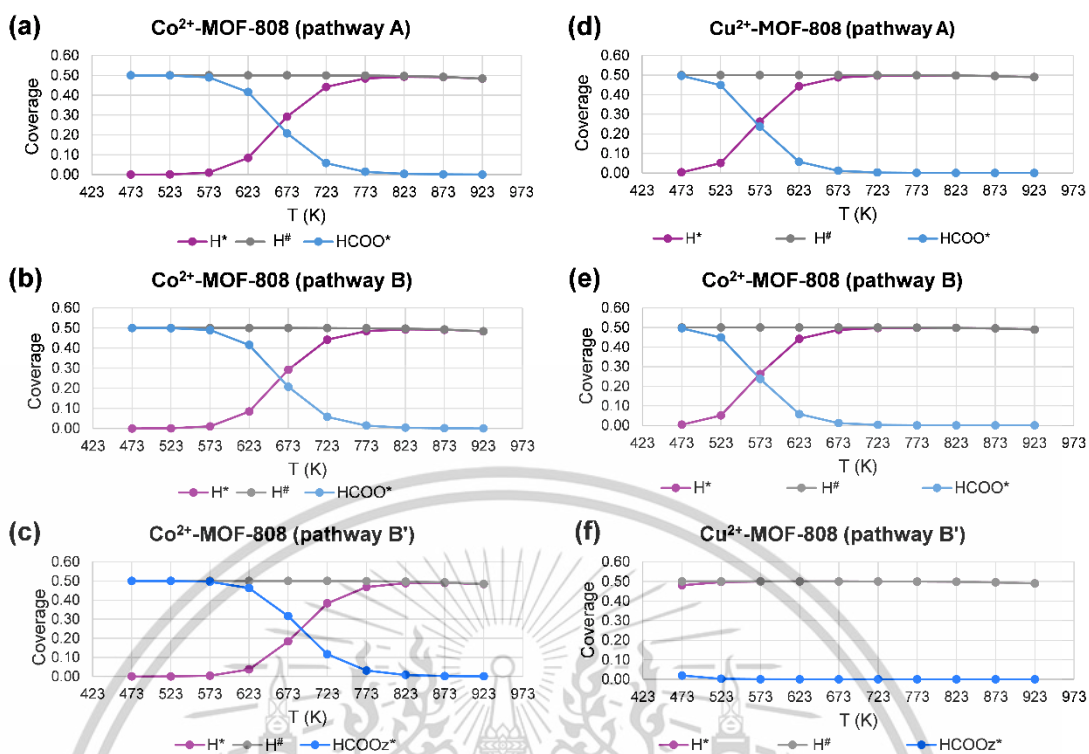


Figure S8. Surface coverages as a function of temperature for Co-MOF: (a) pathway A, (b) pathway B, (c) pathway B'; and for Cu-MOF: (d) pathway A, (e) pathway B, (f) pathway B'. Noted that species with zero coverage are not shown.

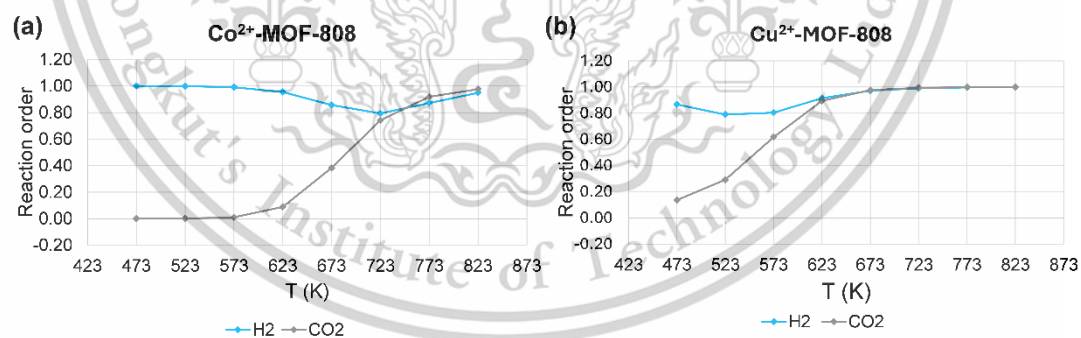


Figure S9. Reaction order as a function of temperature for (a) Co^{2+} -MOF-808 and (b) Cu^{2+} -MOF-808.

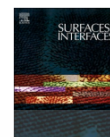
Appendix B: Publication

Surfaces and Interfaces 55 (2024) 105379



Contents lists available at ScienceDirect

Surfaces and Interfaces

journal homepage: www.sciencedirect.com/journal/surfaces-and-interfacesHydrogenation of CO₂ to formic acid catalyzed by Co and Cu Single-atom catalysts supported on MOF-808: A DFT investigationNawarat Kusonjariyakun^a, Jirapat Santatiwongchai^b, Jittima Meeprasert^b, Warot Chotpatiwetchkul^{a,*}, Thana Maihom^c, Sareeya Bureekaew^d, Sarawoot Impeng^{b,*}^a Applied Computational Chemistry Research Unit, Department of Chemistry, School of Science, King Mongkut's Institute of Technology Ladkrabang, Bangkok 10520, Thailand^b National Nanotechnology Center (NANOTEC), National Science and Technology Development Agency (NSTDA), Pathum Thani 12120, Thailand^c Division of Chemistry, Department of Physical and Material Sciences, Faculty of Liberal Arts and Science, Kasetsart University, Kamphaeng Saen Campus, Nakhon Pathom, 73140, Thailand^d Department of Chemical and Biomolecular Engineering, School of Energy Science and Engineering, Vidyasirimedhi Institute of Science and Technology, Rayong 21210, Thailand

ARTICLE INFO

Keywords:

CO₂ hydrogenation
Single-atom catalysts
MOFs
DFT calculations
Microkinetic modeling

ABSTRACT

In this work, DFT-based calculations and microkinetic modeling were employed to investigate CO₂ hydrogenation to formic acid using H₂ over Co and Cu single-atom catalysts supported on MOF-808. We investigated two pathways: one without the introduction of a second H₂ molecule (pathway A) and another one with it (pathway B). Pathway B, which involves introducing the second H₂ molecule alongside the formate intermediate from the first step, exhibits significantly lower energy barriers (three times lower) for the transformation into formic acid in the second step of CO₂ hydrogenation. Moreover, pathway B shifts the reaction thermodynamics from endergonic to exergonic, highlighting its kinetic and thermodynamic advantages. Notably, we observed formate intermediates with quasi-bidentate geometry alongside the prevalent bidentate chelating geometry. Cu²⁺-MOF-808 exhibits superior catalytic activity compared to Co²⁺-MOF-808, attributed to Cu's stronger preference for stabilizing the transition state in its square planar geometry through the Jahn-Teller effect, which is less effective in Co. Furthermore, our microkinetic modeling consistently confirms that Cu²⁺-MOF-808 outperforms Co²⁺-MOF-808 at lower temperatures, with the rate of formic acid production depending on the concentration of H₂. The desorption of formic acid is identified as the rate-determining step of the reaction, significantly impacting overall efficiency.

1. Introduction

Carbon dioxide (CO₂) emissions, primarily resulting from the combustion of fossil fuels, are major contributors to global warming and climate change. Carbon capture, utilization, and storage (CCUS) are recognized as crucial technologies for addressing these environmental issues [1,2]. Consequently, there is substantial research focused on the development of adsorptive and catalytic materials for CO₂ capture and conversion into valuable chemicals.

Among the various chemical processes for converting CO₂ into valuable chemicals, the hydrogenation of CO₂ to produce formic acid has gained considerable attention due to its numerous applications in food and textile industries [3–7]. However, the catalytic hydrogenation

of CO₂ to formic acid using H₂ poses a significant challenge due to the inherent stability of CO₂ ($\Delta G_{298}^{\circ} = -394.4$ kJ/mol). Moreover, this reaction is thermodynamically unfavorable ($\Delta G_{298}^{\circ} = +32.9$ kJ/mol) [8]. Therefore, the development of highly active and effective catalysts for formic acid production through CO₂ hydrogenation using H₂ remains challenging.

Metal-organic frameworks (MOFs) are crystalline porous materials formed by the coordination of metal ions/clusters with organic linkers [9,10]. A diverse combination of readily available metal ions/clusters and organic linkers results in numerous MOFs, each having distinctive properties including high specific surface area, varied size and pore structure and high thermal and chemical stability. These characteristics make MOFs highly attractive for a wide range of applications such as gas

* Corresponding authors.

E-mail addresses: warot.ch@kmitl.ac.th (W. Chotpatiwetchkul), sarawoot.imp@nanotec.or.th (S. Impeng).<https://doi.org/10.1016/j.surfin.2024.105379>

Received 14 July 2024; Received in revised form 29 October 2024; Accepted 31 October 2024

Available online 7 November 2024

2468-0230/© 2024 Elsevier B.V. All rights are reserved, including those for text and data mining, AI training, and similar technologies.

storage and separation as well as catalysis [11,12].

Zr-based MOFs such as UiO-66 [13], NU-1000 [14], and MOF-808 [15] are known for their structural defects like missing ligands. These defects have attracted significant attention for their role as catalysts and as support platforms for anchoring metal single-atom catalysts (SACs) [16–22]. They play a significant role in enhancing catalytic activity by creating active sites within the frameworks and preventing aggregation of loaded SACs, thereby maximizing efficiency. In a recent study by Zhang et al. [23], MOF-808 modified with single-ion Zn^{2+} , incorporated into Zr-oxide node, exhibited remarkable selectivity for CO_2 hydrogenation to methanol. Following this, Liu et al. [24] conducted a theoretical investigation into the reaction pathways of CO_2 hydrogenation to various C1 products (CO , $HCOOH$, CH_3OH , and CH_4) on MOF-808-supported several metal ions including Cu^{2+} , Fe^{2+} , Pt^{2+} , Ni^{2+} , and Pd^{2+} . Among these catalysts, Cu^{2+} -MOF-808 was reported as the most active catalyst. Although their findings are valuable, further details on reaction mechanism are still needed to enhance our understanding and guide the rational design of catalysts.

In this work, we used DFT calculations and microkinetic modeling to investigate the hydrogenation of CO_2 to formic acid on Co^{2+} - and Cu^{2+} -MOF-808 catalysts. We included Co^{2+} to assess its potential benefits alongside Cu^{2+} , which is known for its effectiveness. A key contribution of our work is the identification of the formate intermediate in both quasi-bidentate and chelating geometries, with the quasi-bidentate structure being a novel finding not previously reported. For Co^{2+} , both geometries exhibit similar energetic stability, while Cu^{2+} shows a slight energy difference between the quasi-bidentate and chelating structures. These distinct geometries enable two different pathways for introducing a second H_2 molecule, which is crucial for converting the formate intermediate into formic acid.

Our analysis highlights the roles of the electronic structure and spin states for both Co^{2+} and Cu^{2+} , particularly the Jahn-Teller effect in Cu^{2+} , which significantly influences its catalytic activity and the stability of reaction intermediates. Furthermore, we provide a clear comparison of the differences between the quasi-bidentate and chelating pathways. Overall, our findings offer valuable insights into the reaction mechanism and present a detailed comparison of Co^{2+} - and Cu^{2+} -MOF-808 catalysts. By emphasizing the differences in catalytic pathways and the influence of electronic structure and spin states, this research enhances our understanding of CO_2 hydrogenation and suggests new directions for exploring alternative catalytic strategies, making a significant contribution to the fields of surface chemistry and catalysis.

2. Computational details

The finite-cluster model was employed to investigate the hydrogenation of CO_2 to formic acid over Co and Cu single-atom catalysts supported on MOF-808. The Zr-oxide cluster was derived from the crystal structure of MOF-808 [15], where the carboxylate groups of 1,3,

5-benzenetricarboxylate (BTC) linkers were truncated and capped with hydrogen atoms. Based on previous work [23], where Zn^{2+} -supported MOF-808 was successfully synthesized via post-synthetic metalation, we modeled Co and Cu single-atom catalysts supported on Zr-oxide node by replacing the capping formates with $-OH^-/-OH_2$ groups. Subsequently, one water molecule and two protons from the terminal hydroxyl group and μ_3-OH in the Zr-oxide node were removed, resulting in vacant sites where Co and Cu atoms were then placed. Illustrations of catalyst cluster models before and after metalation are shown in Fig. 1.

In this study, spin-unrestricted DFT calculations were performed with the M06-L density functional [25]. The def2-SVP [26] was employed for C, H, and O atoms, while the SDD pseudopotential basis set [27] was used for Cu, Co, and Zr transition metal atoms. During geometry optimization, only the carbon atoms of the terminal carboxylate groups, which are capped by hydrogen atoms, were kept fixed. Charge analysis was conducted using the Natural Bond Orbital (NBO) method [28]. The Gibbs free energies were determined at 298.15 K and 1 atm through frequency calculations using the M06L/def2-TZVP, which incorporates the Grimme D3 dispersion correction [29]. All calculations were carried out using Gaussian 16 [30]. The spin states of the catalyst model were examined. The calculated results revealed doublet and quartet ground spin states for Cu^{2+} - and Co^{2+} -MOF-808 (Table S1). There was no spin crossing during the reaction mechanism (see Supplementary data).

Gibbs free energy profiles were calculated as:

$$\Delta G = G_{\text{gas}}/M^{2+}\text{-MOF-808} - (G_{\text{gas}} + G_{(M^{2+}\text{-MOF-808})}) \quad (1)$$

where $G_{\text{gas}}/M^{2+}\text{-MOF-808}$ is the Gibbs free energy of the complex, and G_{gas} and $G_{(M^{2+}\text{-MOF-808})}$ are the Gibbs free energies of the corresponding gas molecule and M^{2+} -MOF-808 catalyst, respectively.

To better understand the catalytic activity of Co^{2+} - and Cu^{2+} -MOF-808 in the hydrogenation of CO_2 to formic acid, mean-field microkinetic modeling (MKM) was conducted, based on DFT-calculated elementary reaction steps. Additional details on the MKM methodology are provided in the Supplementary data.

3. Results and discussion

3.1. Structure, electronic properties and stability of Co^{2+} - and Cu^{2+} -MOF-808

Fig. 2 shows the optimized structures of Co^{2+} - and Cu^{2+} -MOF-808 in their most stable spin states: quartet and doublet states, respectively. The relative energies for all possible spin states of Co^{2+} - and Cu^{2+} -MOF-808 are listed in Table S1. The optimized structures reveal that both Co and Cu ions are bound to two oxygen atoms, with one coordinated to the μ_3-O atom and the other to the terminal O atom of the neighboring Zr

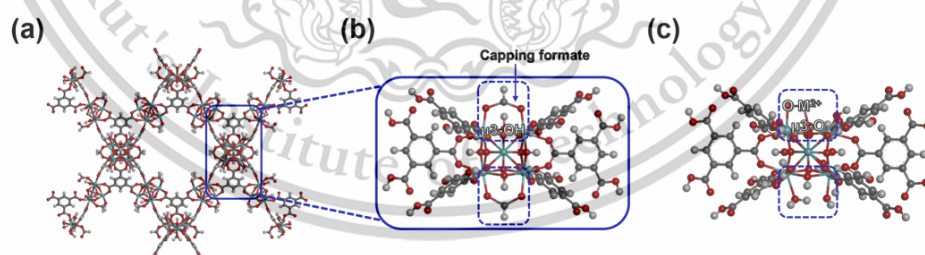


Fig. 1. Structure of MOF-808 (a) and the catalyst cluster models before (b) and after metalation (c) with Co and Cu single atoms. Zr, O, C and H atoms are depicted in cyan, red, dark gray and white, respectively.

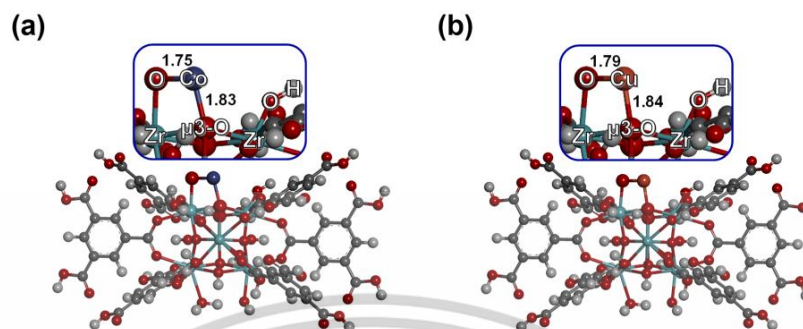
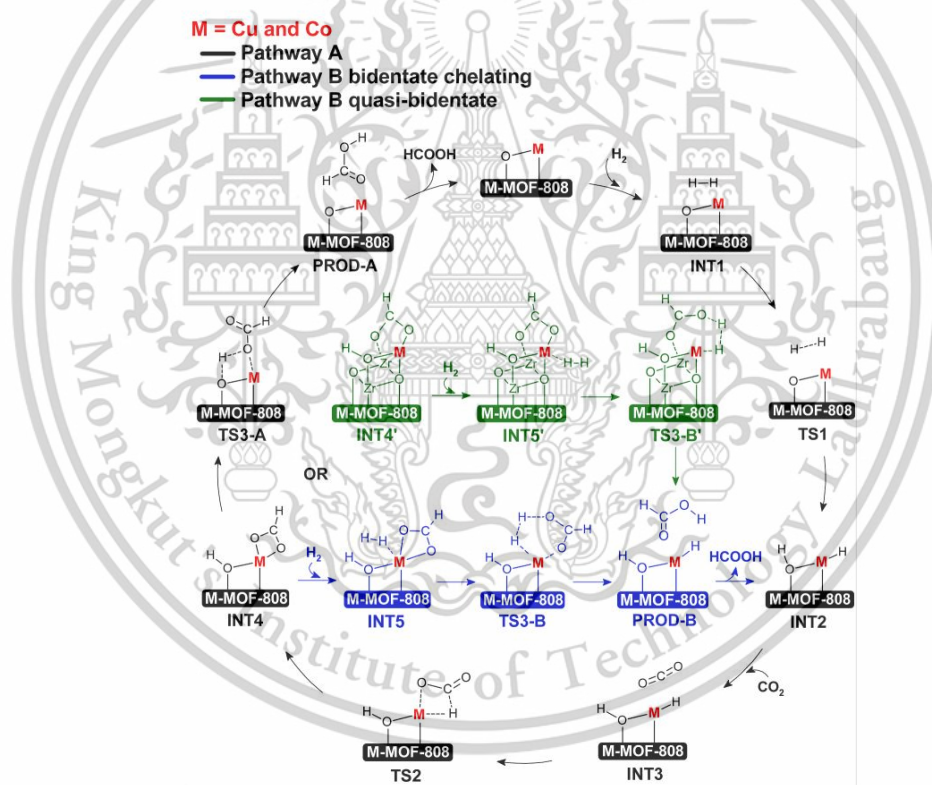


Fig. 2. Optimized structures of (a) Co^{2+} -MOF-808 (quartet spin state) and Cu^{2+} -MOF-808 (doublet spin state). Bond lengths are in Å.

atom of Zr-oxide cluster. These coordination configurations feature C–O bond distances averaging around 1.8 Å. The electron configurations of Co and Cu ions are predicted to be $\text{Co}=4s^{0.42}3d^{7.37}4p^{0.03}4d^{0.01}$ and

$\text{Cu}=4s^{0.38}3d^{9.47}4p^{0.03}$, respectively. Furthermore, the charges of Co and Cu are 1.16 |e| and 1.11 |e|, while the coordinated oxygen atoms carry a negative charge close to -1 |e|. This leads to the assignment of Co^{2+} and



Scheme 1. Two possible pathways for CO_2 hydrogenation to formic acid using H_2 over Co^{2+} - and Cu^{2+} -MOF-808 catalysts.

Cu^{2+} . Note that the charges of Co and Cu ions are found to be less than the expected 2+, probably due to the influence of metal-O coordination bonds. Consistent with previous study [24], the stability of these Co^{2+} and Cu^{2+} ions supported on MOF-808 was investigated based on the replacement energy. The calculated replacement Gibbs free energies are -200.7 kcal/mol and -245.2 kcal/mol for Co-MOF-808 and Cu-MOF-808, respectively. These values are significantly more negative than their respective bulk cohesive energies of the metallic phases, which are -101.2 kcal/mol per atom for Co and -80.5 kcal/mol per atom for Cu, respectively [31]. This indicates that both Co^{2+} and Cu^{2+} ions are strongly stabilized on the MOF-808 support, effectively preventing clustering. The strong bindings of these metal ions to the MOF support ensure their stability within the material, paving the way for further exploration as single-atom catalysts for CO_2 hydrogenation to formic acid.

3.2. Reaction mechanisms of CO_2 hydrogenation to formic acid

Several studies have explored CO_2 hydrogenation with H_2 on single-atom catalysts supported on MOFs, zeolites, and carbon materials [23, 24, 32–41]. This process typically begins with the adsorption and subsequent dissociation of H_2 . After that CO_2 hydrogenation proceeds via formate (HCOO) and carboxyl (COOH) intermediates, often favoring the formate mechanism. However, the formate intermediate strongly binds to the catalytic sites in a bidentate fashion, leading to a high energy barrier for its conversion to formic acid product (HCOOH). To overcome this challenge, adding a second H_2 molecule has emerged as an effective strategy to reduce this energy barrier.

Based on these earlier studies, we propose two possible reaction mechanisms for CO_2 hydrogenation with H_2 , outlined in Scheme 1. The reaction initiates with H_2 adsorption and dissociation, followed by CO_2 hydrogenation to formic acid in two steps: first, the formation of formate intermediate. In the second step, the formate intermediate, adopting a chelating structure, transforms into formic acid. We designated this

mechanism as pathway A. Additionally, to lower an energy barrier in formic acid formation, we introduce a second H_2 molecule alongside the formate intermediate, denoted as pathway B. Unlike previous studies, we observed formate intermediate in both quasi-bidentate and chelating geometries, enabling the introduction of a second H_2 to further facilitate its reduction to formic acid. Further details of these proposed reaction mechanisms are discussed in the following sub-sections.

3.2.1. Pathway A: without introducing a second H_2 molecule

Fig. 3 depicts the energy profile of CO_2 hydrogenation with H_2 on Co^{2+} and Cu^{2+} -MOF-808, accompanied by their corresponding optimized structures along the reaction pathway. The calculated H_2 adsorption energies are -2.0 kcal/mol and -0.4 kcal/mol for Co^{2+} - and Cu^{2+} -MOF-808, respectively. Considering the optimized structures (INT1), the H—H bond distance is significantly elongated to approximately 0.8 Å, compared to the isolated H_2 molecule's bond distance of approximately 0.7 Å, indicating H_2 activation upon adsorption. Additionally, the intermolecular distances between the activated H_2 and Co^{2+} and Cu^{2+} sites are approximately 1.7 Å.

After activation, H_2 undergoes dissociation via the transition state (TS1) with the calculated energy barrier of 4.7 kcal/mol for and Cu^{2+} -MOF-808, similar to the 7.7 kcal/mol barrier reported in previous work [24]. Notably, this process is barrierless for Co^{2+} -MOF-808 in terms of Gibbs free energy (ΔG), but it has an energy barrier of 9.8 kcal/mol in terms of activation energy (ΔE) (see Supplementary data). The energy barriers are within the range of 7.7 – 26.7 kcal/mol observed for H_2 dissociation over the M^{2+} -MOF-808 ($\text{M}^{2+} = \text{Cu}^{2+}, \text{Fe}^{2+}, \text{Pt}^{2+}, \text{Ni}^{2+}, \text{and Pd}^{2+}$) catalysts [24]. At this stage, the bond distance of activated H_2 is further elongated by approximately 0.1 Å, compared to the previous adsorption step. Moreover, one H atom (H1) approaches the terminal oxygen atom, whereas the other one (H2) resides on the Co^{2+} and Cu^{2+} sites. Considering the charges of this TS1, H1 carries a positive charge of around $+0.2$ |e|, whereas H2 exhibits a negative charge of -0.2 |e|. This indicates the heterolytic cleavage process of H_2 during dissociation. The

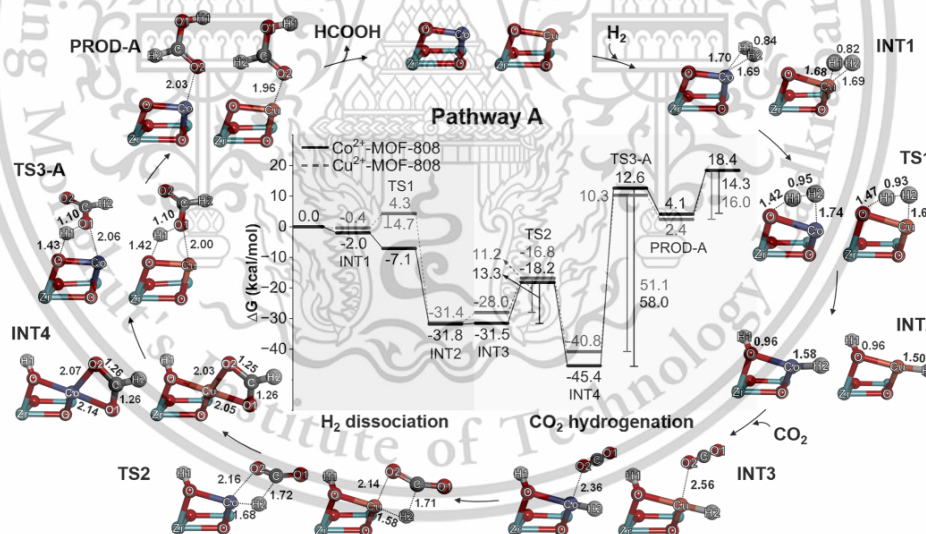


Fig. 3. Gibbs free energy profile and corresponding optimized structures of intermediate (INT), transition state (TS), and product (PROD) for CO_2 hydrogenation to formic acid using H_2 over Co^{2+} - and Cu^{2+} -MOF-808 via the chelating formate intermediate, without the introduction of a second H_2 molecule in pathway A.

transition states exhibit imaginary frequency values of 488.3i cm⁻¹ and 593.1i cm⁻¹ for Co²⁺- and Cu²⁺-MOF-808, respectively.

The collapse of TS1 results in the formation of Co- and Cu-hydride (Co- and Cu-H2) and hydroxyl group (OH1) on the Zr-oxide cluster of MOF-808 (INT2). This step is exergonic by -31.8 kcal/mol and -31.4 kcal/mol for Co- and Cu-MOF-808, respectively. As outlined in Table S2 and S5, the charges on Co and hydride are 1.19 |e| and -0.47 |e|, while for Cu and hydride, they are 1.00 |e| and -0.36 |e|, respectively. Furthermore, the bond distances for Co-hydride and Cu-hydride are predicted to be 1.58 Å and 1.50 Å, respectively (see INT2). The longer distance and higher charges for Co-hydride suggest a greater ionic character compared to Cu-hydride.

The reaction subsequently progresses to the adsorption of CO₂ (INT3), where CO₂ binds weakly to Co or Cu site with intermolecular distances exceeding 2.3 Å. The hydride (H2) is then transferred to the adsorbed CO₂ via the transition state (TS2). The geometry of this transition state reveals a nearly co-planar structure, evidenced by the M-O₂-C-H₂ dihedral angles of -6.0° and -5.9° for Co²⁺- and Cu²⁺-MOF-808, respectively. As a result, the adsorbed CO₂ undergoes significant bending, as reflected in the bond angles of 152.3° and 154.4°, respectively. The C-H₂ and Co-O₂/Cu-O₂ distances are approximately 1.7 Å and 2.1 Å, respectively, suggesting bond formation between them. The transition states have imaginary frequency values of 585.3i cm⁻¹ and 533.6i cm⁻¹ for Co²⁺- and Cu²⁺-MOF-808, respectively, relating the formation of the C-H₂ bond and the cleavage of Co- and Cu-hydride bonds. The calculated energy barrier is 13.3 kcal/mol for Co²⁺-MOF-808 and 11.2 kcal/mol for Cu²⁺-MOF-808, respectively. These energy barriers are comparable to those reported in previous works on CO₂ hydrogenation using metal hydrides as active sites, ranging from 8.5 kcal/mol to 16.8 kcal/mol [24,33].

The subsequent collapse of TS2 results in the formation of formate intermediate adopting a bidentate chelating structure denoted as INT4, which is more stable in energy than the TS2 by 27.2 kcal/mol and 24.0 kcal/mol for Co²⁺- and Cu²⁺-MOF-808 catalysts, respectively. In INT4, the C-O1 distance is approximately 1.25 Å, equivalent to the C-O2 distance. Additionally, the metal-O bonds between the formate intermediate and Co and Cu sites are around 2.05 Å, confirming the bidentate chelating configuration.

Subsequently, the formic acid product is obtained via the transition state (TS3-A). This process involves the transfer of a proton (H1) from hydroxyl group (OH1) to one of oxygen atoms (O2) of the formate intermediate. NBO charge analysis indicates that the H1 has a charge of 0.55 |e| for Co²⁺-MOF-808 and 0.56 |e| for Cu²⁺-MOF-808. The transition states exhibit imaginary frequency values of 820.7i cm⁻¹ and 794.0i cm⁻¹ for Co²⁺- and Cu²⁺-MOF-808, respectively. These correspond to the proton (H1) transfer from hydroxyl group to formate and the formation of the O1-H1 bond. In TS3, the O-H1 and H1-O1 distances are approximately 1.4 Å and 1.1 Å for both Co²⁺- and Cu²⁺-MOF-808. Furthermore, compared to the INT4, the Co-O1 and Cu-O1 distances remain around 2 Å, whereas the Co-O2 and Cu-O2 bonds are completely broken, with O2 pointing upward. These geometric changes contribute to a high energy barrier for this step, calculated to be 58.0 kcal/mol and 51.1 kcal/mol for Co²⁺- and Cu²⁺-MOF-808, respectively. The second hydrogenation step exhibits the highest energy barrier compared to H₂ dissociation and the first step of CO₂ hydrogenation. Although this step is consistent with previous studies as the rate-determining step [35,36,40], our microkinetic modeling based on ΔE at the uM06L/def2-TZVP/SDD level of theory, suggests that the desorption energy of formic acid (HCOOH) is the true rate determining step. We will discuss this in detail later.

Finally, the desorption of formic acid product from the Co²⁺- and Cu²⁺-MOF-808 catalysts requires energy barriers of 14.3 kcal/mol and 16.0 kcal/mol, respectively. These values are consistent with the literature-reported values for formic acid desorption from Cu-embedded graphene which is around 20 kcal/mol [35]. Overall, the CO₂ hydrogenation to formic acid is found to be endergonic by 18.4 kcal/mol,

indicating an unfavorable reaction energetically. This observation correlates with the standard Gibbs free energy change (ΔG₂₉₈) of the reaction at 32.9 kJ/mol [8].

3.2.2. Pathway B: with introducing a second H₂ molecule

Typically, a formate intermediate can adsorb on the catalyst surface in either a bidentate or bridging geometry, depending on the surface characteristics. In the bidentate configuration, the formate binds to one catalytic site via two oxygen atoms, whereas in the bridging arrangement, it coordinates with two metal centers. As depicted in Figs. 4 and 5, the two C-O bond distances in the formate intermediate INT4' closely resemble those observed in the bidentate chelating geometry (INT4), approximately 1.25 Å. However, INT4' is observed to coordinate with one catalytic site (Co or Cu) using one oxygen atom (O2), while the other oxygen atom (O1) exhibits a longer distance to the neighboring Zr atom of the Zr-oxide node. More specifically, the Co- and Cu-O2 bond distances are ~1.9 Å, while the Zr-O1 distances are ~2.4 Å for both Co²⁺- and Cu²⁺-MOF-808 catalysts. This geometric observation indicates a quasi-bidentate geometry in INT4', similar to [42]. Furthermore, the O-C-O bond angle is around 120° in the chelating structure and approximately 125° in the quasi-bidentate geometry. Vibrational mode calculations reveal a split in the symmetric and asymmetric O-C-O stretching vibrations: 201 cm⁻¹ and 213 cm⁻¹ for bidentate chelating and quasi-bidentate on Co²⁺-MOF-808, and 181 cm⁻¹ and 203 cm⁻¹ on Cu²⁺-MOF-808 (see Table 1). The splitting differences are 12 cm⁻¹ and 22 cm⁻¹ for Co²⁺ and Cu²⁺-MOF-808, respectively. This difference influences stability, with the chelating geometry being more stable than the quasi-bidentate by 9.3 kcal/mol for Cu²⁺-MOF-808 (-40.8 kcal/mol versus -31.5 kcal/mol). Conversely, for Co²⁺-MOF-808, both configurations show similar stability, around -45 kcal/mol.

When a second H₂ is introduced alongside the bidentate chelating and quasi-bidentate geometries, the distances between the formate intermediate and Co/Cu site slightly increase (see INT5 and INT5'). This lengthening occurs due to the adsorption of the second H₂ molecule on Co/Cu site adjacent to the formate intermediate, leading to the formation of H₂-formate co-adsorption geometries. In INT5 and INT5', the intermolecular distance between the adsorbed H₂ and Co/Cu sites is around 2 Å, and the adsorbed H₂ reveals a bond distance of around 0.8 Å. This process is slightly endergonic, resulting in an energy increase of approximately 5 kcal/mol in both bidentate chelating and quasi-bidentate pathways for both Co²⁺- and Cu²⁺-MOF-808 catalysts.

The formic acid is then formed via the transition state (TS3-B). During this state, the H3-H4 bond of the second H₂ molecule undergoes dissociation and transfers to the Co/Cu site and formate intermediate. The H3-H4 bond distance stretches from ~0.8 Å to ~1.0 Å, while the Co-H4 and Cu-H4 distances contract to ~1.7 Å. In the case of Co²⁺-MOF-808, the transition states exhibit imaginary frequency values of 540.9i cm⁻¹ and 784.3i cm⁻¹ for the bidentate chelating and quasi-bidentate pathways, respectively. Correspondingly, for Cu²⁺-MOF-808, the values are 949.1i cm⁻¹ and 889.9i cm⁻¹, indicating the simultaneous H3-H4 bond breaking and the formation of the O2-H3 and Co/Cu-H4 bonds. The energy barriers for this step are 16.4 kcal/mol and 17.5 kcal/mol for the quasi-bidentate and bidentate chelating pathways in Co²⁺-MOF-808. Conversely, Cu²⁺-MOF-808 exhibits lower energy barriers of 13.3 kcal/mol and 14.0 kcal/mol for the same pathways. This suggests that Cu is more effective in facilitating this step, likely due to its stronger preference for the Jahn-Teller effect in the Cu²⁺ (d⁹) doublet state compared to Co²⁺ (d⁷) with a high-spin quartet state [43]. This difference is clearly illustrated in the TS3-B structure, where Cu tends to adopt a square planar geometry stabilized by the Jahn-Teller effect. The observed bond angles, approximately 90° and 160°, are close to the typical angles of a true square planar configuration (90° and 180°), as shown in the inset of Fig. 5. In contrast, Co, with its (d⁷) high-spin quartet state and a weaker Jahn-Teller effect, shows a lesser tendency to adopt a square planar geometry (see the inset in Fig. 4). As a result, Co²⁺-MOF-808 has a higher energy barrier. Additionally, compared to

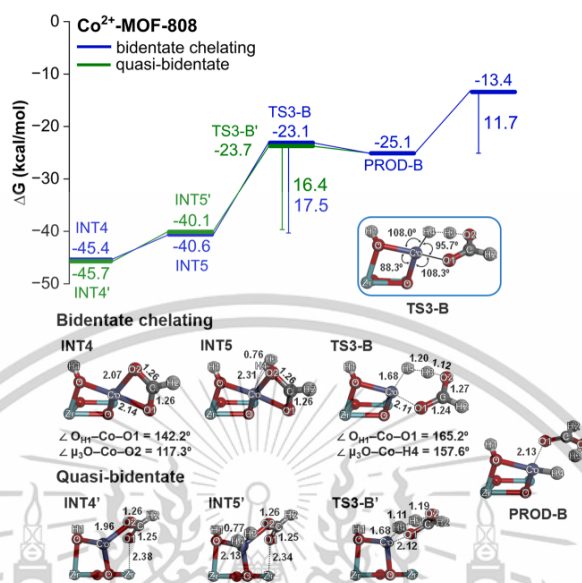


Fig. 4. Gibbs free energy profile and corresponding optimized structures of the intermediate (INT), transition state (TS), and product (PROD) for CO_2 hydrogenation to formic acid using H_2 over Co^{2+} -MOF-808. Pathway B investigates two routes—bidentate chelating and quasi-bidentate—by introducing a second H_2 molecule. The inset shows the structure of TS3-B, where Co adopts a less square planar geometry.

pathway A, introducing a second H_2 molecule significantly reduces the energy barrier for converting the formate intermediate to formic acid by approximately threefold.

To understand the stability differences between the bidentate chelating and quasi-bidentate pathways, we investigated the electronic properties of Co^{2+} and Cu^{2+} metal sites using the simplified models, $\text{Co}(\text{O}_2\text{CH})_2$ and $\text{Cu}(\text{O}_2\text{CH})_2$. These models represent Co^{2+} and Cu^{2+} coordinated to four oxygen atoms, mimicking their coordination environment in MOFs. We chose formate ligands because they effectively represent our system and provide weak coordination that stabilizes Co^{2+} in high-spin quartet states. Typically, metal complexes with a coordination number of four (ML_4) adopt either square planar or tetrahedral geometry. Fig. 6a shows the optimized structures of $\text{Co}(\text{O}_2\text{CH})_2$ and $\text{Cu}(\text{O}_2\text{CH})_2$ under symmetry constraints, along with their relative energetic stabilities. The $\text{Cu}(\text{O}_2\text{CH})_2$ favors a square planar configuration with D_{2h} symmetry over a non-planar and quasi-tetrahedral configuration with D_{2d} symmetry, exhibiting greater stability by 17.9 kcal/mol. In contrast, both configurations of $\text{Co}(\text{O}_2\text{CH})_2$ exhibit similar stability, with the square planar configuration being only 0.7 kcal/mol more stable. This similarity demonstrates the flexibility of Co^{2+} , which can adopt various geometries such as octahedral and tetrahedral geometries, depending on its coordination number. It is important to note that a true tetrahedral configuration is not achievable due to the chelating coordination of the formate ligands.

To further elucidate the electronic and Jahn-Teller effects, we present a schematic d-orbital splitting diagram for ML_4 in both tetrahedral and square planar geometries (Fig. 6b). In the Cu^{2+} (d^9) configuration, reducing symmetry from tetrahedral to square planar lifts the degeneracy of the t_2 orbital set, thereby stabilizing the system. Consequently, the singly occupied $d_{x^2-y^2}$ orbital is elevated to a higher energy level, illustrating that the Jahn-Teller effect favors the square planar

geometry. In contrast, the Co^{2+} (d^7) configuration in high-spin quartet state exhibits similar stability in both tetrahedral and square planar geometries. This is due to Co^{2+} (d^7) having three singly occupied orbitals, with the degree of orbital splitting upon reducing symmetry from tetrahedral to square planar being less pronounced than in Cu^{2+} . Unlike Cu^{2+} (d^9), which undergoes significant Jahn-Teller distortion that destabilizes the $d_{x^2-y^2}$ orbital, the orbital splitting in Co^{2+} is minimal. As a result, the singly occupied $d_{x^2-y^2}$ orbital is only slightly higher in energy than the other two singly occupied orbitals, leading to comparable stability between the tetrahedral and square planar geometries.

Overall, these computational results demonstrate how electronic and Jahn-Teller effects influence the stability differences between Co^{2+} and Cu^{2+} in both tetrahedral and square planar structures. This understanding deepens our insight into the distinctions between the bidentate chelating and quasi-bidentate pathways. Notably, bidentate chelating is more stable than quasi-bidentate for Cu^{2+} -MOF-808, whereas the two pathways show comparable stability for Co^{2+} -MOF-808. This difference stems from the Cu^{2+} 's preference for a square planar structure, which is stabilized by the Jahn-Teller effect. This is evidenced by the *trans* bond angles in bidentate chelating intermediate (INT4), measuring approximately 167° for Cu^{2+} -MOF-808, compared to 142° and 117° for Co^{2+} -MOF-808, as shown in Figs. 4 and 5.

Finally, the desorption of formic acid occurs with activation energies of 11.7 kcal/mol and 7.0 kcal/mol for Co^{2+} - and Cu^{2+} -MOF-808, respectively. These energy barriers are lower than those in pathway A, probably due to formic acid adsorbing on Co- and Cu-hydride sites rather than on open Co and Cu single-atom sites, which provide greater accessibility for interaction with formic acid. In pathway B, the second CO_2 hydrogenation step completes and frees Co- and Cu-hydride sites for the next CO_2 hydrogenation cycle. The CO_2 hydrogenation is exergonic by ~ 13 kcal/mol, indicating a favorable process. This result highlights

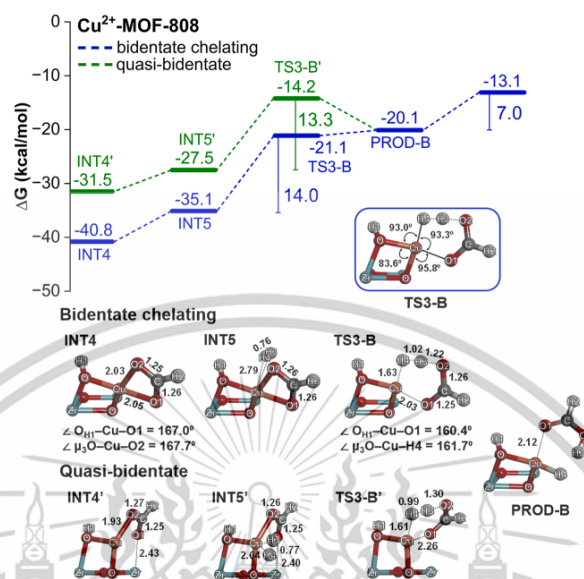


Fig. 5. Gibbs free energy profile and corresponding optimized structures of the intermediate (INT), transition state (TS), and product (PROD) for CO₂ hydrogenation to formic acid using H₂ over Cu²⁺-MOF-808. Pathway B investigates two routes—bidentate chelating and quasi-bidentate—by introducing a second H₂ molecule. The inset shows the structure of TS3-B, where Cu is arranged in a nearly square planar geometry.

Table 1
Vibrational modes of formate intermediate in chelating and quasi-bidentate geometries on Co²⁺- and Cu²⁺-MOF-808.

Vibrational mode	Co ²⁺ -MOF-808		Cu ²⁺ -MOF-808	
	wavenumber (cm ⁻¹)	Δ (cm ⁻¹)	wavenumber (cm ⁻¹)	Δ (cm ⁻¹)
chelating ν _s (OCO)	1402	201	1405	181
chelating ν _{as} (OCO)	1603		1586	
quasi-bidentate ν _s (OCO)	1389	213	1389	203
quasi-bidentate ν _{as} (OCO)	1602		1592	

the importance of introducing a second H₂ molecule, which significantly lowers the energy barrier for converting a formate intermediate into formic acid. Furthermore, it shifts the reaction's thermodynamics from an endergonic to exothermic, suggesting that the rate of formic acid formation may depend on the concentration of H₂. Moreover, the lower energy barrier observed for Cu in our DFT calculations further emphasizes its superior activity in the CO₂ hydrogenation reaction.

3.2.3. Microkinetic modeling

The mean-field microkinetic modeling (MKM) was conducted using a dual-site model representation, with Cu/Co (*) and oxygen (O*) atoms of Co²⁺- and Cu²⁺-MOF-808. The ratio of * and # sites was set at 0.5:0.5. The reaction rate, surface coverages, reaction order, and degree of rate control (DRC) were calculated under the following conditions: total pressure = 1 bar, H₂:CO₂ = 1:1, and temperatures (T) ranging from 473 to 823 K. This study investigates the turnover frequency (TOF) with respect to HCOOH production. Table S8 lists all the elementary reaction steps involved in the hydrogenation of CO₂ to HCOOH over Co²⁺- and

Cu²⁺-MOF-808, which were included in the MKM simulations.

MKM simulations reveal that the TOF of Cu²⁺-MOF-808 is higher than that of Co²⁺-MOF-808 at temperatures below 673 K. However, above this temperature, Co²⁺-MOF-808 surpasses Cu²⁺-MOF-808 in TOF, as shown in Fig. 7(a). To clarify this, the contribution of each reaction pathway to the TOF was analyzed. Fig. 7(b) and 7(c) show that pathway A has minimal impact on the overall reaction, whereas pathways B (bidentate chelating) and B' (quasi-bidentate) are the dominant mechanisms for both catalysts. As the temperature increases, the TOF for the HCOOH formation via pathways B and B' rises more sharply for Co²⁺-MOF-808 than for Cu²⁺-MOF-808. This explains why Co²⁺-MOF-808 surpasses Cu²⁺-MOF-808 in TOF at higher temperatures. Additionally, the optimum temperature for HCOOH production for both catalysts is predicted to be around 723 K.

DRC analysis in Fig. 8 reveals that the desorption of formic acid (HCOOH) from the H* site is the rate-determining step for both catalysts. This is consistent with DFT calculations at the uM06L/def2-TZVP/SDD level of theory, which show that the desorption energy of HCOOH in pathways B (bidentate chelating) and B' (quasi-bidentate) exceeds the energy barrier of the most difficult reaction step, the second step of CO₂ hydrogenation to formic acid, see Supplementary data. Moreover, the hydrogenation of the formate intermediate (HCOO*) in both pathways B and B' (H₂HCOO* ↔ H₂HCOOH* and H₂HCOOz* ↔ H₂HCOOH*) has minimal impact on the overall reaction rate at temperatures above 623 K. Fig. 9 shows that # sites are fully covered by H atoms (H#) because H# is primarily consumed in pathway A, which is not the dominant mechanism for either catalyst. HCOO* exhibits the second-highest coverage on Co²⁺- and Cu²⁺-MOF-808 at temperatures below 673 and ~530 K, respectively. At higher temperatures, the amount of HCOO* decreases while H* increases due to its interaction with a second H₂ molecule, leading to formic acid production. Overall, the addition of a second H₂

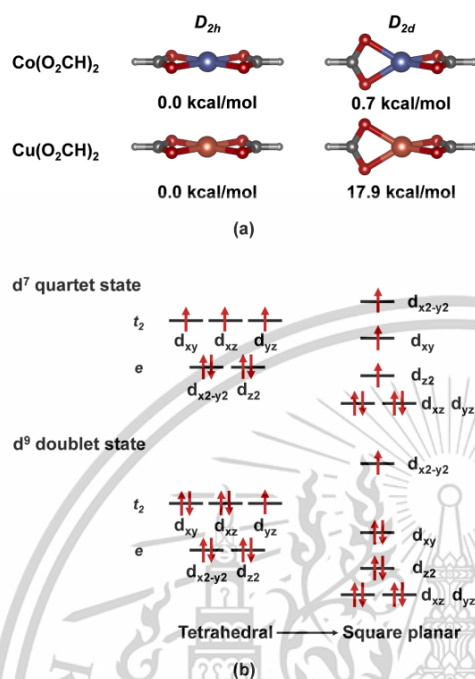


Fig. 6. (a) Optimized structures of $\text{Co}(\text{O}_2\text{CH})_2$ and $\text{Cu}(\text{O}_2\text{CH})_2$ under symmetry constraints, along with their energetic stabilities compared to the most stable configurations in D_{2h} and D_{2d} symmetries. (b) Schematic diagram illustrating the d-orbital splitting for d^7 and d^9 ML_4 complexes.

molecule plays an important role in enhancing the catalytic activity of both Co^{2+} - and Cu^{2+} -MOF-808 for formic acid production. This is further supported by reaction order analysis (Fig. S9), which reveals that the reaction rate is primarily dependent on H_2 concentration, with CO_2 only affecting the rate at higher temperatures.

Overall, MKM simulations indicate that Cu^{2+} -MOF-808 outperforms Co^{2+} -MOF-808 for the hydrogenation of CO_2 to formic acid at temperatures below 673 K. However, Co^{2+} -MOF-808 shows increased activity at higher temperatures. To ensure the stability of single-atom catalysts in

MOFs and prevent cluster formation, it is recommended to maintain the reaction temperature below 573 K, making Cu^{2+} -MOF-808 a better choice for balancing activity and stability. The addition of a second H_2 molecule in pathways B is crucial for enhancing formic acid production. Desorption of formic acid, the rate-determining step for both catalysts, significantly impacts the overall efficiency, emphasizing the need for strategies to reduce the desorption energy or improve product release rates.

While our study provides valuable insights into CO_2 hydrogenation using Co^{2+} - and Cu^{2+} -MOF-808 catalysts, there are important considerations to address. The finite-cluster model we used effectively captures the structural changes and local electronic properties of single-atom catalysts, which are crucial for understanding their performance and reaction mechanisms. However, periodic models may offer a more accurate representation of the MOF framework's rigidity. Despite their higher computational cost due to the large unit cells of MOFs, periodic models could constrain structural flexibility. Nevertheless, we expect this to have only a minor effect on reaction energies and will not significantly alter the overall mechanisms discussed in this work. Additionally, our observation of the quasi-bidentate intermediate geometry, alongside the more commonly observed bidentate chelating geometry, is relatively rare in the literature. This finding would benefit from further experimental validation using Fourier Transform Infrared Reflection-Absorption Spectroscopy (FT-IRRAS), which has been employed with DFT to identify these intermediates [42]. Addressing these limitations in future research could strengthen the validity of our conclusions and broaden their applicability.

4. Conclusion

DFT-based computations were utilized to investigate the reaction mechanism of CO_2 hydrogenation to formic acid over Co and Cu single-atom catalysts supported on MOF-808. We explore two established pathways of the reaction, designated as pathway A and pathway B. Both pathways involve H_2 adsorption and dissociation to generate Co- and Cu-hydride as active centers for CO_2 hydrogenation to formic acid. The hydrogenation reaction then occurs in two steps; first the formation of a formate intermediate, followed by its transformation into formic acid product. The two pathways diverge at the second step of CO_2 hydrogenation, where pathway B introduces a second H_2 molecule alongside the formate intermediate. Our computational results indicate that the H_2 dissociation is feasible with energy barriers below 10 kcal/mol for both Co^{2+} - and Cu^{2+} -MOF-808 catalysts. In pathway A, the second step of CO_2 hydrogenation to produce formic acid is the rate-determining step of the reaction, with high energy barriers of 58.0 kcal/mol and 51.1 kcal/mol for Co^{2+} - and Cu^{2+} -MOF-808, respectively. Interestingly, in pathway B, we observed the formate intermediate adopting bidentate chelating and quasi-bidentate geometries. The addition of a second H_2 molecule into these intermediate configurations

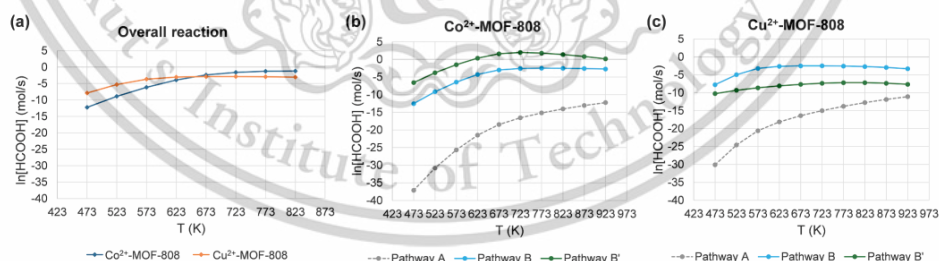


Fig. 7. Turnover frequency (TOF) as a function of temperature for HCOOH production: (a) TOF for overall reaction mechanisms; (b) TOF over Co^{2+} -MOF-808; (c) TOF over Cu^{2+} -MOF-808. Pathways B and B' correspond to bidentate chelating and quasi-bidentate routes, respectively.

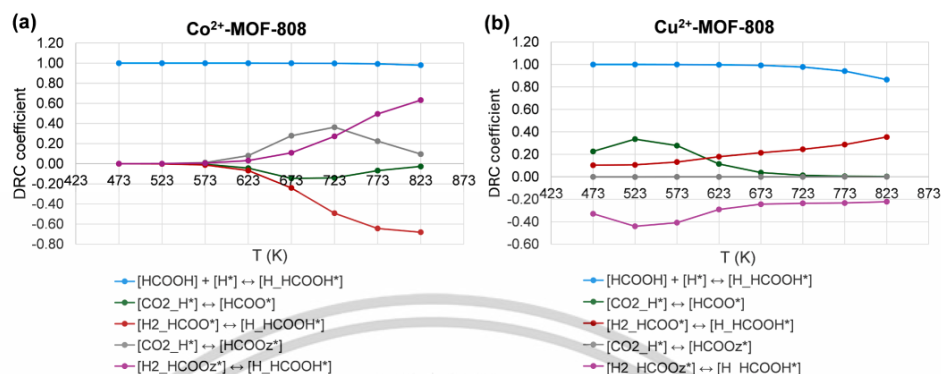


Fig. 8. Degree of rate control (DRC) as a function of temperature: (a) Co²⁺-MOF-808 and (b) Cu²⁺-MOF-808. Note that elementary reaction steps with a zero DRC coefficient are not included.

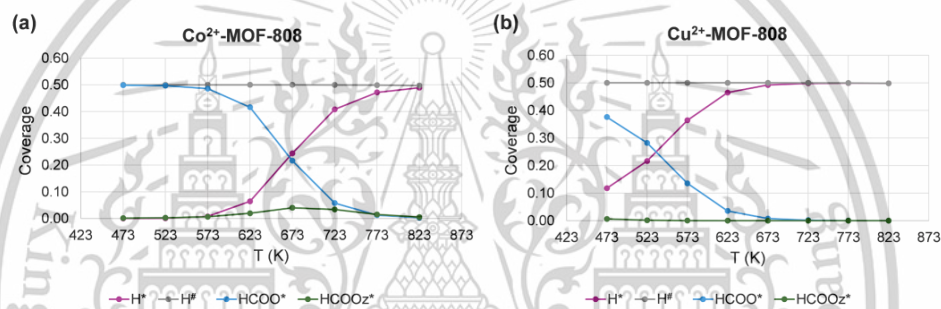


Fig. 9. Surface coverages as a function of temperature: (a) Co²⁺-MOF-808 and (b) Cu²⁺-MOF-808. Note that species with zero coverage are not shown.

significantly lowers energy barriers for this step, which are three times lower compared to pathway A. Overall, pathway B emerges as both kinetically and thermodynamically more favorable than pathway A. Our simulations indicate that Cu²⁺-MOF-808 outperforms Co²⁺-MOF-808 as a catalyst for CO₂ hydrogenation reaction, primarily due to Cu's enhanced ability to stabilize the transition state in its square planar geometry through the Jahn-Teller effect, a capability less pronounced in Co.

CRediT authorship contribution statement

Nawarat Kusunjariyakun: Writing – original draft, Investigation, Formal analysis, Visualization. **Jirapat Santatiwongchai:** Formal analysis, Validation, Visualization. **Jittima Meeprasert:** Investigation, Formal analysis, Visualization. **Warot Chotpatiwetchkul:** Writing – review & editing, Investigation, Methodology, Resources, Funding acquisition, Data curation, Conceptualization. **Thana Maihom:** Formal analysis. **Sareeya Bureekaew:** Formal analysis. **Sarawoot Impeng:** Writing – review & editing, Software, Resources, Investigation, Funding acquisition, Methodology, Data curation, Project administration, Conceptualization, Supervision.

Declaration of competing interest

The authors declare that they have no known competing financial interests or personal relationships that could have appeared to influence the work reported in this paper.

Acknowledgments

N.K. acknowledges the financial support from the School of Science, King Mongkut's Institute of Technology Ladkrabang (Grant No. RA/TA-2565-M-009). W.C. thanks the TSRI and King Mongkut Institute of Technology Ladkrabang (Grant Nos. 2564-02-05-021 and PF66-4274282). We thank Nanoscale Simulation Laboratory at National Nanotechnology Center (NANOTEC) and NSTDA Supercomputer center (ThaiSC) for providing computational resources. This project is co-funded by National Research Council of Thailand (NRCT) and Electricity Generating Authority of Thailand (EGAT) under grant number N25H660015.

Supplementary materials

Supplementary material associated with this article can be found, in the online version, at doi:10.1016/j.surfin.2024.105379.

Data availability

No data was used for the research described in the article.

References

- R.M. Cuéllar-Franca, A. Azapagic, Carbon capture, storage and utilisation technologies: a critical analysis and comparison of their life cycle environmental impacts, *J. CO₂ Util* 9 (2015) 82–102, <https://doi.org/10.1016/j.jcou.2014.12.001>.
- B. Dziejarski, R. Krzyżwińska, K. Andersson, Current status of carbon capture, utilization, and storage technologies in the global economy: a survey of technical assessment, *Fuel* 342 (2023) 127776, <https://doi.org/10.1016/j.fuel.2023.127776>.
- W. Wang, S. Wang, X. Ma, J. Gong, Recent advances in catalytic hydrogenation of carbon dioxide, *Chem. Soc. Rev.* 40 (2011) 3703–3727, <https://doi.org/10.1039/C1CS15008A>.
- W. Li, H. Wang, X. Jiang, J. Zhu, Z. Liu, X. Guo, C. Song, A short review of recent advances in CO₂ hydrogenation to hydrocarbons over heterogeneous catalysts, *RSC Adv* 8 (2018) 7651–7669, <https://doi.org/10.1039/C7RA13546G>.
- R.-P. Ye, J. Ding, W. Gong, M.D. Argyle, Q. Zhong, Y. Wang, C.K. Russell, Z. Xu, A. G. Russell, Q. Li, M. Fan, Y.-G. Yao, CO₂ hydrogenation to high-value products via heterogeneous catalysis, *Nat. Commun.* 10 (2019) 5698, <https://doi.org/10.1038/s41467-019-13628-0>.
- Z. Sun, J. Dong, C. Chen, S. Zhang, Y. Zhu, Photocatalytic and electrocatalytic CO conversion: from fundamental principles to design of catalysts, *J. Chem. Technol. Biotechnol.* 96 (2021) 1161–1175, <https://doi.org/10.1002/jctb.6653>.
- R.R. Ikrededegh, M. Tahir, A critical review in recent developments of metal-organic-frameworks (MOFs) with band engineering alteration for photocatalytic CO₂ reduction to solar fuels, *J. CO₂ Util* 43 (2021) 101381, <https://doi.org/10.1016/j.jcou.2020.101381>.
- Wan-Hui Wang, Yuichiro Himeida, Recent Advances in Transition Metal-Catalysed Homogeneous Hydrogenation of Carbon Dioxide in Aqueous Media, in: Iyad Karamé (Ed.), *Hydrogenation*, IntechOpen, Rijeka, 2012, <https://doi.org/10.5772/48658>, Ch. 10.
- M. Kondo, T. Yoshitomi, H. Matsuzaka, S. Kitagawa, K. Seki, Three-Dimensional Framework with Channeling Cavities for Small Molecules: {M₂(4, 4'-byg)₂(NO₃)₂·xH₂O}_n (M = Co, Ni, Zn), *Angew. Chem. Int. Ed.* 36 (1997) 1725–1727, <https://doi.org/10.1002/ange.199717251>.
- M. Eddoudi, J. Kim, N. Rosi, D. Vodak, J. Wachter, M. O'Keeffe, O.M. Yaghi, Systematic design of pore size and functionality in isoreticular MOFs and their application in methane storage, *Science* 295 (2002) 469–472, <https://doi.org/10.1126/science.1067208>.
- P.Z. Moghadam, Y.G. Chung, R.Q. Snurr, Progress toward the computational discovery of new metal-organic framework adsorbents for energy applications, *Nat. Energy* 9 (2024) 121–133, <https://doi.org/10.1038/s41560-023-01417-2>.
- J. Lee, O.K. Farha, J. Roberts, K.A. Scheidt, S.T. Nguyen, J.T. Hupp, Metal-organic framework materials as catalysts, *Chem. Soc. Rev.* 38 (2009) 1450–1459, <https://doi.org/10.1039/B907080F>.
- J.H. Cavka, S. Jakobsen, U. Østbye, N. Guillou, C. Lamberti, S. Bordiga, K. P. Lillerud, A New Zirconium Inorganic Building Brick Forming Metal Organic Frameworks with Exceptional Stability, *J. Am. Chem. Soc.* 130 (2008) 13850–13851, <https://doi.org/10.1021/ja805795g>.
- J.E. McKeown, W. Bury, D. Fairen-Jimenez, S. Kwon, E.J. DeMarco, M.H. Weston, A.A. Safjeant, S.T. Nguyen, P.C. Stair, R.Q. Snurr, O.K. Farha, J.T. Hupp, Vapor-Phase Metalation by Atomic Layer Deposition in a Metal-Organic Framework, *J. Am. Chem. Soc.* 135 (2013) 10294–10297, <https://doi.org/10.1021/ja405082g>.
- H. Furukawa, F. Gandara, Y.-B. Zhang, J. Jiang, W.L. Queen, M.R. Hudson, O. M. Yaghi, Water Adsorption in Porous Metal-Organic Frameworks and Related Materials, *J. Am. Chem. Soc.* 136 (2014) 4369–4381, <https://doi.org/10.1021/ja500330a>.
- D. Yang, B.C. Gates, Catalysis by Metal Organic Frameworks: perspective and Suggestions for Future Research, *ACS Catal* 9 (2019) 1779–1798, <https://doi.org/10.1021/acs Catal.9b04515>.
- Y. Shan, G. Zhang, Y. Shi, H. Pang, Synthesis and catalytic application of defective MOF materials, *Cell Rep. Phys. Sci.* 4 (2023) 101301, <https://doi.org/10.1016/j.xcrp.2023.101301>.
- A.M. Abdel-Mageed, B. Rungtaweeworant, M. Parlinska-Wojtan, X. Pei, O. M. Yaghi, R.J. Behm, Highly Active and Stable Single-Atom Cu Catalysts Supported by a Metal-Organic Framework, *J. Am. Chem. Soc.* 141 (2019) 5201–5210, <https://doi.org/10.1021/jacs.8b11386>.
- B. Rungtaweeworant, A.M. Abdel-Mageed, P. Khemthong, S. Eaimsumang, K. Chakarawat, T. Butburee, B. Kunkel, S. Wohlrab, K. Chainok, J. Phanthasri, S. Wannapaiboon, S. Youngian, T. Seehamngkol, S. Impeng, K. Faungnawakij, Structural Evolution of Iron-Loaded Metal-Organic Framework Catalysts for Continuous Gas-Phase Oxidation of Methane to Methanol, *ACS Appl. Mater. Interfaces* 15 (2023) 26700–26709, <https://doi.org/10.1021/acsami.3c03310>.
- K. Otake, S. Ahn, J. Knapp, J.T. Hupp, J.M. Notestein, O.K. Farha, Vapor-Phase Cyclohexene Epoxidation by Single-Iron Fe(III) Sites in Metal-Organic Frameworks, *Inorg. Chem.* 60 (2021) 2457–2463, <https://doi.org/10.1021/acs.inorgchem.0c03364>.
- S. Impeng, E. Salaya-Gerónimo, B. Kunkel, S. Bartling, K. Faungnawakij, B. Rungtaweeworant, A.M. Abdel-Mageed, Mechanism and selectivity of MOF-supported Cu single-atom catalysts for preferential CO oxidation, *J. Mater. Chem. A* 12 (2024) 3084–3095, <https://doi.org/10.1039/D3TA05047E>.
- A.M. Abdel-Mageed, B. Rungtaweeworant, S. Impeng, J. Bannmann, J. Rabeah, S. Chen, T. Häring, S. Namuangruk, K. Faungnawakij, A. Brückner, R.J. Behm, Unveiling the CO Oxidation Mechanism over a Molecule-Defined Copper Single-Atom Catalyst Supported on a Metal-Organic Framework, *Angew. Chem. Int. Ed.* 62 (2023) e202301920, <https://doi.org/10.1002/anie.202301920>.
- J. Zhang, B. An, Z. Li, Y. Cao, Y. Dai, W. Wang, L. Zeng, W. Lin, C. Wang, Neighboring Zn–Zr Sites in a Metal-Organic Framework for CO₂ Hydrogenation, *J. Am. Chem. Soc.* 143 (2021) 8829–8837, <https://doi.org/10.1021/jacs.1c03283>.
- J. Liu, W. Xue, W. Zhang, D. Mei, Theoretical Study on the Catalytic CO₂ Hydrogenation over the MOF-808-Encapsulated Single-Atom Metal Catalysts, *J. Phys. Chem. C* 127 (2023) 4051–4062, <https://doi.org/10.1021/acs.jpcc.2c08006>.
- Y. Zhao, D.G. Truhlar, The M06 suite of density functionals for main group thermochemistry, thermochemical kinetics, noncovalent interactions, excited states, and transition elements: two new functionals and systematic testing of four M06-class functionals and 12 other functionals, *Theor. Chem. Acc.* 120 (2008) 215–241, <https://doi.org/10.1007/s00214-007-0310-x>.
- F. Weigend, R. Ahlrichs, Balanced basis sets of split valence, triple zeta valence and quadruple zeta valence quality for H to Rn: design and assessment of accuracy, *Phys. Chem. Chem. Phys.* 7 (2005) 3297–3305, <https://doi.org/10.1039/B508541A>.
- M. Dolg, U. Wedig, H. Stoll, H. Preuss, Energy-adjusted abinitio pseudopotentials for the first row transition elements, *J. Chem. Phys.* 86 (1987) 866–872, <https://doi.org/10.1063/1.452288>.
- A.E. Reed, L.A. Curtiss, F. Weinhold, Intermolecular interactions from a natural bond orbital, donor-acceptor viewpoint, *Chem. Rev.* 88 (1988) 899–926, <https://doi.org/10.1021/cr00088a005>.
- S. Grimme, J. Antony, S. Ehrlich, H. Krieg, A consistent and accurate ab initio parametrization of density functional dispersion correction (DFT-D) for the 94 elements H–Pu, *J. Chem. Phys.* 132 (2010) 154104, <https://doi.org/10.1063/1.3382344>.
- M.J. Frisch, G.W. Trucks, H.B. Schlegel, G.E. Scuseria, M.A. Robb, J.R. Cheeseman, G. Scalmani, V. Barone, G.A. Petersson, H. Nakatsuji, X. Li, M. Caricato, A. V. Marenich, J. Bloino, B.G. Janesko, R. Gomperts, B. Mennucci, H.P. Hratchian, J. V. Ortiz, A.F. Izmaylov, J.L. Sonnenberg, D. Williams-Young, F. Ding, F. Lipparini, F. Egidi, J. Goings, B. Peng, A. Petrone, T. Henderson, D. Ranasinghe, V. G. Zakrzewski, J. Gao, N. Rega, G. Zheng, W. Liang, M. Hada, M. Ehara, K. Toyota, R. Fukuda, J. Hasegawa, M. Ishida, T. Nakajima, Y. Honda, O. Kitao, H. Nakai, T. Vreven, K. Throssel, J.A. Montgomery Jr., J.E. Peralta, F. Ogliaro, M. J. Bearpark, J.J. Heyd, E.N. Brothers, K.N. Kudin, V.N. Staroverov, T.A. Keith, R. Kobayashi, J. Normand, K. Raghavachari, A.P. Rendell, J.G. Burant, S.S. Iyengar, J. Tomasi, A. Cossi, J.M. Millam, M. Klene, C. Adamo, R. Cammi, J.W. Ochterski, R.L. Martin, K. Morokuma, O. Farkas, J.B. Foresman, D.J. Fox, *Gaussian 16*, Rev. C.02, Gaussian, Inc., Wallingford CT, 2019.
- C. Kittel, P. McEuen, *Introduction to Solid State Physics*, 9th ed., John Wiley & Sons, New Jersey, 2018.
- T. Mathom, S. Wannakao, B. Boekfa, J. Limtrakul, Production of Formic Acid via Hydrogenation of CO₂ over a Copper-Alkoxide-Functionalized MOF: A Mechanistic Study, *J. Phys. Chem. C* 117 (2013) 17650–17658, <https://doi.org/10.1021/jp405178p>.
- K. Nilwanna, J. Sittiwong, B. Boekfa, P. Treestikul, S. Boonyu-udtayan, M. Probst, T. Mathom, J. Limtrakul, Aluminum-based metal-organic framework support metal (II)-hydride as catalyst for the hydrogenation of carbon dioxide to formic acid: a computational study, *Mol. Catal.* 541 (2023) 113116, <https://doi.org/10.1016/j.mcat.2023.113116>.
- Y. Chai, B. Qin, B. Li, W. Dai, G. Wu, N. Guan, L. Li, Zeolite-encaged mononuclear copper centers catalyze CO₂ selective hydrogenation to formic acid over a Cu-embedded graphene: a DFT study, *Appl. Surf. Sci.* 364 (2016) 241–248, <https://doi.org/10.1016/j.apsusc.2015.12.117>.
- N. Yodsin, C. Rungnim, S. Tungkamani, V. Promarak, S. Namuangruk, S. Jungstittiwong, DFT Study of Catalytic CO₂ Hydrogenation over Pt-Decorated Carbon Nanocoons: H₂ Dissociation Combined with the Spillover Mechanism, *J. Phys. Chem. C* 124 (2020) 1941–1949, <https://doi.org/10.1021/acs.jpcc.9b08776>.
- Y. Injongkol, R. Inrayot, N. Yodsin, A. Montoya, S. Jungstittiwong, Mechanistic insight into catalytic carbon dioxide hydrogenation to formic acid over Pt-decorated boron nitride nanosheets, *Mol. Catal.* 510 (2021) 111675, <https://doi.org/10.1016/j.mcat.2021.111675>.
- P. Poldorn, Y. Wongnongwa, T. Mudchima, S. Jungstittiwong, Theoretical insights into catalytic CO₂ hydrogenation over single-atom (Fe or Ni) incorporated nitrogen-doped graphene, *J. CO₂ Util* 48 (2021) 101532, <https://doi.org/10.1016/j.jcou.2021.101532>.
- S. Ali, R. Iqbal, A. Khan, S.U. Rehman, M. Haneef, L. Yin, Stability and Catalytic Performance of Single-Atom Catalysts Supported on Defective and Defective Graphene for CO₂ Hydrogenation to Formic Acid: a First-Principles Study, *ACS Appl. Nano Mater.* 4 (2021) 6893–6902, <https://doi.org/10.1021/acsnano.1c00959>.
- Y. Zhang, Y. Mo, Z. Cao, Rational Design of Main Group Metal-Embedded Nitrogen-Doped Carbon Materials as Frustrated Lewis Pair Catalysts for CO₂ Hydrogenation to Formic Acid, *ACS Appl. Mater. Interfaces* 14 (2022) 1002–1014, <https://doi.org/10.1021/acscami.1c20230>.

- [41] X. Liang, Q. Ke, X. Zhao, X. Chen, Graphene-Supported Tin Single-Atom Catalysts for CO₂ Hydrogenation to HCOOH: a Theoretical Investigation of Performance under Different N Coordination Numbers, *ACS Appl. Nano Mater.* 6 (2023) 4489–4498, <https://doi.org/10.1021/acsnm.2c05581>.
- [42] M. Creutzburg, K. Sellschopp, S. Tober, E. Grånäs, V. Vonk, W. Mayr-Schmölzer, S. Müller, H. Noei, G.B. Vonbun-Feldbauer, A. Stierle, Heterogeneous Adsorption and Local Ordering of Formate on a Magnetite Surface, *J. Phys. Chem. Lett.* 12 (2021) 3847–3852, <https://doi.org/10.1021/acs.jpclett.1c00209>.
- [43] F.A. Cotton, G. Wilkinson, C.A. Murillo, M. Bochmann, *Advanced Inorganic Chemistry*, 6th ed., John Wiley & Sons, New York, 1999.



Poster presentation

Abstract of poster presentation of CO₂ hydrogenation to formic acid by single-atom Cu anchored on MOF-808(Zr): A DFT study for PACCON 2023 at Mae Fah Luang University, Chiang Rai, Thailand, 20-21 January 2023.



CO₂ hydrogenation to formic acid by single-atom Cu anchored on MOF-808(Zr): A DFT Study

Nawarat Kusonjariyakun¹, Jirapat Santatiwongchai², Warot Chotpatiwetchkul,^{1*} Sarawoot Impeng^{2*}

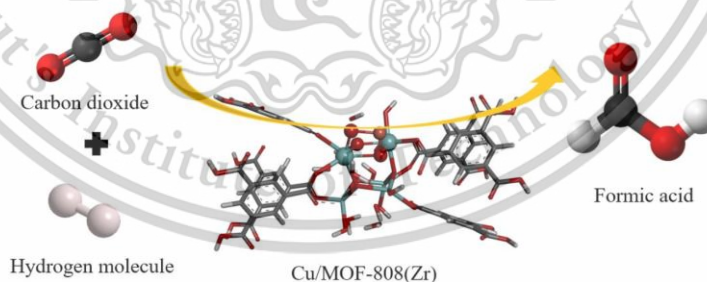
¹Applied Computational Chemistry Research Unit, Department of Chemistry, School of Science, King Mongkut's Institute of Technology Ladkrabang, Bangkok 10520, Thailand

²National Nanotechnology Center (NANOTEC), National Science and Technology Development Agency (NSTDA), Pathum Thani 12120, Thailand


*E-mail: warot.ch@kmitl.ac.th, sarawoot.imp@nanotec.or.th

Carbon dioxide (CO₂) is one of the greenhouse gases that contribute to global warming. The conversion of CO₂ to valuable chemicals is of great interest from environmental and economic views. In this work, DFT calculations with the M06-L density functional were employed to investigate the hydrogenation of CO₂ to formic acid on single-atom Cu supported by MOF-808(Zr), denoted as Cu/MOF-808(Zr). The reaction proceeds in two steps, the H₂ dissociation and CO₂ hydrogenation to form formic acid. The computational results show that the H₂ dissociation is a feasible process with an energy barrier of approximately 15 kcal/mol. The CO₂ hydrogenation proceeds via formate intermediate in which the first step of reaction requires a small energy barrier of about 8 kcal/mol. The second step of CO₂ hydrogenation is under investigation. According to these results, the Cu/MOF-808(Zr) is suggested as a promising catalyst for CO₂ hydrogenation to formic acid.

Keywords: CO₂ hydrogenation; CO₂ conversion; DFT calculations; MOFs; formic acid



Poster presentation of CO₂ hydrogenation to formic acid by single-atom Cu anchored on MOF-808(Zr): A DFT study for PACCON 2023 at Mae Fah Luang University, Chiang Rai, Thailand, 20-21 January 2023.



CHEMICAL DIVERSITY TOWARDS SUSTAINABLE DEVELOPMENT GOALS

Mae Fah Luang University, Chiang Rai, THAILAND

CO₂ hydrogenation to formic acid by single-atom Cu anchored on MOF-808(Zr): A DFT study

Nawarat Kusonjariyakun¹, Jirapat Santatiwongchai², Warot Chotpatiwetchkul^{1*}, Sarawoot Impeng^{2*}

¹Applied Computational Chemistry Research Unit, Department of Chemistry, School of Science, King Mongkut's Institute of Technology Ladkrabang, Bangkok 10520, Thailand
²National Nanotechnology Center (NANOTEC), National Science and Technology Development Agency (NSTDA), Pathum Thani 12120, Thailand
 *E-mail : warot.ch@kmitl.ac.th, sarawoot.imp@nanotec.or.th

Abstract

Carbon dioxide (CO₂) is one of the greenhouse gases that contribute to global warming. The conversion of CO₂ to valuable chemicals is of great interest from environmental and economic views. In this work, DFT calculations with the M06-L density functional were employed to investigate the hydrogenation of CO₂ to formic acid on single-atom Cu supported by MOF-808(Zr), denoted as Cu/MOF-808(Zr). The reaction proceeds in two steps, the H₂ dissociation and CO₂ hydrogenation to form formic acid. The computational results show that the H₂ dissociation is a feasible process with an energy barrier of approximately 15 kcal/mol. The CO₂ hydrogenation proceeds via formate intermediate in which the first step of reaction requires a small energy barrier of about 8 kcal/mol. The second step of CO₂ hydrogenation is under investigation. According to these results, the Cu/MOF-808(Zr) is suggested as a promising catalyst for CO₂ hydrogenation to formic acid.

Introduction

One of the greenhouse gases that causes global warming is carbon dioxide (CO₂). Thus, the conversion of CO₂ to high-value chemicals is of great interest from environmental and economic views. One example of CO₂ conversion to a valuable chemical is hydrogenation of CO₂ to formic acid (HCOOH).

In this work, density functional theory (DFT) calculations were performed to investigate the hydrogenation of CO₂ to HCOOH over single-atom Cu anchored MOF-808(Zr), Cu/MOF-808(Zr).

Model & Method

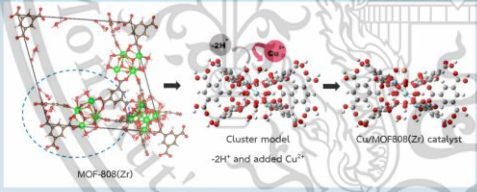
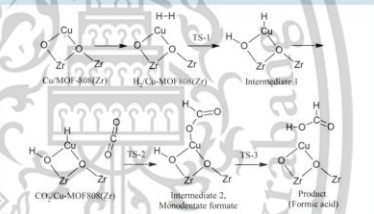


Figure 1: Cu/MOF-808(Zr) catalyst model

Method

- ◆ Spin-unrestricted DFT calculations with the M06-L density functional.
- ◆ The def2-SVP basis set for C, H, O atoms.
- ◆ The SDD pseudopotential basis set for Zr, Cu atoms.
- ◆ The Gaussian 09 & 16 programs.

Results



Scheme 1. Proposed mechanism for CO₂ conversion to HCOOH over Cu/MOF-808(Zr)

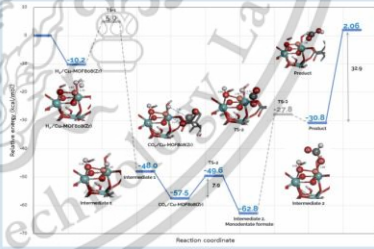


Figure 2. Reaction profile for the hydrogenation of CO₂ to HCOOH over Cu/MOF-808(Zr)

References

- ◆ Zhang, J. An, B. Li, Z. Cao, Y. Dai, Y. Wang, W. Zeng, L. Lin, W. and Wang, C. 2021. Journal of the American Chemical Society. 143 : 8829-8837.
- ◆ Yodsin, N. Rungruim, C. Tungkamani, S. Promarak, V. Namuangruk, S. and Jungsuttiwong, S. 2020. The Journal of Physical Chemistry C. 124(3) : 1941-194.
- ◆ Ahmed, I. Sung, H.J. 2014. Materials Today. 17(3) : 136-46.

Conclusions

- ◆ DFT calculations have been carried out to investigate the CO₂ hydrogenation reaction over Cu/MOF-808(Zr).
- ◆ The reaction proceeds in two steps, the H₂ dissociation followed by CO₂ hydrogenation to produce HCOOH.
- ◆ From energy profile, the H₂ dissociation is feasible, and that the resulting reaction intermediate is stable and active for the hydrogenation of CO₂ to HCOOH.
- ◆ The hydrogenation of CO₂ proceeds via formate intermediate (monodentate configuration) which requires a small energy barrier of 7.9 kcal/mol.
- ◆ From these results, the Cu/MOF-808(Zr) is considered as a potential catalyst for the hydrogenation of CO₂ to HCOOH.



Acknowledgments

- ◆ Department of Chemistry, School of Science, King Mongkut's Institute of Technology Ladkrabang (KMITL)
- ◆ National Nanotechnology Center (NANOTEC), National Science and Technology Development Agency (NSTDA)

This material is reserved for educational use only, not allowed for commercial use.

Forbidden to modify the content, and cite the document when use.

Poster presentation of CO₂ hydrogenation to formic acid by single-atom Cu anchored on MOF-808(Zr): A DFT study for KMITL Innovation expo 2023 at King Mongkut's Institute of Technology Ladkrabang, Bangkok, Thailand, 27-29 April 2023.


CO₂ hydrogenation to formic acid by single-atom Cu anchored on MOF-808(Zr): A DFT study

Nawarat Kusonjariyakun¹, Jirapat Santatiwongchai², Warot Chotpatiwetchkul,^{1*} Sarawoot Impeng^{2*}

¹Applied Computational Chemistry Research Unit, Department of Chemistry, School of Science, King Mongkut's Institute of Technology Ladkrabang, Bangkok 10520, Thailand
²National Nanotechnology Center (NANOTEC), National Science and Technology Development Agency (NSTDA), Pathum Thani 12120, Thailand
*E-mail : warot.chg@kmitl.ac.th, sarawoot.imp@nanotec.or.th

Abstract

Carbon dioxide (CO₂) is one of the greenhouse gases that contribute to global warming. The conversion of CO₂ to valuable chemicals is of great interest from environmental and economic views. In this work, DFT calculations with the M06-L density functional were employed to investigate the hydrogenation of CO₂ to formic acid on single-atom Cu supported by MOF-808(Zr), denoted as Cu/MOF-808(Zr). The reaction proceeds in two steps, the H₂ dissociation and CO₂ hydrogenation to form HCOOH. The computational results show that the H₂ dissociation is a feasible process with an energy barrier of approximately 15 kcal/mol. The CO₂ hydrogenation proceeds via formate intermediate in which the first step of reaction requires a small energy barrier of about 8 kcal/mol. The second step of CO₂ hydrogenation is under investigation. According to these results, the Cu/MOF-808(Zr) is suggested as a promising catalyst for CO₂ hydrogenation to formic acid.

Introduction

One of the greenhouse gases that causes global warming is carbon dioxide (CO₂). Thus, the conversion of CO₂ to high-value chemicals is of great interest from environmental and economic views. One example of CO₂ conversion to a valuable chemical is hydrogenation of CO₂ to formic acid (HCOOH).

In this work, density functional theory (DFT) calculations were performed to investigate the hydrogenation of CO₂ to HCOOH over single-atom Cu anchored MOF-808(Zr), Cu/MOF-808(Zr).

Results



Scheme 1. Proposed mechanism for CO₂ conversion to HCOOH over Cu/MOF-808(Zr)

Model & Method



Figure 1: Cu/MOF-808(Zr) catalyst model

Method

- ◆ Spin-unrestricted DFT calculations with the M06-L density functional.
- ◆ The def2-SVP basis set for C, H, O atoms.
- ◆ The SDD pseudopotential basis set for Zr, Cu atoms.
- ◆ The Gaussian 09 & 16 programs.

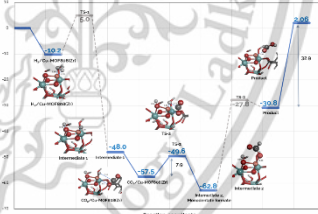


Figure 2. Reaction profile for the hydrogenation of CO₂ to HCOOH over Cu/MOF-808(Zr)

References

- ◆ Zhang, J. An, B. Li, Z. Cao, Y. Dai, Y. Wang, W. Zeng, L. Lin, W. and Wang, C. 2021. Journal of the American Chemical Society. 143 : 8829-8837.
- ◆ Yodsri, N. Rungnim, C. Tungkamani, S. Promarak, V. Namuangruk, S. and Jungsutiwong, S. 2020. The Journal of Physical Chemistry C. 124(3) : 1941-194.
- ◆ Ahmed, I. Sung, H.J. 2014. Materials Today. 17(3) : 136-66.


Conclusions

- ◆ DFT calculations have been carried out to investigate the CO₂ hydrogenation reaction over Cu/MOF-808(Zr).
- ◆ The reaction proceeds in two steps, the H₂ dissociation followed by CO₂ hydrogenation to produce HCOOH.
- ◆ From energy profile, the H₂ dissociation is feasible, and that the resulting reaction intermediate is stable and active for the hydrogenation of CO₂ to HCOOH.
- ◆ The hydrogenation of CO₂ proceeds via formate intermediate (monodentate configuration) which requires a small energy barrier of 7.9 kcal/mol.
- ◆ From these results, the Cu/MOF-808(Zr) is considered as a potential catalyst for the hydrogenation of CO₂ to HCOOH.

Acknowledgments

- ◆ Department of Chemistry, School of Science, King Mongkut's Institute of Technology Ladkrabang (KMITL)
- ◆ National Nanotechnology Center (NANOTEC), National Science and Technology Development Agency (NSTDA)

ช่องทางการติดต่อ : 061-7765919 (Nawarat)



Author biography

Name	Miss Nawarat Kusonjariyakun
Date of Birth	21 August 1999
Address	86-88 Setthasamphan Road, Nongkhae Subdistrict, Nongkhae District, Saraburi 18140
Education	(2021) Bachelor of Science in Industrial Chemistry (GPA 2.88) (King Mongkut's Institute of Technology Ladkrabang) (2024) Master of Science in Applied Chemistry (King Mongkut's Institute of Technology Ladkrabang)
Scholarship	School of Science, King Mongkut's Institute of Technology Ladkrabang (Grant No. RA/TA-2565-M-009)
Academic Publication	1. Hydrogenation of Carbon Dioxide to Formic Acid Catalyzed by Cu and Co Single-atom Catalyst Supported on MOF-808: A DFT investigation